


# The qPlus sensor, a powerful core for the atomic force microscope

Cite as: Rev. Sci. Instrum. **90**, 011101 (2019); <https://doi.org/10.1063/1.5052264>

Submitted: 15 August 2018 • Accepted: 25 December 2018 • Published Online: 30 January 2019

 Franz J. Giessibl

## COLLECTIONS

 This paper was selected as Featured



View Online



Export Citation



CrossMark

## ARTICLES YOU MAY BE INTERESTED IN

[High-speed force sensor for force microscopy and profilometry utilizing a quartz tuning fork](#)



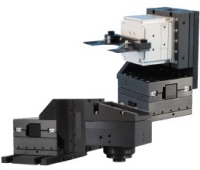
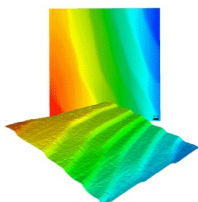
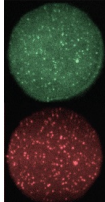
Applied Physics Letters **73**, 3956 (1998); <https://doi.org/10.1063/1.122948>

[Atomic resolution on Si\(111\)-\(7×7\) by noncontact atomic force microscopy with a force sensor based on a quartz tuning fork](#)

Applied Physics Letters **76**, 1470 (2000); <https://doi.org/10.1063/1.126067>

[WSXM: A software for scanning probe microscopy and a tool for nanotechnology](#)

Review of Scientific Instruments **78**, 013705 (2007); <https://doi.org/10.1063/1.2432410>

 <b>MCL</b> MAD CITY LABS INC. <a href="http://www.madcitylabs.com">www.madcitylabs.com</a>	<p>Nanopositioning Systems</p> 	<p>Modular Motion Control</p> 	<p>AFM and NSOM Instruments</p> 	<p>Single Molecule Microscopes</p> 
---	--	--	---	--

# The qPlus sensor, a powerful core for the atomic force microscope

Cite as: Rev. Sci. Instrum. 90, 011101 (2019); doi: [10.1063/1.5052264](https://doi.org/10.1063/1.5052264)

Submitted: 15 August 2018 • Accepted: 25 December 2018 •

Published Online: 30 January 2019



Franz J. Giessibl<sup>a)</sup> 

## AFFILIATIONS

Institute of Experimental and Applied Physics, University of Regensburg, Universitätsstrasse 31, D-93040 Regensburg, Germany

<sup>a)</sup>Electronic mail: [franz.giessibl@ur.de](mailto:franz.giessibl@ur.de)

## ABSTRACT

Atomic force microscopy (AFM) was introduced in 1986 and has since made its way into surface science, nanoscience, chemistry, biology, and material science as an imaging and manipulating tool with a rising number of applications. AFM can be employed in ambient and liquid environments as well as in vacuum and at low and ultralow temperatures. The technique is an offspring of scanning tunneling microscopy (STM), where the tunneling tip of the STM is replaced by using a force sensor with an attached tip. Measuring the tiny chemical forces that act between the tip and the sample is more difficult than measuring the tunneling current in STM. Therefore, even 30 years after the introduction of AFM, progress in instrumentation is substantial. Here, we focus on the core of the AFM, the force sensor with its tip and detection mechanism. Initially, force sensors were mainly micro-machined silicon cantilevers, mainly using optical methods to detect their deflection. The qPlus sensor, originally based on a quartz tuning fork and now custom built from quartz, is self-sensing by utilizing the piezoelectricity of quartz. The qPlus sensor allows us to perform STM and AFM in parallel, and the spatial resolution of its AFM channel has reached the subatomic level, exceeding the resolution of STM. Frequency modulation AFM (FM-AFM), where the frequency of an oscillating cantilever is altered by the gradient of the force that acts between the tip and the sample, has emerged over the years as the method that provides atomic and subatomic spatial resolution as well as force spectroscopy with sub-piconewton sensitivity. FM-AFM is precise; because of all physical observables, time and frequency can be measured by far with the greatest accuracy. By design, FM-AFM clearly separates conservative and dissipative interactions where conservative forces induce a frequency shift and dissipative interactions alter the power needed to maintain a constant oscillation amplitude of the cantilever. As it operates in a noncontact mode, it enables simultaneous AFM and STM measurements. The frequency stability of quartz and the small oscillation amplitudes that are possible with stiff quartz sensors optimize the signal to noise ratio. Here, we discuss the operating principles, the assembly of qPlus sensors, amplifiers, limiting factors, and applications. Applications encompass unprecedented subatomic spatial resolution, the measurement of forces that act in atomic manipulation, imaging and spectroscopy of spin-dependent forces, and atomic resolution of organic molecules, graphite, graphene, and oxides.

Published under license by AIP Publishing. <https://doi.org/10.1063/1.5052264>

## I. INTRODUCTION

### A. Atomic force microscopy (AFM)

The first instrument that allowed to image a surface at atomic resolution was the scanning tunneling microscope (STM). STM was invented by Gerd Binnig and Heinrich Rohrer in 1981, and the author still remembers the day in the fall of 1985 when he first heard about this incredible instrument in a hallway of ETH Zurich as an undergraduate student. In those days, it was taught early on in school that while the

existence of atoms is unquestioned, it is impossible to “see” them except for the atomic structure of sharp tips in a field ion microscope. Today, high school students perform STM experiments, and it is hard to recollect the strong skepticism against the true resolution of atoms that prevailed in the scientific community before the invention of STM. It was strongly doubted that the challenges posed by mechanical and thermal vibrations that oppose stable tunneling across a vacuum gap between a sharp tip and a flat sample could ever be mastered. Any remaining doubts about the capability to resolve atoms

evaporated when Binnig, Rohrer, Gerber, and Weibel showed a real space image of the silicon (111)-(7 × 7) surface in 1983.<sup>22</sup> Binnig and Rohrer received the Nobel Prize in Physics already in 1986 for the invention of STM, shared with Ernst Ruska, the inventor of the electron microscope. The challenges of implementing STM in the early years are recollected in the Nobel lecture of Binnig and Rohrer.<sup>23</sup> Although the technical challenges to create a scanning tunneling microscope that operates in an ultrahigh vacuum (UHV) to provide clean and well defined surfaces and tips were huge, the physics of the quantum mechanical tunneling effect is highly supportive to the concept of a microscope based on electron tunneling. Heinrich Rohrer named the achievement of vacuum tunneling<sup>21</sup> as the birth of STM in a noteworthy talk at the 1991 International Conference on STM in Interlaken, Switzerland. STM relies on the quantum mechanical tunneling current between two biased electrodes, the tip and the sample. This tunneling current increases by a factor of ten when decreasing the tip-sample distance by one Å (100 pm). Even for a relatively blunt metal tip close to a flat surface, chances are high that one atom in the tip apex sticks out by, say, a third of an atomic diameter, thereby carrying the major part of the tunneling current and thus enabling the spectacular atomic resolution.

The monotonic exponential increase of the tunneling current enables a simple implementation of a distance control loop, where the logarithm of the ratio between the actual tunneling current and its setpoint yields a linear and monotonic input for a distance regulator.

Careful observations during operation of the STM revealed to Binnig that atomic forces are present (see also Refs. 46 and 209), and in 1985, Binnig suggested to utilize these forces and invented a new type of microscope, the “Atomic Force Microscope” (AFM),<sup>24</sup> a microscope that should extend the atomic resolution capability of STM to insulating samples as reported in the opening paragraph of Ref. 203. A first working version of AFM was introduced by Binnig, Gerber, and Quate in 1986,<sup>25</sup> in a publication that has been cited close to ten thousand times since. Conceptually, the atomic force microscope might be viewed as a highly refined stylus profilometer, an instrument that maps a surface using a cantilever with a sharp tip that scans across a surface and records its topography line by line. However, the spatial resolution provided by stylus profilometry is much lower than needed for reaching the atomic scale, and documented evidence that profilometry might ever reach atomic resolution levels is not known to us. Therefore, AFM has its origin more in the scanning tunneling microscope (STM) which has opened direct access to matter on the single atom scale. Although the AFM did not achieve atomic resolution from the start, it became much more widespread in use than STM because it works in any environment and can image conductors and insulators. An estimated ten thousand atomic force microscopes are in use worldwide today, and in 2016, 30 years after their seminal paper,<sup>25</sup> Binnig, Quate, and Gerber were rewarded with the Kavli Prize for Nanoscience. Many review papers<sup>64,86,118</sup> and books<sup>167-169</sup> are available that discuss the key elements of the rise of AFM.

In the development of STM, profound experimental challenges have been mastered such as establishing mechanically stable vacuum tunneling junctions on a picometer lengthscale, sub-Angstrom scanning precision, as well as the preparation of atomically sharp tips and clean flat samples. Nevertheless, reaching atomic resolution by AFM required overcoming additional profound challenges that are rooted in the added complexity of the control signal, the force. While the tunneling current in vacuum is

1. monotonic with distance,
2. extremely short range and thus originating mainly from the tip's front atom, and
3. ranging from pA to hundreds of nA and easily measured experimentally, the tip-sample force shares none of these three characteristics of the tunneling current. First, the tip-sample force is not monotonic, and it is usually initially attractive, turning repulsive when atoms get in contact. Second, the force is composed of strong long-range components due to van der Waals and other interactions, and the chemical forces that allow for atomic resolution are often much smaller in magnitude. Third, the experimental difficulties to measure forces in the pico- to nanonewton regime are much harder than those encountered when measuring currents in the pico- to nanoampere regime. For operation in ambient conditions, contamination layers add to the complexity of the tip-sample interaction. For these reasons, the spatial resolution of AFM did not reach the spatial resolution of STM for a long time, and initially, common experience and expectations held that the AFM will stay behind the resolution of STM forever. Today, the AFM usually exceeds the spatial resolution of STM, and the key element of the AFM is the force detector with its tip and deflection sensor,<sup>56</sup> which is the subject of the present article.

## B. Principle and operating modes of atomic force microscopy

### 1. Quasistatic mode

The quasistatic mode is the simplest mode of AFM, where the cantilever scans the surface similar to the stylus in the profilometer or the needle of a record player. In the static (or dc-) mode, the tip-sample force  $F_{ts}$  leads to a deflection  $q$  of a cantilever beam with force constant  $k$  given by

$$q = \frac{F_{ts}}{k}. \quad (1)$$

Early after the introduction of AFM, reports about the achievement of atomic resolution appeared. While atomic lattices were shown in these early reports, steps or defects were not observed, and the appearance of atomic lattices was explained with an egg-carton effect where the tip assumes a negative of the sample after repeated scanning (see, e.g., Fig. 1 in Ref. 69). One key challenge of obtaining true atomic resolution in the quasistatic mode is the presence of strong long-range forces that lead to an uncontrolled “jump-to-contact” of the cantilever when it is brought close to the surface. It is possible to obtain true atomic resolution in quasistatic mode for certain

conditions. In one experiment,<sup>68</sup> KBr(001) was resolved atomically in a low-temperature UHV microscope using a special trick: when the cantilever had landed on the KBr surface after jump-to-contact, the load on the cantilever due to the strong van der Waals forces was reduced by pulling the sample back to a point just before the contact between the cantilever and the sample was lost again. Then, the sample was moved laterally from the damaged cantilever landing zone to an area that was pristine and scanning was resumed at a repulsive interaction of an estimated 1 nN yet a net attractive interaction. Despite the small repulsive interaction, the 5 nm scanframe was slightly depressed and a small superstructure was induced in the scanned area (see Fig. 20 in Ref. 86). In 1993, Ohnesorge and Binnig obtained true atomic resolution in ambient conditions on calcite with quasistatic AFM in contact- and noncontact modes, even resolving an atomic step.<sup>179</sup> Here, the trick was to immerse the surface and the cantilever in water, thus preventing jump-to-contact by strongly reducing the van der Waals interaction.<sup>131</sup>

## 2. Dynamic modes

The quasistatic mode is conceptually simple. However, it has a few drawbacks. First, it is hard to measure static deflections of small springs with a good signal-to-noise ratio (SNR). Second, the contact between the tip and the sample can lead to wear and tear. Third, the chemical bonding forces that enable atomic contrast are typically overwhelmed by large long-range van der Waals forces. These three challenges can be met by operating in a dynamic mode, in particular, with a dynamic mode that operates at small amplitudes (see Fig. 1).

The original publication about the AFM already discussed dynamic modes of operation of AFM.<sup>25</sup> Currently, most AFMs operating in ambient conditions use amplitude modulation (AM) mode. In this mode, the cantilever is driven to oscillate at a constant frequency close to the eigenfrequency  $f_0$  of the cantilever. The tip-sample interaction changes the oscillation amplitude, and this change is used as a feedback signal. Both dissipative and non-dissipative parts of the interaction force change the resulting amplitude, and a separation of those two force parts is not straightforward. Often, the phase image that shows the difference in phase between the driving signal and the oscillation provides greater spatial resolution. The reason for the widespread use of the AM mode rests on two characteristics. First, it is relatively simple to measure the amplitude at the operational frequency of the cantilever—a lock-in technique allows for excellent precision. Second, a monotonic feedback signal is available in AM-AFM: The setpoint of the amplitude is smaller than the amplitude of the free oscillation, and the tip-sample interaction upon reducing the distance reduces the amplitude in a more or less monotonic fashion (except for a subtle artifact<sup>10</sup>).

The technically more advanced frequency modulation mode (FM-AFM)<sup>2,47</sup> strictly separates dissipative and non-dissipative interactions—dissipative interactions lead to an increase in the driving amplitude that excites the oscillation of the cantilever, and non-dissipative interactions lead to a frequency shift.

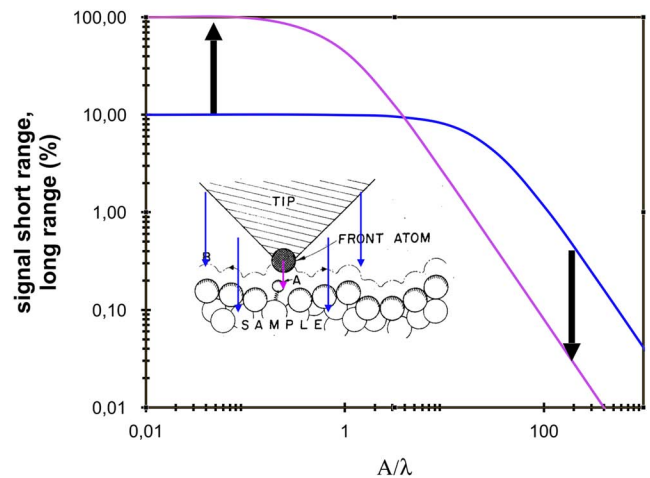


**FIG. 1.** Long- and short-range contributions to the frequency shift  $\Delta f$  as a function of amplitude for a force that consists of a short range force (plotted in magenta)  $F_{sr}(z) = F_{0\ sr} \cdot \exp(-z/\lambda_{sr})$  and a long-range force (blue)  $F_{lr}(z) = F_{0\ lr} \cdot \exp(-z/\lambda_{lr})$ . Here, we have adapted a typical example of  $F_{0\ lr} = 3 \cdot F_{0\ sr}$  and  $\lambda_{lr} = 30 \cdot \lambda_{sr}$ . For amplitudes  $A$  that are small compared to the range of the interaction  $\lambda$ , the frequency shift is proportional to the force gradient  $F/\lambda$ ; for large amplitudes, it is expressed by the normalized frequency shift  $\gamma = \Delta f/f_0 k A^{3/2} \propto F\sqrt{\lambda}$ . The influence of short- and long-range forces can thus be adjusted by the choice of amplitude  $A$ : small amplitudes result in a good sensitivity for short-range forces, and large amplitudes emphasize long-range forces. Guide to read this plot: for a specific type of cantilever or sensor, the frequency shift for infinitely small amplitudes amounts to 100 Hz due to short range forces and 10 Hz due to long range forces. Upon increasing the amplitude to  $\lambda_{sr}$ , the short range contribution starts to drop, while the frequency shift due to long range forces remains constant. Once the amplitude is significantly larger than  $\lambda_{lr}$ , the frequency shift contribution due to long range forces is 16 times larger than the short range contribution, i.e., the short range versus long range contributions change from 10 to 1/16 as the amplitude is increased. Inset: Schematic presentation of the tip and the sample, reprinted with permission from Binnig *et al.*, Phys. Rev. Lett. **56**, 930 (1986). Copyright 1986 The American Physical Society.

## 3. Stability criterion

Attractive forces between the tip and the sample can lead to an uncontrolled jump-to-contact of the cantilever when approaching it to a sample.<sup>30</sup> In the quasistatic mode, jump-to-contact is prevented if the stiffness  $k$  of the cantilever fulfills the following condition:

$$k > \max\left(-\frac{\partial^2 V_{ts}}{\partial z^2}\right), \quad (2)$$

where  $V_{ts}$  is the potential energy between the tip and the sample. In the dynamic modes, jump-to-contact can be prevented for any cantilever, provided the amplitude  $A$  is large enough,<sup>78</sup>

$$k \cdot A > \max\left(\frac{\partial V_{ts}}{\partial z}\right). \quad (3)$$

An oscillation of the cantilever stabilizes it—it can only become unstable if the tip-sample force  $F_{ts} = -\partial V_{ts}/\partial z$  is greater in magnitude than the restoring force  $k \cdot A$ . In the first achievement of atomic resolution in noncontact AFM, the second criterion to prevent jump-to-contact was fulfilled by adjusting



a large amplitude of 34 nm to stabilize the relatively soft cantilever ( $k = 17$  N/m) at the close tip-sample distances required to obtain atomic resolution.<sup>71</sup>

## II. PHYSICS OF FREQUENCY MODULATION ATOMIC FORCE MICROSCOPY

Of all physical observables, time and its inverse, frequency, can be measured by far at the greatest precision.<sup>224</sup> Today, frequency modulation AFM (FM-AFM)<sup>2,47</sup> has emerged as the AFM technique that enables high spatial and force resolution with a straightforward separation of conservative and dissipative interactions. In FM-AFM, the cantilever is driven to oscillate by applying positive feedback to obtain a constant amplitude  $A$  and the conservative force between the tip and the sample alters the frequency from the natural eigenfrequency  $f_0$  of the cantilever to  $f = f_0 + \Delta f$ , while dissipative forces induce the amplitude feedback to adjust the drive signal  $A_{drive}$  to keep  $A$  constant.

### A. Signal–Frequency shift and its dependence on tip-sample forces

#### 1. Frequency shift as a function of tip-sample forces

In frequency modulation atomic force microscopy, the oscillation of the force sensor is driven by feeding back its deflection, phase shifted by  $+\pi/2$ , to an actuator that shakes the base of the cantilever with a drive amplitude  $A_{drive}$ . An automatic gain circuit adjusts  $A_{drive}$  to establish a constant oscillation amplitude  $A$ . The oscillation frequency corresponds to  $f_0$ , the eigenfrequency of the cantilever, when the tip is far from the surface and the force gradient field between the tip and the sample is close to zero. For smaller distances, the tip-sample force gradient increases and leads to a frequency shift  $\Delta f = f - f_0$ . With  $f = f_0 + \Delta f$  and  $f_0 = \frac{1}{2\pi} \sqrt{k/m^*}$ , the frequency shift is given by

$$\Delta f = \frac{f_0}{2k} \langle k_{ts} \rangle \quad (4)$$

with<sup>84</sup>

$$\langle k_{ts} \rangle(z, A) = \frac{2}{\pi} \int_{-1}^1 k_{ts}(z + \zeta A) \sqrt{1 - \zeta^2} d\zeta. \quad (5)$$

This equation shows that the frequency shift is a function of the amplitude. Two extreme cases allow a simplification. When the amplitude is *small* compared to the range of the tip-sample interaction  $\lambda$ , the gradient approximation holds, i.e.,

$$\langle k_{ts} \rangle(z, A \ll \lambda) \approx k_{ts}(z). \quad (6)$$

When the amplitude is *large* compared to the range of the tip-sample interaction  $\lambda$ , it is useful to introduce a large-amplitude approximation where the frequency shift is given by

$$\Delta f = \frac{f_0}{k} \frac{1}{A^{3/2}} \gamma_{ts} \quad (7)$$

with the “normalized frequency shift”  $\gamma_{ts} \approx 0.4 F_{ts} \sqrt{\lambda}$ .<sup>78</sup> In FM-AFM, the signal is a frequency shift  $\Delta f$ . This frequency shift depends on the tip-sample interaction and the stiffness  $k$ ,

eigenfrequency  $f_0$ , and amplitude  $A$  of the cantilever. For a force that follows an exponential distance dependence  $F(z) = F_0 \exp(-z/\lambda)$ , we find

$$\Delta f = \frac{f_0}{kA} F_0 e^{-(z+A)/\lambda} I_1(A/\lambda), \quad (8)$$

where  $I_1(A/\lambda)$  is the Bessel function of the first kind, a special version of the Kummer function.<sup>83</sup>

We can rewrite Eq. (8) such that its resemblance to the gradient approximation is directly evident,

$$\Delta f = \frac{f_0}{2k} \kappa F_0 e^{-z/\lambda} \frac{2I_1(A/\lambda) e^{-A/\lambda}}{A/\lambda}. \quad (9)$$

The first factor in this equation is the gradient approximation, while the fraction  $2I_1(x)e^{-x}/x$  with  $x = A/\lambda$  can be expanded as  $2I_1(x)e^{-x}/x = 1 - x + 5/8x^2 + O(x^3)$ . For a minimum distance between the tip and the sample of  $z$ , the tip oscillates within the interval  $[z, z + 2A]$ , and at the optimal oscillation amplitude  $A_{opt} \approx 1.545\lambda$ ,<sup>92</sup> we obtain an average tip-sample force gradient that is approximately one third of the peak force gradient at distance  $z$  because  $2I_1(1.5451)e^{-1.5451}/1.5451 \approx 0.33$ .

#### 2. Amplitude dependence of short-range force contributions to the frequency shift $\Delta f$

For a total force given by a sum of long-range and short-range forces  $F(z) = F_{0\text{lr}} \exp(-z/\lambda_{lr}) + F_{0\text{sr}} \exp(-z/\lambda_{sr})$ , we obtain the total frequency shift with Eq. (10). The frequency shift is given by

$$\Delta f = \frac{f_0}{kA} (F_{0\text{lr}} e^{-(z+A)/\lambda_{lr}} I_1(A/\lambda_{lr}) + F_{0\text{sr}} e^{-(z+A)/\lambda_{sr}} I_1(A/\lambda_{sr})). \quad (10)$$

The amplitude dependence of the frequency shift is displayed in Fig. 1. For amplitudes  $A$  that are smaller than the range of the short-range forces  $\lambda$ , the frequency shift is constant. However, once  $A$  reaches  $\lambda$ , the frequency shift starts to drop at a high rate proportional to  $1/A^{3/2}$ .

Figure 2 highlights the relevant observables that govern STM and AFM in a logarithmic display. The black curve shows

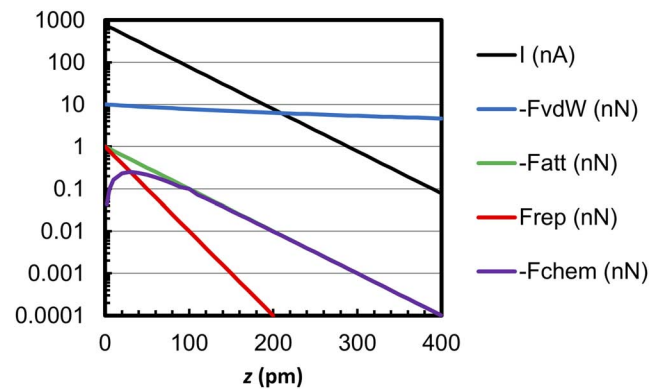


**FIG. 2.** Logarithmic plot of the tunneling current  $I$ , van der Waals force  $F_{vdW}$ , and chemical bonding force  $F_{chem}$  composed of attractive ( $F_{att}$ ) and repulsive ( $F_{rep}$ ) components. The long-range van der Waals force typically dominates the interaction force by a large margin, so it masks the chemical bonding forces that enable true atomic resolution of AFM.

the tunneling current with its typical factor ten increase for each distance reduction of 100 pm. A strong distance dependence is important for high spatial resolution. The distance control loop features a logarithmic amplifier that computes an error signal from the logarithm of the ratio between the tunneling current and its setpoint  $s_{\text{error}} = \log(I/I_{\text{set}})$ . This signal  $s_{\text{error}}$  is smaller than zero if the current is below its setpoint and greater than zero otherwise. The error signal  $s_{\text{error}}$  enters a PI (proportional-integral) controller, enabling a stable and simple feedback loop.

FM-AFM measures forces that are typically composed of long- and short-range contributions, where the long-range contributions arise from van der Waals and electrostatic forces. These long-range forces do not contribute to atomic resolution and should be filtered out. The long-range force has a very weak distance dependence but a large magnitude compared to the short-range attractive (green) and repulsive (red) forces. This graph outlines an important consequence of the choice of amplitude in an FM-AFM experiment: choosing a small amplitude increases the contribution of short-range forces to the frequency shift, and the use of large amplitudes results in a large contribution of long-range forces to the frequency shift. When using soft cantilevers, a relatively large amplitude might have to be chosen in order to obtain a stable oscillation; see Eq. (3).

Figure 3 is a display of currents and force gradients. We notice a striking difference between the role of short-range and long-range components: the force gradient of the short-range forces is larger than the gradient of the long-range force for small distances. Also, the slope of the repulsive Pauli force is typically larger than even the slope of the tunneling current.

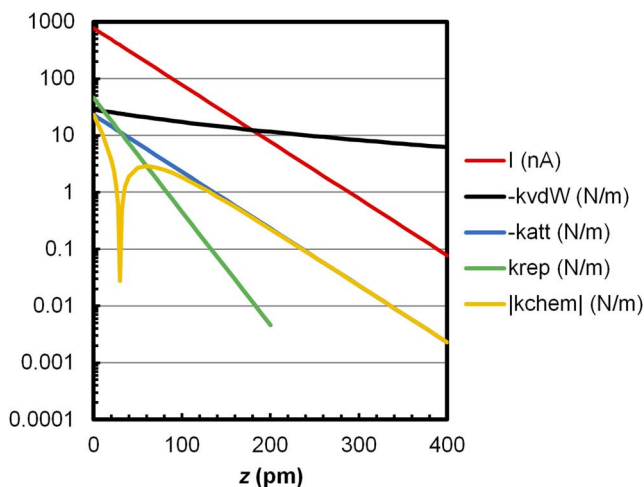


**FIG. 3.** Logarithmic display of tunneling current  $I$ , gradients of van der Waals force  $k_{\text{vdW}}$ , and chemical bonding force  $k_{\text{chem}}$  composed of attractive ( $k_{\text{att}}$ ) and repulsive ( $k_{\text{rep}}$ ) components. The gradient of the forces, in particular, the repulsive component shown in red, dominates the interaction for small distances. In frequency modulation AFM, the frequency shift is proportional to the force gradient if the amplitude is small compared to the interaction length; therefore, the use of small amplitudes results in a strong contribution of the repulsive Pauli exclusion forces that occur when atoms are touching each other.

Therefore, a direct coupling of the force gradient to the frequency shift provided by small amplitude FM-AFM is an ideal way to maximize the sensitivity to short-range forces.

### 3. Deconvolution of forces from frequency shifts

The origin of the experimentally observed frequency shift is force gradients in the tip-sample force. For infinitely small amplitudes  $A$ , the frequency shift is proportional to the force gradient, but for larger amplitudes, a convolution as explained in Eq. (5) takes place. The reverse process, a deconvolution, can be obtained by a matrix inversion as introduced in 2001 in Ref. 84 or by using the more popular Sader-Jarvis algorithm<sup>206</sup> that was introduced three years later. In principle, the matrix inversion is accurate, but it is quite sensitive to the accuracy of the oscillation amplitude.<sup>256</sup> For example, if a frequency shift spectrum has been recorded at an amplitude of  $A = 50$  pm, but the deconvolution is processed for  $A = 55$  pm, spikes and errors can result. The Sader-Jarvis algorithm<sup>206</sup> is more stable against inaccuracies of the oscillation amplitude but may result in deconvolution errors up to 5%. Recently, Sader *et al.* found that some inversion problems of frequency shift into force are even ill-posed, and well-posed inversions may only be possible by choosing amplitudes  $A$  that are either larger or smaller than the specific thresholds, as outlined in Refs. 207 and 208, depending on the characteristics of the force law.

### B. Noise

If the frequency of the force sensor could be measured with infinite accuracy, infinitely small force gradients could be measured. In practice, there is noise, and four relevant noise contributions can be distinguished. Thermal noise has already been discussed in the first article about FM-AFM by Albrecht *et al.*<sup>2</sup> A different source of noise (detector noise) has been described by Dürig in 1997 [Eq. (11) in Ref. 48]. For large bandwidths  $B$ , i.e., for large scanning speeds, deflection detector noise is dominant as it increases with  $B^{3/2}$ . Two other noise sources, thermal noise and oscillator noise, increase with the square root of bandwidth  $B$ . The fourth noise source is due to sensor frequency drifts that can be caused by temperature changes. As we measure an average force gradient in FM-AFM, the noise in this figure is given with Eq. (4),

$$\delta k_{\text{ts}} = 2k \frac{\delta f}{f_0}. \quad (11)$$

#### 1. Thermal noise

The thermal noise of a force sensor at a bandwidth  $B$  is already discussed in Eq. (1) of the first article about frequency modulation AFM,<sup>2</sup>

$$\frac{\delta f_{\text{thermal}}}{f_0} = \sqrt{\frac{k_B T B}{\pi k A^2 f_0 Q}}. \quad (12)$$

According to the equipartition theorem, every degree of freedom holds an energy of  $k_B T/2$ , i.e., a harmonic oscillator contains an energy of  $k_B T$  due to its kinetic and potential energy degrees of freedom, while the energy of the oscillator

is given by  $kA^2/2$  when it oscillates at amplitude  $A$ . The relative thermal frequency noise is therefore related to the square root of the quotient between thermal energy and total energy multiplied by the ratio between bandwidth and eigenfrequency divided by the quality factor. Ultimately, the relevant quantity in an AFM measurement is the force gradient between the tip and the sample, and the thermal noise in force gradient measurement is given by

$$\delta k_{ts thermal} = \sqrt{\frac{4kk_B TB}{\pi A^2 f_0 Q}}. \quad (13)$$

The absolute thermal frequency noise after Eq. (12) is given by an integral of a thermal noise density  $n_{\Delta f thermal}$  from modulation frequency  $f_{mod}$  from 0 up to bandwidth  $B$  with

$$\delta f_{thermal} = \sqrt{\int_0^B n_{\Delta f thermal}^2 df_{mod}}. \quad (14)$$

With this integral, the noise density of thermal noise is constant with respect to frequency (white thermal noise),

$$n_{\Delta f thermal} = \sqrt{\frac{k_B T f_0}{\pi k A^2 Q}}. \quad (15)$$

## 2. Deflection detector noise

The precision of all length measurements, including the measurement of the deflection of a cantilever, is compromised by noise. The precision of the deflection detection can be described by a deflection detector noise density  $n_q$ . For example, with  $n_q = 100 \text{ fm}/\sqrt{\text{Hz}}$ , the error in deflection measurement is  $\delta q = n_q \sqrt{B}$  with  $\delta q = 100 \text{ fm}$  at a bandwidth of  $B = 1 \text{ Hz}$  and  $\delta q = 1 \text{ pm}$  at  $B = 100 \text{ Hz}$ . Typically, the oscillation frequency of the cantilever varies very little around the eigenfrequency  $f_0$ , and we can therefore assume a constant deflection detector noise density  $n_q$  for frequencies around  $f_0$ . If  $n_q$  was zero, a single oscillation cycle would allow an infinitely precise measurement of the oscillation period  $\Xi$  and its inverse, the oscillation frequency  $f$ . Figure 4 shows two oscillation cycles of a cantilever as it can be observed on an oscilloscope. The oscillation period  $\Xi$  is given by the time difference between two consecutive zero crossings, and the uncertainty of each zero crossing is given by the error in deflection measurement  $\delta q' = 2n_q \sqrt{B}$  divided by the slope of the deflection curve that is given by  $\omega \cdot A$  with  $\omega = 2\pi \cdot f$  and oscillation amplitude  $A$ . If only one oscillation cycle was available for frequency measurement, the relative precision of the frequency measurement would be

$$\frac{\delta f_{sensor}}{f_0} \approx \frac{\delta \Xi}{\Xi} = 4 \frac{n_q \sqrt{B}/(2\pi f_0 A)}{1/f_0} = \frac{2}{\pi} \frac{n_q \sqrt{B}}{A}. \quad (16)$$

However, if the bandwidth is smaller than  $f_0$ , a larger number of oscillation cycles given by  $f_0/B$  is available for frequency measurement, and the precision is greatly enhanced, yielding a frequency uncertainty due to detector noise given by

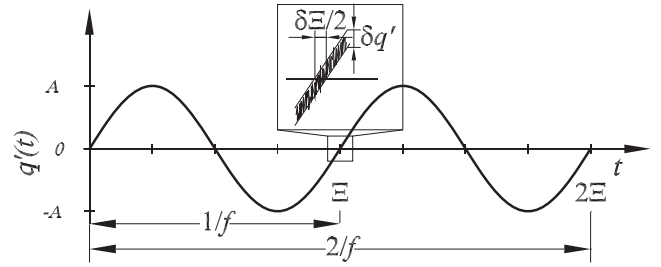


**FIG. 4.** Typical cantilever deflection signal as it appears on an oscilloscope. The deflection of the cantilever  $q'(t)$  is subject to an error  $\delta q' = 2 \cdot n_q B^{1/2}$ .<sup>43</sup> Therefore, the oscillation period of a single oscillation cycle is subject to an error  $\delta \Xi$  given by  $\delta q'$  divided by the slope of the deflection curve at the zero crossing (see text). The oscillation frequency is given by the inverse time lag between two consecutive zero-crossings with positive velocity. If  $N$  oscillation cycles are used for frequency measurement (corresponding to a bandwidth  $B = f/N$ ), the accuracy increases by a factor  $N$  and the frequency error due to detector noise is proportional to  $B^{3/2}$  (Fig. 2.16 in Ref. 167). From *Noncontact Atomic Force Microscopy*, edited by Morita et al. Copyright 2002 Springer. Reprinted with permission from Springer.

$$\frac{\delta f_{sensor}}{f_0} \approx \frac{2}{\pi} \frac{n_q B^{3/2}}{f_0 A}. \quad (17)$$

A more precise calculation<sup>50,105,146</sup> yields a slightly larger prefactor (0.816 vs. 0.637),

$$\frac{\delta f_{sensor}}{f_0} = \sqrt{\frac{2}{3}} \frac{n_q B^{3/2}}{A f_0}. \quad (18)$$

With Eq. (11), we find

$$\delta k_{ts sensor} = \sqrt{\frac{8}{3}} \frac{k n_q B^{3/2}}{f_0 A}. \quad (19)$$

The noise density of detector noise is increasing linearly with frequency (blue noise),

$$n_{\Delta f detector} = \sqrt{2} \frac{n_q}{A} f_{mod}. \quad (20)$$

## 3. Oscillator noise

In 2009, Kobayashi et al.<sup>146</sup> described an additional contribution to frequency noise in FM-AFM that is inversely proportional to  $Q$  and therefore is significant, in particular, in low  $Q$  environments. This contribution is not explicitly temperature dependent and thus can become significant at low temperatures where thermal noise becomes small. The origin of this noise is a consequence of driving the cantilever with its own phase shifted ( $\pi/2$ ) and noisy (due to a finite  $n_q$ ) oscillation signal. The lower the  $Q$  value, the more of this noise pushes the cantilever at the correct phase. Therefore, this noise contribution is proportional to  $n_q$  and inversely proportional to  $Q$ ,

$$\frac{\delta f_{osc}}{f_0} = \frac{n_q B^{1/2}}{\sqrt{2} A Q}. \quad (21)$$

With Eq. (11), we find

$$\delta k_{ts osc} = \sqrt{2} \frac{k n_q B^{1/2}}{Q A}. \quad (22)$$

Similar to thermal noise, oscillator noise is proportional to the square root of the detection bandwidth  $B$  and inversely proportional to amplitude. While thermal noise also decreases with increasing  $Q$  proportional to  $1/\sqrt{Q}$ , oscillator noise is proportional to  $1/Q$ ; thus of all noise sources, it is most sensitive to the quality factor. The noise density of oscillator noise is constant with respect to frequency (white noise),

$$n_{\Delta f \text{ oscillator}} = \frac{f_0 n_q}{\sqrt{2} A Q}. \quad (23)$$

#### 4. Frequency drift noise

All of the three noise sources discussed so far increase with bandwidth. In principle, those noise sources can be made infinitely small by reducing the bandwidth and thus the scanning speed. Thermal drift prevents the acquisition of images or spectra at infinitely small speeds. First, the scanning probe microscope itself will drift with changes in temperature or for other reasons such as piezo creep. Second, the cantilever will not maintain a constant oscillation frequency. Changes in temperature, aging, or other factors cause the oscillation frequency to drift with time. Thermal drift is a challenge for room temperature measurements and, in particular, for high-temperature measurements. The oscillation frequency of a sensor will change slightly even in liquid helium environments, e.g., induced by slight changes in the boiling temperature induced by variations in ambient pressure.

We can compute the power spectral density of the frequency drift noise contribution by taking a Fourier transform of the square of the frequency drift. If the sensor frequency drifts linearly with time at a drift rate  $r$ , we find  $\delta f(t) = r \cdot t$  within a time interval  $[-\tau/2 \dots \tau/2]$ . With  $\Omega = 2\pi/\tau$ , we can express the time dependence of the frequency as

$$\delta f^2(t) = \sum_{n=0}^{\infty} a_n \cos(n\Omega t) \quad (24)$$

with Fourier coefficients

$$a_n = \frac{\Omega}{\pi} \int_{t=-\tau/2}^{\tau/2} r^2 t^2 \cos(n\Omega t) dt \quad (25)$$

and

$$a_n = (-1)^n \frac{r^2 \tau^2}{\pi^2 n^2}. \quad (26)$$

We can now interpret  $|a_n|$  as the equivalent power component at a frequency  $f_{\text{mod}} = n/\tau$  in a frequency interval of  $1/\tau$ . Therefore, the power spectral density (power per frequency) becomes

$$n_{\Delta f \text{ drift}}^2(f_{\text{mod}}) = \frac{r^2 \tau}{\pi^2 f_{\text{mod}}^2} \quad (27)$$

and

$$n_{\Delta f \text{ drift}}(f_{\text{mod}}) = \frac{r\sqrt{\tau}}{\pi f_{\text{mod}}}. \quad (28)$$

Thus, a linear frequency drift leads to  $1/f$  noise in the frequency spectrum of the phase-locked-loop (PLL) output. The magnitude of this noise component depends on the drift rate

of the frequency  $r$  and the measurement period  $\tau$ . The time period  $\tau$  is at least the time it takes to complete one image. Thus, for fast measurements, frequency drift noise can be reduced provided that the frequency detector (PLL) is reset before an image is taken. To obtain the effect of this noise on the force gradient measurement, we need to multiply  $n_{\Delta f}(f_{\text{mod}})$  by  $2k/f_0$  [see Eq. (4)] to obtain

$$n_{k_{ts} \text{ drift}}(f_{\text{mod}}) = \frac{2kr\sqrt{\tau}}{f_0 \pi f_{\text{mod}}}. \quad (29)$$

The noise density of drift noise is inverse with frequency ( $1/f$  or pink noise),

$$n_{\Delta f \text{ drift}} = \frac{r\sqrt{\tau}}{\pi f_{\text{mod}}}. \quad (30)$$

The effect of thermal drift noise for qPlus sensors and needle sensors will be discussed in detail in Subsection IV B 4.

#### 5. Summary of noise calculations

To assess the various noise contributions regarding their impact on the precision of measuring the tip-sample force gradient, we express the four noise sources in terms of  $k_{ts}$ . The errors in measuring  $k_{ts}$  are evaluated by squaring the density expressions, integrating them in a modulation frequency interval from  $f_{\text{mod}}$  from  $1/\tau$  to  $B$  where  $\tau$  is the time needed to acquire the image,

$$\delta k_{ts \text{ thermal}} = \sqrt{\frac{4kk_B TB}{\pi A^2 f_0 Q}}, \quad (31)$$

$$\delta k_{ts \text{ sensor}} = \sqrt{\frac{8}{3}} \frac{k n_q B^{3/2}}{f_0 A}, \quad (32)$$

$$\delta k_{ts \text{ osc}} = \sqrt{2} \frac{k n_q B^{1/2}}{Q A}. \quad (33)$$

For the first three noise sources, we can set the lower modulation frequency to zero, but drift noise would diverge for infinitely long measurement times, requiring a finite lower threshold  $B_{\text{min}} = 1/\tau$ ,

$$\delta k_{ts \text{ drift}}(f_{\text{mod}}) = \frac{2kr\sqrt{\tau}}{f_0 \pi} \sqrt{\tau - 1/B}. \quad (34)$$

As  $B \gg 1/\tau$ , the noise in  $k_{ts}$  due to drift is proportional to the drift rate  $r$  times the time it takes to acquire the image  $\tau$ . If we assume to acquire an image with  $N$  pixels, we find  $\tau \approx N/B$  and

$$\delta k_{ts \text{ drift}}(f_{\text{mod}}) \approx \frac{2krN}{f_0 \pi B}. \quad (35)$$

These four noise sources are statistically independent, and the net effect of statistically independent variables is computed by taking the square root of the sum of squares.

The summary of noise calculations allows us to identify important conclusions about ideal properties of the force sensor. The first three noise sources are all inversely proportional to  $A$ , i.e., they appear to suggest the use of infinitely large amplitudes. However, we will see in Sec. II C that for



maximizing the signal-to-noise ratio, finite amplitudes on the order of the decay length of the forces are optimal. The stiffness  $k$  affects all noise sources: thermal noise increases as  $\sqrt{k}$ , and oscillator noise, frequency drift noise, and drift noise are proportional to  $k$ . Therefore, we recommend that  $k$  should be large enough to enable stable sensor oscillations as discussed in Eqs. (2) and (3) at the optimal amplitude but should otherwise be as small as possible. High  $Q$ -values are desirable to minimize thermal and oscillator noise. The frequency drift noise can be minimized by using a sensor material with little frequency change as a function of temperature and by operating the sensors in a thermally stable environment, preferentially at temperatures at or close to the turnover temperature  $T_p$  [see Eq. (77)]. The noise performance of the electrical amplifier is critical to minimize deflection detector noise.

### C. Signal-to-noise ratio

Using the calculations for the frequency shift and for noise, we can now calculate the signal-to-noise ratio. When increasing the amplitude from zero, we found in Eq. (8) that the frequency shift remains almost constant until the amplitude reaches the range of the interaction and then decreases proportionally to  $1/A^{3/2}$ . The noise in the frequency measurement of the sensor is inversely proportional to  $A$ ; therefore, the signal-to-noise ratio (SNR) can be expressed as

$$\text{SNR} \propto e^{-A/\lambda} I_1(A/\lambda). \quad (36)$$

This function is plotted in Fig. 5; it has its maximum at  $\kappa A = 1.5451\dots$ ; thus, the optimal signal-to-noise ratio is reached

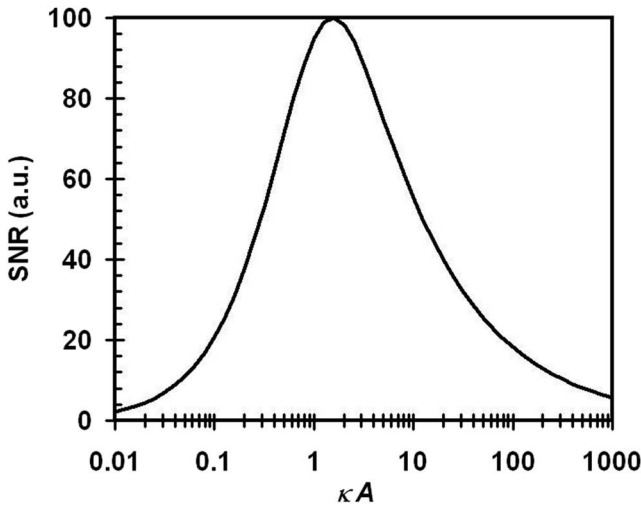


**FIG. 5.** Signal-to-noise-ratio (SNR) as a function of the product between decay constant  $\kappa$  and amplitude  $A$  or ratio  $A/\lambda$  with decay length  $\lambda = 1/\kappa$ . Optimal SNR is obtained for  $A_{\text{opt}} = 1.545\lambda$ , equivalent to  $\kappa A_{\text{opt}} = 1.545$ . The decrease in SNR for non-optimal amplitudes is asymmetric with  $\log(A)$ , choosing  $A = 0.1A_{\text{opt}}$  or  $A = 100A_{\text{opt}}$  both yield approximately twenty percent of the ideal SNR. Reprinted with permission from Giessibl *et al.*, Phys. Rev. B **84**, 125409 (2011). Copyright 2011 The American Physical Society.

for amplitudes that correspond to the decay length  $\lambda = 1/\kappa$  of the tip-sample force,<sup>80</sup> or more precisely,  $A_{\text{opt}} \approx 1.545\lambda$ . In theory, this ideal amplitude applies to all sensors in FM-AFM that probe interactions of range  $\lambda$ , provided the sensor stiffness is sufficient to enable stable oscillation close to the surface.<sup>78</sup>

While the ideal amplitude for an optimal signal-to-noise-ratio is  $A/\lambda \approx 1.545$ , we still have to consider the influence of the choice of amplitude to the signal strength of the desired observable. For example, if the interaction is composed by a repulsive interaction with a decay length of 20 pm and an attractive interaction with a decay length of 50 pm, the ideal amplitude for maximizing SNR for the repulsive branch would be about 30 pm, while the optimal SNR in the attractive branch would result for  $A \approx 75$  pm. Even when probing the repulsive regime, using an amplitude even smaller than 30 pm can be beneficial to suppress more of the attractive contribution (see Fig. 1).

### D. Dissipative forces

When the tip-sample forces vary between forward and backward traces during tip oscillation, the force field is no longer conservative. Generally, dissipative processes lead to an energy loss, while in some cases with nonzero tip-sample bias voltages, discharging effects can also cause an energy transfer from the tip-sample system to the cantilever. In this case, the amplitude feedback circuit needs to alter its drive signal. When the cantilever oscillates in a conservative force field, the drive amplitude for an optimally adjusted phase is given by

$$A_{\text{drive}} = \frac{A}{Q}, \quad (37)$$

where  $Q$  is the quality factor of the sensor. For a proper adjusted phase in the oscillation controller, the phase of the cantilever lags by  $\phi = -\pi/2$  with respect to the drive; i.e., for a drive signal given by

$$q_{\text{drive}}(t) = A_{\text{drive}} \cos(2\pi ft), \quad (38)$$

the cantilever oscillates according to

$$q'(t) = A \sin(2\pi ft). \quad (39)$$

The purpose of the drive signal is to make up for energy that is lost by internal friction in the force sensor. This loss per oscillation cycle is given by

$$\Delta E_{\text{cl}} = \pi \frac{kA^2}{Q}. \quad (40)$$

If the tip-sample force is not conservative, the integral over one oscillation cycle (running from  $q' = -A$  to  $q' = A$  and back to  $q' = -A$ )

$$\Delta E_{\text{ts}} = \oint F_{\text{ts}}(z + q') dq' \quad (41)$$

is nonzero, and the drive amplitude needs to adjust from  $A_{\text{drive}}$  to  $A'_{\text{drive}}$  given by

$$A'_{drive} = A \frac{\Delta E_{cl} + \Delta E_{ts}}{\pi k A^2} = A \left( \frac{1}{Q} + \frac{\Delta E_{ts}}{\pi k A^2} \right). \quad (42)$$

The energy dissipation can then be extracted from  $A'_{drive}$  by [similar to Eq. (4) in Ref. 35 for the special case  $\phi = \pi/2$  as noted above]

$$\Delta E_{ts} = \frac{\pi k A^2}{Q} \left( \frac{A'_{drive}}{A_{drive}} - 1 \right). \quad (43)$$

Monitoring  $A_{drive}$  thus allows us to record the dissipation as a function of position in addition to conservative forces.

### E. Higher harmonics

The oscillation frequency is the main observable in FM-AFM. If the cantilever vibrates in a nonharmonic potential, a shift in frequency is not the only change in cantilever oscillation. In addition, we observe the emergence of higher harmonics  $a_2, a_3, \dots$  in the cantilever oscillation with its main amplitude  $A = a_1$ . Dürig<sup>49</sup> has found a highly elegant method to calculate the higher harmonics in the cantilever motion that links the higher harmonics to an expansion of  $F_{ts}$  in terms of Chebyshev polynomials.

The cantilever motion is assumed to be periodic; therefore, it is expressed as a Fourier series with fundamental frequency  $f$ ,

$$q'(t) = \sum_{n=0}^{\infty} a_n \cos(n2\pi ft). \quad (44)$$

The static deflection  $a_0$  is the average tip-sample force divided by the stiffness of the cantilever, while  $a_1$  is just the unperturbed oscillation amplitude  $A$ . For  $n > 1$ , the amplitudes  $a_n$  are given by

$$a_n = \frac{2}{\pi k} \frac{f_0^2}{f_0^2 - n^2 f^2} \int_{-1}^1 F_{ts}(z + a_1 u) T_n(u) \frac{du}{\sqrt{1-u^2}}. \quad (45)$$

Because  $f \approx f_0$  and  $a_1 = A$ ,

$$a_n = \frac{2}{\pi k} \frac{1}{1-n^2} \int_{-1}^1 F_{ts}(z + Au) T_n(u) \frac{du}{\sqrt{1-u^2}}. \quad (46)$$

In 2004, we<sup>112</sup> realized that integration by parts allows us to express the higher harmonics in a more intuitive way,

$$a_n = \frac{2}{\pi k} \frac{1}{1-n^2} \frac{1}{1 \cdot 3 \cdot \dots \cdot (2n-1)} A^n \times \int_{-1}^1 \frac{dF_{ts}^{(n)}(z + Au)}{dz^{(n)}} (1-u^2)^{n-1/2} du. \quad (47)$$

The  $n$ th harmonic is a convolution of the  $n$ th force gradient with a weight function with a sharpness that increases with  $n$ . Figure 6 shows these weight functions. For exponential force laws, explicit solutions are available. With  $F(z) = F_0 \exp(-\kappa z)$ , we find

$$a_2 = \frac{2}{3k} F_0 \exp(-\kappa z) \left[ I_0(\kappa A) - 2 \frac{I_1(\kappa A)}{\kappa A} \right], \quad (48)$$

where  $I_n(z)$  is a modified Bessel function of the first kind.<sup>1</sup> The results of these calculations are also applicable for amplitude modulation AFM (Ref. 20). Because of the link of higher harmonics to higher force gradients, the method is well

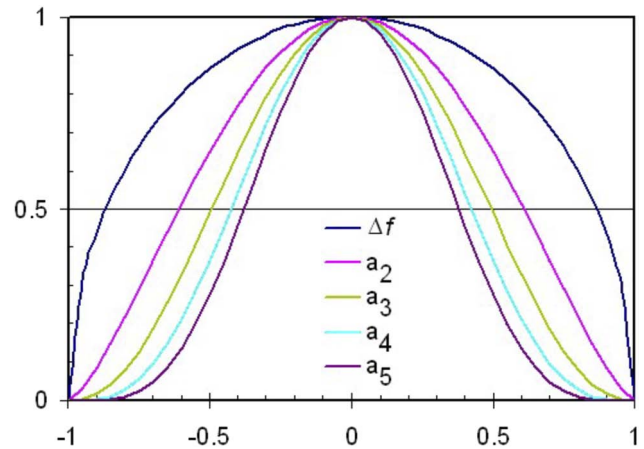


**FIG. 6.** Weight functions  $w_n(q'/A)$  to derive frequency shift  $\Delta f$  (semicircle) and higher harmonics  $a_n$  (more and more bell-shaped with larger  $n$ ). The frequency shift of an oscillating cantilever is given by a convolution of the force gradient  $k_{ts} = -dF_{ts}/dz$  with the semicircular weight function  $w_1(u) = (1-u^2)^{1/2}$  [see Eq. (5)], while the  $n$ th harmonic  $a_n$  is given by a convolution of the  $n$ th derivative of the force  $d^n F_{ts}/dz^n$  with the corresponding weight function  $w_n(u) = (1-u^2)^{n-1/2}$  [see Eq. (47)]. The horizontal axis displays the ratio  $u = q'/A$  between cantilever deflection  $q'$  and amplitude  $A$ .

suited for very high resolution. However, even for small distances with strong interactions, higher harmonics are often very small on the order of 100 fm, although piezoelectric detection as present in qPlus sensors increases the magnitude of higher harmonics.<sup>91</sup>

### F. Simultaneous work function measurements

The tunneling current follows an exponential distance law

$$I(z) = I_0 \exp(-\kappa z), \quad (49)$$

where the decay constant  $\kappa$  is linked to the work function  $\Phi$ ,

$$\kappa = \sqrt{2m_e \Phi}/\hbar, \quad (50)$$

with electron mass  $m_e$ . When performing simultaneous STM and AFM, the oscillating tip of course modulates the tunneling current and the extent of the modulation allows information about the work function.<sup>115,124</sup>

## III. THE qPLUS SENSOR AND ITS OBJECTIVE TO EMBODY AN IDEAL SENSOR FOR FM-AFM

As FM-AFM utilizes frequency to measure force gradients, the frequency stability of the sensor is critical. It is worthwhile to study the frequency standards that have been developed in the art and science of watchmaking. Quartz oscillators come in various geometries, mainly determined by the oscillation frequencies. Quartz watches typically use tuning forks that oscillate at a frequency of  $2^{15}$  Hz [see Figs. 7(b) and 8(a)], and tuning fork geometries are available in eigenfrequencies up to several 100 kHz, although some use a second flexural mode to reach high Q factors for frequencies above 100 kHz. For higher frequencies, length extensional resonators [LER, see Fig. 8(e)] are used<sup>6,242</sup> that oscillate at typical frequencies of 1 MHz. Even

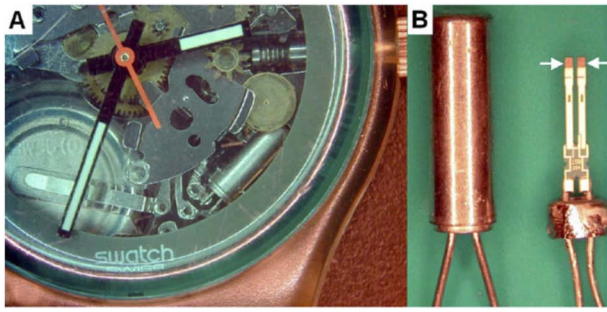


**FIG. 7.** (a) Swatch wristwatch with a transparent case.<sup>87</sup> The timekeeping element is a quartz tuning fork housed in an evacuated metal can (right bottom of the watch). (b) Encapsulated tuning fork (left) and tuning fork with open case (right). The high  $Q$  factor is obtained because each of the two tines is calibrated by laser ablation [reddish parts indicated by arrows on (b) right] to obtain an eigenfrequency of exactly  $2^{15}$  Hz. The two tines vibrate in an antiparallel mode such that the dynamic forces are exactly compensated. Reproduced with permission from Giessibl *et al.*, *Nanotechnology* **15**, 84 (2004). Copyright 2004 IOP Publishing.<sup>87</sup>

higher frequencies in the range up to 100 MHz and higher are using plates or disks that vibrate in a shear mode (not shown here). The quartz watch is a promising candidate to check if its oscillator core can be transformed to a useful sensor in AFM. A quartz tuning fork not only keeps time at an excellent precision but also provides an electrical deflection signal, uses little power, and therefore does not produce large heat loads for low temperature microscopes.

A key design element of a quartz tuning fork is its high symmetry, where two prongs oscillate opposite to each other. These two prongs form two coupled oscillators. In an AFM, we only have one tip, so the attachment of a tip breaks the symmetry. While the mass of the tip can be compensated, the tip-sample force gradient would only act on one of the two coupled oscillators, leading to a drastic reduction in the  $Q$  factor, beating modes and other problems. In the first designs of the qPlus sensor, one of the prongs was attached to a very heavy substrate such that only a quartz cantilever and thus a single cantilever remained. Thus it is more

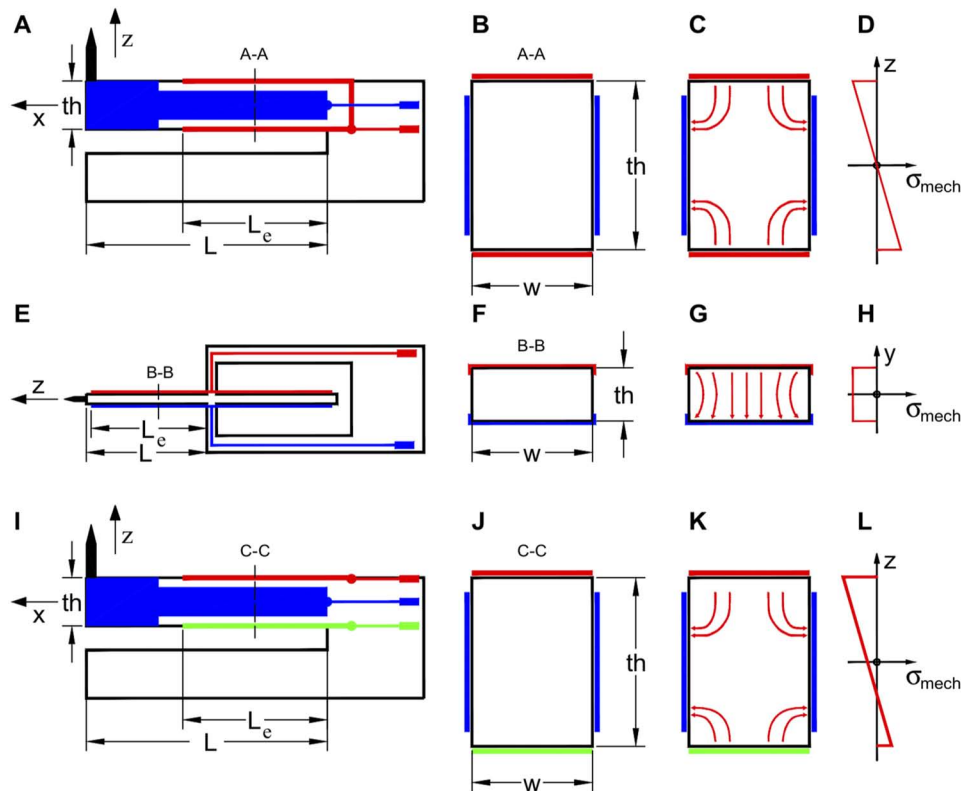


**FIG. 8.** Geometry (see Table I), electrode placement, electric field distribution upon deflection, and mechanical strain for a standard qPlus sensor [(a)–(d)], a length extensional resonator [(e)–(h)], and a novel biaxial qPlus sensor design [(i)–(l)] that aims to detect  $z$  and  $x$ -directions simultaneously. (a) shows a standard qPlus sensor. (b) shows the cross section of the beam and the placement of the electrodes. The top and bottom electrodes (red, named A in Fig. 11) are connected, as are the side electrodes (blue, named B in Fig. 11). (c) shows the distribution of the electric field when the beam is deflected. (d) shows the strain distribution of the deflected beam. The needle sensor (e) is built by attaching a light tip to one prong of the length extensional resonator and has a longitudinal vibrational eigenmode. Because of the longitudinal mode, the cross section of the beam (f) develops an almost uniform electric field distribution (g) with uniform strain distribution (h). [(i)–(l)] show a combination of the standard qPlus sensor and a LER sensor. The top and bottom electrodes shown in (j) are split into two with electrode A (red), electrode A' (green), and electrodes B (blue). This design allows us to excite two different modes, a bending mode in the  $z$ -direction that is read out by measuring the difference between the charges generated by electrodes A + A' and B, and a longitudinal mode in the  $x$ -direction that is measured by the difference between the charges generated by electrodes A and A'.

accurate to find this new name “qPlus sensor” rather than calling it “tuning fork sensor” (see also the discussion in Ref. 92 regarding coupled and single oscillators). The detrimental impact of mass imbalance on the quality factor of tuning forks has been studied in Ref. 204. Due to their simple use, quartz tuning forks were adopted early in scanning probe microscopy. Dransfeld *et al.*<sup>45,99</sup> used quartz tuning forks as a sensor in near field acoustic microscopy in 1989, and in 1993, Bartzke *et al.* transformed a 1 MHz quartz length extensional resonator into the so-called needle sensor by attaching a tip to one of the extensional beams.<sup>13,14</sup> Tuning forks were also successfully used in scanning near field optical microscopy by Karrai *et al.*<sup>136,137</sup> Quartz tuning forks have been used successfully as sensors in AFM using normal forces in the group of Siria.<sup>31</sup> The group of Jhe studied the influence of a liquid layer in ambient conditions manifested in shear force interactions,<sup>8,143,153</sup> as well as the wetting mechanism of titania<sup>152</sup> using quartz tuning fork sensors.

Figure 8 shows the geometry, the electrode placement, and the electric field in the oscillating quartz sensor for the qPlus geometry, the length extensional resonator, and a novel biaxial qPlus sensor that is currently in development. A standard qPlus sensor [see Fig. 8(a)] is created by attaching one of the prongs of the tuning fork to a substrate and attaching a tip to the other prong. The prong without displayed electrodes is fixed to a massive substrate (not shown here, see Fig. 10). The custom built qPlus sensors only have electrodes on their single beam (see Fig. 11). The arrangement of the electrodes in Fig. 8(b) becomes clear when looking at the stress distribution in the beam when it is bent downwards (C), where tensile stress (D) occurs in the upper half of the cross section and compressive stress in the lower half. Therefore, the electric field vector is pointing to opposite directions in the upper and lower halves of the cross section and the surface charges on the red electrodes on the top and bottom have an equal sign. Lateral electrodes are needed to collect the opposite charges.

Quartz tuning forks and quartz length extensional resonators consist of two coupled oscillators. The high Q value they reach is due to the perfect antisymmetric oscillation. The invention of the qPlus sensor transformed the two coupled oscillators that build up a tuning fork to one single high Q oscillator. The analysis of the first successful noncontact AFM experiment of 1995<sup>71</sup> published in 1997<sup>78</sup> made it clear that small amplitudes and stiff cantilevers were needed. It turned out that the spring constants of the quartz tuning forks used in Swatch watches (see Fig. 7) were very close to the ideal stiffness that was wanted for an atom-resolving cantilever.<sup>80</sup> The first qPlus sensors were built using tuning forks and immobilizing one of the beams by attaching it to a heavy substrate; later custom designed versions have only a single oscillating beam from the start.

### A. Calculation of stiffness, eigenfrequency, and sensitivity

#### 1. qPlus sensor

For a rectangular beam with width  $w$ , thickness  $th$ , and length  $L$ , the spring constant  $k$  is given by<sup>33</sup>

$$k = \frac{E_Y \cdot w \cdot th^3}{4L^3}, \quad (51)$$

where  $E_Y$  is Young's modulus. For a harmonic oscillator, the eigenfrequency is given by  $f_0 = \sqrt{k/m^*}$ , where  $m^*$  is the effective mass. For a beam with length  $L$ , width  $w$ , height  $th$  (see Fig. 8), a constant cross section, and constant mass density  $\rho$ , the effective mass is given by  $m^* = 0.243 m = 0.243 \cdot \rho \cdot w \cdot th \cdot L$ ;<sup>33</sup> thus, the fundamental eigenfrequency  $f_0$  is given by

$$f_0 = 0.162 \cdot \frac{th}{L^2} \cdot v_s, \quad (52)$$

where  $v_s$  is the speed of sound in quartz given by  $v_s = \sqrt{E_Y/\rho}$ .

The calculation of the sensitivity has been performed for the qPlus sensor in Ref. 81 and for the needle sensor (LER) in Ref. 92, and we reproduce the calculation that leads to the sensitivities from Refs. 81 and 92 in the remainder of this subsection. When a force  $F = kz'$  is acting on the upper prong, the strain  $\epsilon$  at the upper side is given by

$$\epsilon(x, z = th/2) = \frac{th \cdot F \cdot (x - L)}{2 \cdot E_Y \cdot J}, \quad (53)$$

where  $E_Y$  is Young's modulus and  $J$  is the moment of inertia  $J = w \cdot th^3/12$ . This strain causes a stress  $\sigma_{mech} = \epsilon E$  which leads to a surface charge density  $\sigma_{charge} = \sigma_{mech} d_{21}$ , where  $d_{21}$  is the piezoelectric coupling constant ( $d_{21} = 2.31 \cdot 10^{-12}$  C/N for quartz).<sup>33</sup> The lower side of the bent prong also has a charge density  $\sigma_{charge}$  (both  $\epsilon$  and the  $z$ -component of the surface normal vector have opposite signs) and contributes an equal amount to the total charge  $q$ . Integrating  $\sigma_{charge}$  from  $x = 0$  to  $x = L_e$  (=length of the electrodes) and  $y = -w/2$  to  $w/2$  yields

$$q/z' = 12 \cdot d_{21} \cdot k \cdot L_e (L - L_e/2) / th^2. \quad (54)$$

With  $z' = A \cos(2\pi f \tau)$  and  $L_e \approx 1.6$  mm, the expected output voltage per deflection is  $S_v \approx 2\pi f \cdot R \cdot 2.8 \mu\text{C}/\text{m}$ , and with  $f = 25\,800$  Hz and  $R = 100$  M $\Omega$ , we find  $S_v^{\text{theory}} \approx 45 \mu\text{V}/\text{pm}$ ,

$$S_{q\text{Plus}}^{\text{theory}} = q_{el}/A = 12 \cdot d_{21} \cdot k \cdot \frac{L_e (L - L_e/2)}{th^2}. \quad (55)$$

Standard qPlus sensors with the dimensions listed in Table I yield  $S_{q\text{Plus}}^{\text{theory}} = 2.8 \mu\text{C}/\text{m}$ . It is important to note that the calculated sensitivity is based on an idealized homogeneous field distribution, as shown in Fig. 3(e) of Ref. 92, while the actual field looks more like Fig. 8(c). In practice, the actual sensitivity typically only reaches about half of this theoretical value.<sup>255</sup>

#### 2. Needle sensor (length extensional resonator)

The needle sensor consists of two coupled beams that oscillate opposite to each other [see Fig. 8(e)]. The longitudinal stiffness of  $k'$  of each of the two bars that constitute the needle sensor is given by

$$k' = \frac{E \cdot w \cdot th}{L}, \quad (56)$$

with Young's modulus  $E$ , length  $L$ , width  $w$ , and thickness  $th$  of each quartz beam. The fundamental eigenmode is a



**TABLE I.** Geometrical parameters, stiffness  $k$ , eigenfrequency  $f_0$ , charge per deflection  $S_q^{\text{theory}}$ , charge per force  $S_{q/F}^{\text{theory}} = S_q^{\text{theory}}/k$ , and current per force  $S_{I/F}^{\text{theory}} = S_q^{\text{theory}} 2\pi f_0/k$  of the quartz oscillators used. The qPlus sensor has a single beam with length  $L$ , width  $w$ , and thickness (height)  $th$ , while the needle sensor features two coupled beams that oscillate in a longitudinal direction opposite to each other (see Fig. 8). Note that the experimental sensitivity reaches typically only 50% of the theoretical value listed above for qPlus sensors, while it matches the theoretical value for the needle sensor.

Type	$L$ ( $\mu\text{m}$ )	$L_e$ ( $\mu\text{m}$ )	$th$ ( $\mu\text{m}$ )	$w$ ( $\mu\text{m}$ )	$k$ (N/m)	$f_0$ (Hz)	$S_q^{\text{theory}}$ (aC/pm)	$S_{q/F}^{\text{theory}}$ (aC/nN)	$S_{I/F}^{\text{theory}}$ (fA/nN)	No. of electrodes
qPlus S1.0d	2360	1600	214	127	1800	32 768	2.8	1.5	319	2
qPlus S1.0	2360	1600	214	127	1800	32 768	2.8	1.5	319	3
qPlus S1.0B	2360	1600	214	127	1800	32 768	2.8	1.5	319	4
qPlus S0.8	1890	1230	214	127	3 600	52 600	3.4	0.95	312	3
qPlus S0.6	1420	700	214	127	9 400	93 500	4.56	0.53	312	3
qPlus S0.4	945	614	214	127	28 900	210 000	6.8	0.24	312	3
qPlus M1	1600	1040	120	130	1 070	41 000	2.3	2.16	558	2
qPlus M2	1200	780	120	130	2 500	73 000	3.1	1.22	558	2
qPlus M3	1000	650	120	130	4 400	105 000	3.7	0.85	558	2
qPlus M4	1000	650	90	130	1 850	79 000	2.8	1.5	744	2
qPlus M5	1000	650	120	130	4 400	105 000	3.7	0.85	558	3
qPlus M5B	1000	650	120	130	4 400	105 000	3.7	0.85	558	4
Needle (LER)	1340	1100	70	130	1 080 000	1 000 000	45	0.083	117	2

longitudinal standing wave with a node at the root of each beam and its end at a maximal deflection; thus, the length of one beam  $L$  corresponds to a quarter wavelength  $\lambda/4$ . Because the velocity of sound is  $v_s = \sqrt{E/\rho}$  with mass density  $\rho$ , the eigenfrequency is given by

$$f_0 = \frac{v_s}{4L}. \quad (57)$$

To calculate the sensitivity of the needle sensor, we note that the deflection of a cross section at a distance  $z$  from the mount is given by

$$\delta z(z) = A \sin\left(\frac{\pi z}{2L}\right) \quad (58)$$

when the ends of the device oscillate at amplitude  $A$ . The strain as a function of  $z$ -position is then given by

$$\epsilon(z) = \frac{\partial \delta z(z)}{\partial z} = \frac{\pi A}{2L} \cos\left(\frac{\pi z}{2L}\right). \quad (59)$$

The strain  $\epsilon$  leads to a mechanical stress  $\sigma_{\text{mech}}$  given by

$$\sigma_{\text{mech}}(z) = E\epsilon(z). \quad (60)$$

The piezoelectric effect causes the emergence of a surface charge density  $\sigma_{\text{el}}$  given by

$$\sigma_{\text{el}}(z) = d_{21}\sigma_{\text{mech}}(z), \quad (61)$$

where  $d_{21} = 2.31$  pC/N is the transverse piezoelectric coupling coefficient of quartz,<sup>246</sup> which is equal to the longitudinal piezoelectric coupling coefficient  $d_{11}$ . It is important to note that  $d_{21}$  is essentially constant over the temperature range from 1.5 K to room temperature.<sup>246</sup> When the charge density is integrated over the surface of the sensor, the total charge  $q_{\text{el}}$  at a given deflection  $A$  is given by

$$q_{\text{el}} = d_{21}w \int_{-L_e}^{L_e} E \frac{A\pi}{2L} \cos\left(\frac{z\pi}{2L}\right) dz. \quad (62)$$

Thus, the sensitivity is given by

$$S_{q\text{LER}}^{\text{theory}} = q_{\text{el}}/A = 2d_{21}Ew \sin\left(\frac{L_e\pi}{2L}\right). \quad (63)$$

With Eq. (56), we can express Eq. (63),

$$S_{q\text{LER}}^{\text{theory}} = 2d_{21}k' \frac{L}{th} \sin\left(\frac{\pi L_e}{2L}\right). \quad (64)$$

The electrodes extend almost to the end of the beams ( $L_e = 1.1$  mm,  $L = 1.34$  mm); therefore, the sine in the equation above is almost one (exact value 0.960 685 188), and with  $L/th = 1340/70$ , we find  $S_{q\text{LER}}^{\text{theory}} \approx 19 \cdot d_{21} \cdot k'$ . With the stiffness  $k' = 540$  kN/m, we find a theoretical sensitivity of  $S_{q\text{LER}}^{\text{theory}} = 45$   $\mu\text{C/m}$ .

### 3. Biaxial qPlus sensor

Figure 8(i) shows the geometry of a biaxial qPlus sensor, where the conventional axis is mapping the  $z$ -direction and the longitudinal axis covers the  $x$ -direction of the tip-sample interaction. The stiffnesses, eigenfrequencies, and sensitivities can be calculated using the formulas for the normal qPlus and LER sensors. The only differences are that (a) needle sensors use two coupled beams with stiffness  $k'$  (540 kN/m for the dimensions shown in Table I) where the effective stiffness is  $k = 2k'$  and for the biaxial qPlus sensor, the stiffness in the  $x$ -direction is  $k_x = k'$  and (b) the sensitivity of the biaxial qPlus sensor in the  $x$ -direction is only half of that of the needle sensor because it only uses one beam. Currently, this sensor is in development, and results are in preparation. The design of this new sensor is described here to motivate the discussion of the properties of the needle sensor here as these are needed for the  $x$ -axis of the biaxial qPlus sensor.

### B. Sensor and its fabrication

To build a qPlus sensor from a quartz tuning fork, we need a heavy substrate to fix one of the two tines and a tip needs to be mounted on the free prong. The first generation of qPlus sensors was built by attaching one leg of an unspecified

tuning fork as used in quartz wristwatches to a small piece of Pyrex glass (Fig. 9). The second generation already featured the tuning forks of the Swatch brand as well as a custom made ceramic substrate<sup>32</sup> with the electrical connections shown in Fig. 10. The fabrication of sensors starts with the assembly of the quartz tuning fork with a rigid insulating substrate, as shown in Fig. 10. Both conductive and nonconductive glues are used in assembly. In 2011, newer versions of the qPlus sensor were invented.<sup>74–76</sup> These sensors only have a single quartz beam and provide separate electrodes for STM current, excitation, and other purposes.

The third generation of qPlus sensors (Fig. 11) has an integrated separate electrode to bias the tip electrically without having to route an extra wire. We also switched to a ceramic substrate with a rectangular shape (as used in the lateral force sensor of Fig. 13) and smoother edges than those used in generation two.<sup>11</sup> The fourth generation of qPlus sensors (Fig. 12) has a total of four electrodes: two for differential deflection detection, one to bias the tip, and one for deflection excitation.

To be able to measure lateral forces,<sup>85,260–262</sup> the sensor can be rotated by 90°, as shown in Fig. 13. In this case, the tip is aligned with the beam of the qPlus sensor.

Table I shows the geometrical parameters of a variety of qPlus sensors along with stiffness, eigenfrequency, and sensitivities. The stiffness  $k$  is a very important parameter for extracting force data from experimental frequency shift. The connection between the geometrical parameters presented in Eq. (51) is linear with sensor width  $w$ , cubic with thickness  $th$ , and inverse cubic with length  $L$ . Therefore, a 3% error in measuring the linear dimensions of the sensor would result

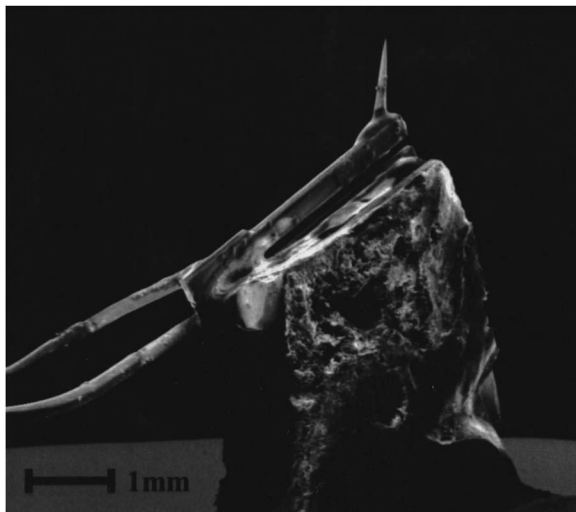


**FIG. 9.** First generation qPlus sensor.<sup>79</sup> A tuning fork extracted from an encapsulated tuning fork with a length of one prong of  $L = 3.0$  mm, thickness  $t = 330$   $\mu\text{m}$ , and width  $w = 120$   $\mu\text{m}$  was used, yielding a stiffness of  $k = 3143$  N/m. One tine of the tuning fork was glued to a small piece of Pyrex glass, the Pyrex glass was glued to a washer made of stainless steel and mounted to the end of a piezoelectric tube scanner.<sup>26</sup> Reproduced with permission from F. J. Giessibl, *Appl. Phys. Lett.* **73**, 3956 (1998). Copyright 1998 AIP Publishing LLC.

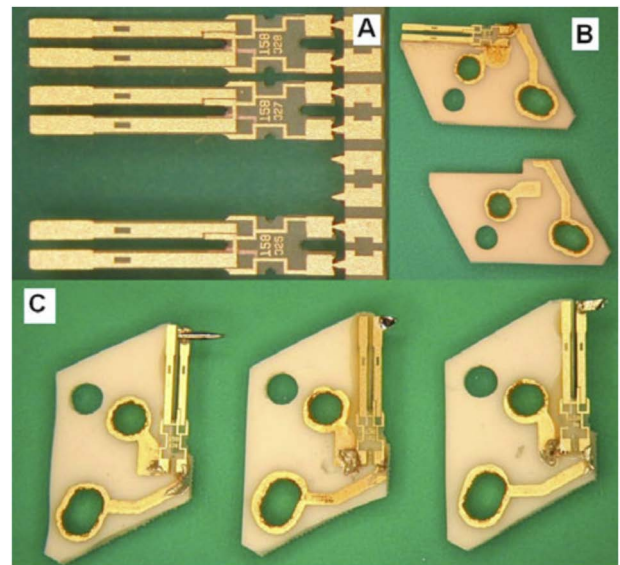


**FIG. 10.** Second generation of qPlus sensors.<sup>87</sup> Here, type E158 tuning forks from the Swiss company Micro Crystal<sup>163</sup> were separated from a wafer (a) and glued onto a specially designed piece of aluminum oxide (CeramTec<sup>32</sup>) with two electrical connections. (b) The tuning fork is glued to a substrate made of alumina ( $\text{Al}_2\text{O}_3$ ) that contains gold plated nickel electrodes to provide for electrical contacts. The tuning fork is glued to the substrate with a nonconductive glue EPO-TEK T7110 or EPO-TEK H70E.<sup>54</sup> (c) Third step of assembly: a tip is added to the free prong of the tuning fork, and the contact leads of the substrate are connected to the electrodes of the tuning fork using a conductive glue EPO-TEK E4110 or EPO-TEK EC101.<sup>54</sup> The electrical contact between the tip and the electrode is also done using EPO-TEK E4110. Here, we show three different tips: an etched tungsten tip on the left, a splinter of silicon in the center, and a piece of iridium that was chipped off a 250  $\mu\text{m}$  wire using a wire cutter. Reproduced with permission from Giessibl *et al.*, *Nanotechnology* **15**, 84 (2004). Copyright 2004 IOP Publishing.

in a 21% error of the stiffness  $k$ . Sader *et al.*<sup>205</sup> proposed to express the stiffness in terms of mass density, volume, and eigenfrequency,

$$k = 0.243 \cdot \rho \cdot L \cdot w \cdot th \cdot (2\pi f_0)^2, \quad (65)$$

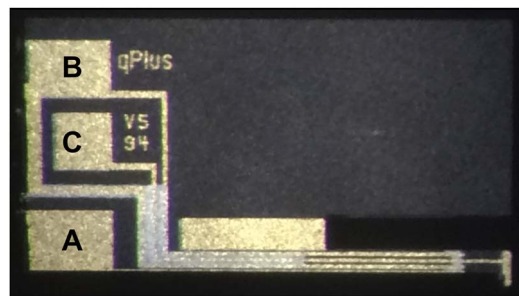


**FIG. 11.** Third generation of custom built qPlus sensors (Type M5B in Table I). This sensor has top and bottom electrodes A and side electrodes B for differential deflection measurement as well as a center electrode C to bias the tip for STM operation and (optional) to excite the sensor oscillation.

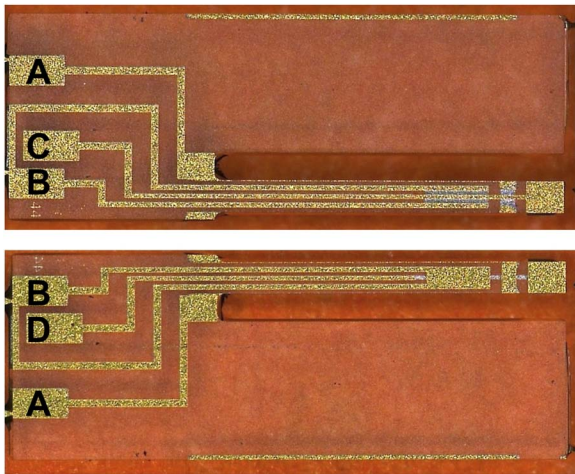


**FIG. 12.** Forth generation qPlus sensor with a total of four electrodes (Type S1.0B in Table I). Front side shown in the upper image: the top/bottom electrodes (A) and the side electrodes (B) serve for a differential deflection detection, the center electrode (C) on the front provides electrical contact to the tip. Back side shown in the lower image: top and bottom electrodes (A) and side electrodes (B) (connected to the ones on the front side) serve for deflection measurement; center and fourth electrode (D) is placed on the back side for excitation. In contrast to electrode (C), electrode (D) ends at about 2/3 of the length of the beam and does not connect to the tip section of the sensor.

where  $\rho$  is the mass density of the cantilever material. The eigenfrequency of the sensor can be measured with outstanding accuracy, and only three geometrical parameters in linear power remain (length  $L$ , width  $w$ , and thickness  $th$ ). If again each geometrical parameter is measured with an accuracy of 3%, the accuracy of the stiffness of the sensor is now precise

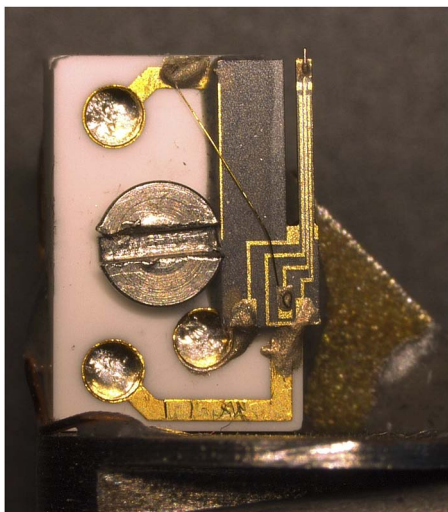


**FIG. 13.** Sensor for lateral force microscopy based on a third generation qPlus sensor (Type S1.0 in Table I) and a rectangular ceramic substrate.<sup>11</sup> The tip is aligned with the quartz beam, and the sensor is rotated by 90° to measure lateral forces.<sup>263</sup>

to 9%. Of course, the eigenfrequency needs to be measured before mounting the tip. Also, one could take the mass of the gold coating into account. Typically, the electrodes have a 500 nm thick gold coating on a much thinner adhesive layer of, e.g., chromium—as the density of gold is about 8 times larger than the density of quartz, the mass of the sensor beam might increase another percent or so.

Experimental measurements of  $k$  for the E158 type tuning forks listed in Table I show a stiffness of  $k = 1900$  N/m with respect to the end of the beam,<sup>162</sup> and finite element analysis came to a similar result.<sup>37</sup> However, given that we usually mount a tip with a wire diameter of  $d \approx 100$   $\mu\text{m}$  to the end of the quartz beam with length  $L$ , this stiffness has to be corrected by a factor  $L^3/(L + d/2)^3$  and a value of  $k = 1800$  N/m is a very good estimate.

### C. The probe tip of the sensor

Traditional silicon cantilevers are only about 0.2 mm long, and it is not feasible to attach a tip by hand. The large size of the qPlus sensor allows us to attach a variety of tips to them. Figure 10(c) already shows three examples where tungsten, silicon, and iridium tips are attached to the end of a qPlus sensor with conductive glue such that they can be used for STM and AFM simultaneously. The rigid properties of the qPlus sensor also allow us to mount single crystal tips from a cleavable material such as NiO and cleave the tips *in situ*<sup>268</sup> or clean by applying large voltage pulses.<sup>119</sup>

Metal tips can be characterized at the atomic level with a technique called COFI (Carbon Monoxide Front Atom Identification). In this method, the front end of the tip is probed by a CO molecule that is bonded, e.g., to a Cu(111) surface, where it stands upright and exposes the O atom to the tip. The CO molecule probes the tip structure and allows us to count the number of tip atoms (Ref. 257 and correction in Ref. 53) and even to determine, within limits, the chemical species of the tip's front atom.<sup>121</sup>

Gross *et al.*<sup>95</sup> found that the adsorption of a CO molecule on a metal tip increases the spatial resolution of AFM for organic molecules dramatically. The CO molecule adsorbs on the metal tip with the C atom bonded to the metal, exposing the O atom as the front atom of the tip. These tips provide atomic resolution of organic molecules, and they even image metallic clusters at unprecedented resolution.<sup>55</sup> Mohn *et al.*<sup>166</sup> discovered that other inert tip terminations such as Br, Cl, and Xe also lead to enhanced contrast. Subsequent studies<sup>16,164</sup> found that CuO tips offer a similar spatial resolution without the aberrations caused by lateral deflections of the CO molecule. Temirov *et al.*<sup>235</sup> found that STM with a trapped H<sub>2</sub> molecule in the junction provides a spatial resolution similar to AFM with CO terminated tips.

Regarding the length of tips, we recommend to keep them as short as possible as the longer they are, the more lateral motion is added to the normal oscillation.<sup>162,243</sup>

### D. Amplifier and wiring

For achieving low detector noise, the sensor needs to produce a large ac-current when oscillating at a given amplitude.



The amplifier needs to transform this ac-current into an ac-voltage with as little noise as possible. Thus, the combination of sensor and amplifier determines the detector noise. The sensor produces a certain charge per deflection, called calculated charge sensitivity  $S_q^{\text{theory}}$  that is measured in Coulombs per meter. When the sensor oscillates, this charge turns into an ac current, yielding a current sensitivity  $S_I^{\text{theory}} = 2\pi f \cdot S_q^{\text{theory}}$ . The amplifier transforms this current into a voltage, yielding a voltage sensitivity of  $S_v = R \cdot S_I^{\text{theory}} = R \cdot 2\pi f \cdot S_q^{\text{theory}}$ , where  $R$  is the gain of the amplifier.

In the first publication of the qPlus sensor in 1998, a high-gain instrumentation amplifier (Analog Devices<sup>9</sup> AD624 wired to a gain of 1000) was used.<sup>79</sup> Atomic resolution with the qPlus sensor was achieved by choosing a current-to-voltage converter<sup>81</sup> based on a 100 M $\Omega$  feedback SMD (surface mounted device) resistor and an AD744 operational amplifier chip.<sup>9</sup> Performance was further enhanced by using the AD823 operational amplifier chip<sup>9</sup> with a lower quiescent current. Today, we use a differential amplifier setup based on a schematic described in Refs. 133 and 144 with 10 G $\Omega$  SMD feedback resistors and an AD8616 operational amplifier chip,<sup>9</sup> and the complete setup and assembly are explained in Ref. 125 and Fig. 14.

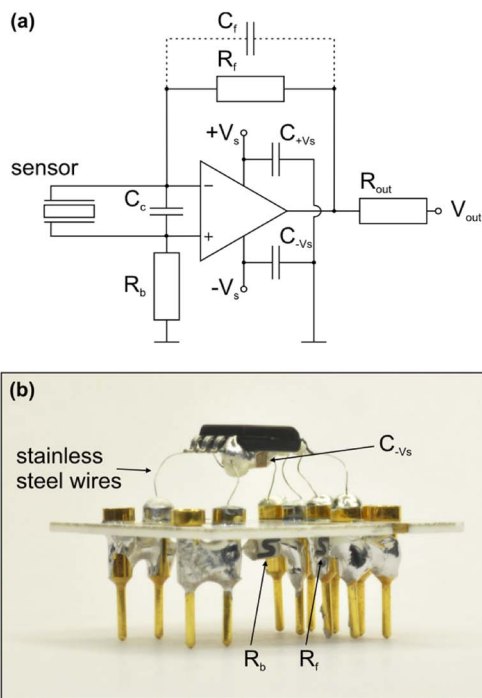


**FIG. 14.** Low noise and low power qPlus amplifier providing a differential deflection measurement. The amplifier is mounted directly onto a 4 K stage that minimizes the Johnson noise of the resistors, and the AD8616 operational amplifier is held by its stainless steel electrical wires to minimize thermal conduction. The length and width of the wires are chosen such that the internal heat dissipation of the amplifier leads to a temperature of the chip of about 80 K.<sup>125</sup> Reproduced with permission from F. Huber and F. J. Giessibl, *Rev. Sci. Instrum.* **88**, 073702 (2008). Copyright 2008 AIP Publishing LLC.

It is important to note that the distance between the sensor and the amplifier should be as small as practical. To be more precise, the capacity of the cable that connects the sensor and the amplifier should have a capacity as low as possible. The reason for this is that amplifiers have a certain input voltage noise and, when the input connects to a capacitive load, that voltage noise turns into a current noise, see Ref. 92. The capacity of a coaxial wire with length  $l$ , radius of inner wire  $r_i$ , and radius of outer shield  $r_a$  is given by

$$C = \frac{\pi \epsilon_0 \epsilon_r l}{\ln(r_a/r_i)}, \quad (66)$$

where  $\epsilon_0 = 8.85$  pF/m is the permittivity of vacuum and  $\epsilon_r$  is the relative dielectric constant of the insulation material used in the wire. In room temperature and 4 K instruments, the distance between the sensor and the amplifier is often only a few centimeters and the connection between the sensor and the amplifier can be done by two wires that are as thin as practical (possibly only 50  $\mu$ m) and spaced by a few centimeters, resulting in a capacity of only 1 pF or so. At ultralow temperatures, the distance between the amplifier and the sensor needs to be larger as outlined in the last chapter.

## E. Sensor excitation

The simplest excitation scheme uses the xyz-scan piezo such as a tube scanner with a modulated excitation signal added to the z-high voltage signal. Some tube scanners do not bring the four lateral electrodes all the way to the end but

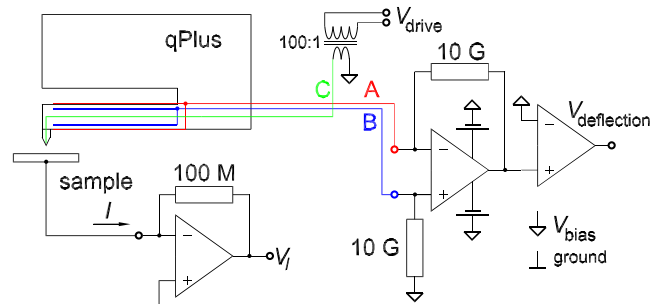


**FIG. 15.** Schematic for driving a qPlus sensor of generation 3 or 4. The tip is connected through a separate wire to the bias voltage. For generation 3 sensors, a transducer (typical gain 100/1–1000/1) adds a small excitation voltage to the bias. For a Q of 100 000, a drive voltage of 10  $\mu$ V (10 mV–100 mV before the transducer) is sufficient to result in an oscillation amplitude of 100 pm. For generation 4 sensors, the drive voltage connects directly to terminal D, and the sample bias connects to terminal C of the sensor. The deflection measurement is performed with a differential amplifier that is connected to deflection electrodes A and B (see Fig. 14). The drive voltage  $V_{\text{drive}}$  usually couples to the deflection electrodes through parasitic capacitive coupling, but as the deflection is measured differentially, an equal coupling of the drive voltage to electrodes A and B is easily achieved by appropriate routing of the wires. The positive and negative power supply voltages for the deflection amplifier are batteries that are referenced to the bias voltage  $V_{\text{bias}}$ . Thus, all three (or four) sensor electrodes are at a potential very close to  $V_{\text{bias}}$ , and the dc offset of the deflection amplifier of  $V_{\text{bias}}$  is subtracted by a differential amplifier at the output to result in a pure ac deflection output signal  $V_{\text{deflection}}$ . The tunneling current  $I$  is measured at the sample, in our case mainly with a 100 M $\Omega$  gain such that  $V_I = -100 \text{ M}\Omega \cdot I$ .



feature a small ring electrode at their end that is used for excitation. Other schemes use a separate dither piezo mounted onto the end of the xyz-scanner. The newest design of qPlus sensors integrates a separate excitation electrode on the quartz beam with a total of four electrodes, two for a differential excitation measurement, one for the STM current signal, and one for the excitation; see Fig. 12. A schematic that explains the wiring of an electrically excited qPlus sensor is displayed in Fig. 15.

#### IV. EXPERIMENTAL NOISE MEASUREMENTS OF QPLUS SENSORS

So far, we have only considered theoretical calculations to compare the noise characteristics of qPlus sensors and needle sensors (length extensional resonators or LER) studied here. Now, we supplement the calculations by measurements. Some of the following explanations and text are adopted from an earlier work that explicitly compares qPlus and needle sensors.<sup>92</sup>

##### A. Thermal noise peak

The measurement of the thermal noise peak is a comparatively simple and highly informative measurement. It shows how well sensor and amplifier perform and yields very important data such as the eigenfrequency  $f_0$  of the sensor, its quality factor  $Q$ , the experimental voltage sensitivity  $S_v^{\text{exp}}$ , and the deflection noise density  $n_q$ . First, we measure the thermal noise peak of the qPlus sensor with sensors of standard dimensions as shown in Fig. 16. The equipartition theorem states that each degree of freedom of an oscillator carries a thermal energy  $k_B T/2$ , where  $k_B$  is Boltzmann's constant and  $T$  is the temperature in Kelvin. For a one dimensional oscillator like the standard qPlus sensor, we find the thermal amplitude by equating the average potential energy to the thermal energy, yielding

$$\frac{1}{2} k A_{\text{rms}}^2 = \frac{1}{2} k_B T. \quad (67)$$

At room temperature, we find a thermal rms-amplitude of  $A_{\text{rms}} = 1.52$  pm or peak amplitude of  $A_0 p = 2.14$  pm for  $k = 1800$  N/m. In contrast to a qPlus sensor, a tuning fork has two coupled beams that oscillate in a common antiparallel mode such that  $2 \cdot k A_{\text{rms}}^2/2 = k_B T/2$ , yielding a thermal rms-amplitude of  $A_{\text{rms}} = 1.07$  pm or peak amplitude of  $A_0 p = 1.52$  pm. The needle sensor also is a coupled oscillator; therefore,  $2 \cdot k' A_{\text{rms}}^2/2 = k_B T/2$ , yielding a thermal rms-amplitude of  $A_{\text{rms}} = 62$  fm or peak amplitude of  $A_0 p = 88$  fm.

The power spectral density in Fig. 16 was recorded by connecting the output of the amplifier to the input of an FFT (Fast Fourier Transform) analyzer (Agilent 35670A Dynamical Analyzer). The input of the amplifier was connected to a standard qPlus sensor of type S1.0 (no tip attached). From Fig. 16, we can calculate the sensitivity as well as the deflection detector noise density by following the procedure published in Ref. 81.

The noise of the deflection measurement depends on the sensor, the cable, and the amplifier. A standard qPlus sensor oscillates at 30 kHz and generates a charge of  $1.44 \mu\text{C}/\text{m}$ . For the commercial Femto HQA-15M-10T charge amplifier,<sup>60,148</sup> we measured a noise density of  $n_{\text{amp}} = 122 \text{ zC}/\sqrt{\text{Hz}}$  when the input was connected to a 1 m coaxial cable with a capacitance of 100 pF and  $n_{\text{amp}} = 86 \text{ zC}/\sqrt{\text{Hz}}$  without cable. Thus, a standard qPlus sensor would yield  $n_q = 122 \text{ zC}/\sqrt{\text{Hz}}/1.44 \mu\text{C}/\text{m} = 85 \text{ fm}/\sqrt{\text{Hz}}$  when connected with a cable with a capacity of 100 pF and  $n_q = 62 \text{ fm}/\sqrt{\text{Hz}}$  when connected directly to the amplifier. For our homebuilt amplifier based on the operational amplifier AD823,<sup>9</sup> the noise at 4 K typically drops to 50%,<sup>110</sup> yielding  $n_q = 31 \text{ fm}/\sqrt{\text{Hz}}$  at 4 K. Our newest design<sup>125</sup> has reached optimal levels down to  $n_q = 16 \text{ fm}/\sqrt{\text{Hz}}$  and standard levels of  $n_q = 22 \text{ fm}/\sqrt{\text{Hz}}$  at 4 K. These homebuilt amplifiers are vacuum and UHV compatible and therefore can

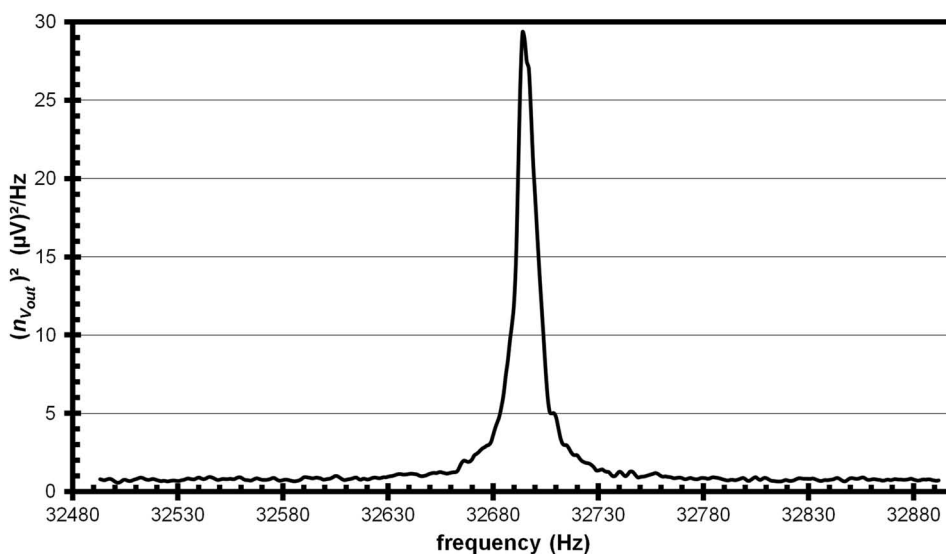


**FIG. 16.** Thermal spectrum of a qPlus sensor without a tip and standard dimensions at room temperature and ambient pressure. A homebuilt preamplifier was used. The eigenfrequency is  $f_0 = 32\,698$  Hz, the  $Q$ -factor is 2900, the charge sensitivity of the sensor is  $S_q^{\text{exp}} = 1.44 \mu\text{C}/\text{m}$ , the voltage sensitivity is  $16 \text{ mV}/\text{nm}$ , and the deflection detector noise density is  $62 \text{ fm}/\sqrt{\text{Hz}}$ .<sup>92</sup> Reprinted with permission from Giessibl *et al.*, Phys. Rev. B **84**, 125409 (2011). Copyright 2011 The American Physical Society.

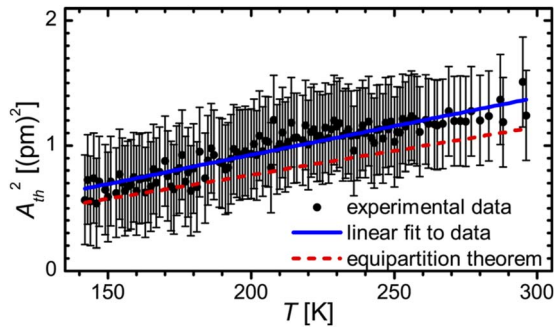


**FIG. 17.** Integrated thermal spectrum of a quartz tuning fork E158 with standard dimensions as a function of temperature.<sup>255</sup> Reproduced with permission from Welker *et al.*, *Appl. Phys. Lett.* **99**, 084102 (2011). Copyright 2011 AIP Publishing LLC.

be connected closely to the sensor, thereby greatly reducing  $C_{\text{cable}}$ .

The power spectral density in Fig. 16 was recorded by connecting the output of a home-built UHV compatible amplifier to the input of the Nanonis OC4 PLL and recording its FFT (Fast Fourier Transform) output. The input of the amplifier was connected to a qPlus sensor without a tip with standard dimensions using a short cable with a length of approximately 0.1 m (capacity approximately 10 pF). The experimental result is  $S_{\text{qPlus}}^{\text{exp}} = 1.44 \mu\text{C}/\text{m}$ —about 51% of the theoretical value. The deviation between the theoretical and experimental values is probably due to edge effects—the calculation of the sensitivity is based on a homogeneous field distribution and an electrode configuration in the quartz crystal, while the actual field distribution is perturbed by edge effects [see Fig. 8(h)].

The validity of the equipartition theorem is verified by measuring the thermal spectrum as a function of temperature, as displayed in Fig. 17.<sup>255</sup> While the measurement of the thermal noise peak is simple, it needs to be used with care at low temperatures. As the thermal excitation becomes smaller with temperature, other excitation sources such as mechanical vibrations can rise above the thermal excitation, and it is advisable to use a different method for amplitude calibration at low temperatures.

## B. Comparison of the four theoretical noise sources to experimental qPlus results

### 1. Thermal noise

Thermal noise depends on three sensor properties: eigenfrequency  $f_0$ , stiffness  $k$ , and quality factor  $Q$ . In summary, thermal noise is small for cantilevers that are as soft as possible while stiff enough to prevent jump-to-contact at small amplitudes and that have a high eigenfrequency and a high quality factor,

$$\delta k_{\text{ts thermal}} \propto \sqrt{\frac{kB}{f_0 Q}}. \quad (68)$$

For the qPlus sensor,  $Q \approx 3000$  at room temperature, reaching up to 200 000 at 4 K<sup>120</sup> with type qPlus S1.0 or even more than one million<sup>190</sup> with type qPlus M4 (see Table I for type specifications). Thus, at room temperature, the thermal contribution to the minimal detectable force gradient is  $\delta k_{\text{ts thermal}}/\sqrt{B} = 6$  (mN/m)/ $\sqrt{\text{Hz}}$  for the needle sensor and  $\delta k_{\text{ts thermal}}/\sqrt{B} = 3$  (mN/m)/ $\sqrt{\text{Hz}}$  for the qPlus sensor. At  $T = 4$  K, the minimal detectable force gradient is  $\delta k_{\text{ts thermal}}/\sqrt{B} = 390$  ( $\mu\text{N}/\text{m}$ )/ $\sqrt{\text{Hz}}$  for the needle sensor and  $\delta k_{\text{ts thermal}}/\sqrt{B} = 40$  ( $\mu\text{N}/\text{m}$ )/ $\sqrt{\text{Hz}}$  for the qPlus sensor. Again, these calculations refer to  $A = 100$  pm.

### 2. Detector noise

In summary, we find that using a very large spring constant for sensors with piezoelectric detection is not a significant disadvantage regarding deflection detector noise because although the frequency shift that a sensor is subject to is proportional to  $1/k$ , the sensitivity is proportional to  $k$ , and the two effects cancel.

For quartz sensors, the deflection noise depends on the charge that is generated per deflection and the gain and noise of the preamplifier. Current-to-voltage converters convert the current provided by the quartz sensor to a voltage. However, the frequency response of the current-to-voltage converter is not independent of frequency but is given by

$$V_{\text{out}} = -\frac{R}{1 + i2\pi fRC} I, \quad (69)$$

where  $R$  is the resistance of the feedback resistor and  $C$  is its parasitic capacitance. The lower line in Fig. 19 shows the theoretical frequency response of an ideal operational amplifier with  $R = 100$  M $\Omega$  and a parasitic capacitance of  $C = 0.2$  pF. The gain is flat for frequencies smaller than the corner frequency  $f_{c1} = 1/(2\pi RC) = 7.96$  kHz. For  $f \gg f_{c1}$ , the gain is given by  $V_{\text{out}} \approx -I/(i2\pi fC)$ —inversely proportional to  $f$ . A sinusoidally varying charge  $Q_{\text{ch}} = Q_0 \exp(i2\pi ft)$  corresponds to a current  $I = \dot{Q}_{\text{ch}} = Q_0 i2\pi f \exp(i2\pi ft)$ ; thus, the gain can be expressed as  $V_{\text{out}} = -Q_{\text{ch}}/C$ . Therefore, this amplifier is called a “charge amplifier” for frequencies significantly larger than  $f_{c1}$ . Simple amplifiers as the one shown in Fig. 18 often display a second corner frequency  $f_{c2}$  not very much higher than  $f_{c1}$  and for frequencies beyond  $f_{c2}$  the gain decays proportional to  $1/f^2$ . A popular commercial amplifier<sup>60</sup> that is used here for the needle sensor has an  $f_{c2}$  at around 15 MHz and is therefore suited well for high-frequency sensors.

The question is now when is it advisable to use a current-to-voltage converter and when is it favorable to use a charge amplifier. Figure 19 shows that the current-to-voltage converter operates similar to a charge amplifier for sufficiently large frequencies, i.e., it does not provide a linear relationship between current and output voltage independent of frequency, but its gain rolls off as  $1/f$  with increasing frequency  $f$ . While one can increase  $f_{c1}$  by reducing the value of the feedback resistor  $R$ , a reduction in  $R$  increases the current noise. The tradeoff between noise and bandwidth leads to an optimal amplifier type for a given operating frequency. Indeed, we found out that our home-built current-to-voltage converter has a better signal-to-noise ratio for frequencies between

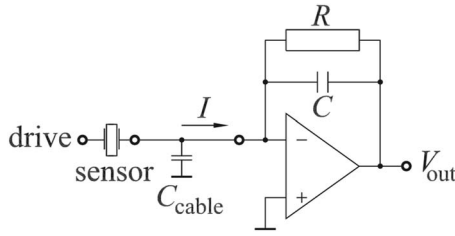


**FIG. 18.** Schematic of a quartz sensor, cable, and current-to-voltage converter that is often used for amplifying deflection data from quartz sensors.<sup>92</sup> The gain of the amplifier is given by  $V_{out} = -RI/(1 + i/f f_{c1})$  with its first corner frequency  $f_{c1}$  given by  $f_{c1} = 1/(2\pi RC)$ , where  $V_{out}$  is given by a complex number to indicate the phase shift. Typically, amplifiers of qPlus sensors are operated far beyond  $f_{c1}$ , i.e.,  $f/f_{c1} \gg 1$ , so they essentially act as charge amplifiers. The capacity of the cable should be as low as possible—cable capacity increases noise in the amplifier output. If the amplifier is vacuum compatible, it can be placed close to the sensor, thus reducing cable capacity and noise. The sensor can be excited electrically as shown in this figure or mechanically—the drive signal is grounded in this case. Reprinted with permission from Giessibl *et al.*, Phys. Rev. B **84**, 125409 (2011). Copyright 2011 The American Physical Society.

60 kHz and 100 kHz, while the FEMTO amplifier<sup>60</sup> works better for higher frequencies.<sup>38</sup> For charge amplifiers, the deflection detector noise density can be expressed by

$$n_q = \frac{n_{amp}}{S_q}, \quad (70)$$

where  $n_{amp}$  is the noise density of the preamplifier and  $S_q$  is the charge sensitivity (charge per deflection) as calculated for the needle sensor in Eq. (64) and for the qPlus sensor in Eq. (55). With the calculations in the previous chapter, we find

$$\delta k_{ts \text{ sensor}} = \sqrt{\frac{8}{3}} \frac{k}{S_q f_0} n_{amp} \frac{B^{3/2}}{A}. \quad (71)$$

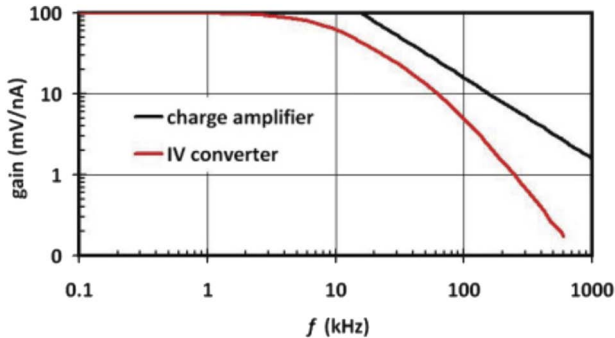


**FIG. 19.** Current gain versus frequency for a current-to-voltage converter built from an ideal operational amplifier and a 100 MΩ feedback resistor with a parasitic capacitance of 0.2 pF (solid line), yielding a first corner frequency (here,  $f_{c1} = 8$  kHz). For frequencies higher than  $f_{c1}$ , the gain drops proportional to  $1/f$ . Typically, these simple amplifiers develop a second corner frequency (here  $f_{c2} = 80$  kHz);<sup>38</sup> for frequencies higher than  $f_{c2}$ , their gain drops proportional to  $1/f^2$ . The dashed line displays the gain of a commercial charge amplifier<sup>50</sup> with a constant gain of  $10^{13}$  V/C (dashed line) for a remarkably large frequency range from 250 Hz to 15 MHz.<sup>92</sup> Reprinted with permission from Giessibl *et al.*, Phys. Rev. B **84**, 125409 (2011). Copyright 2011 The American Physical Society.

This equation shows that the deflection detector noise is small for small spring constants, small amplifier noise, large sensitivity, and large eigenfrequency. Thus, the figure of merit for the sensor is not how much charge per deflection it generates (expressed by  $S_q$ ) but the charge per force given by  $S_q/k$  when a charge amplifier is used. If a current amplifier with sufficient bandwidth is available, the figure of merit is the current that the sensor generates per force, expressed as  $S_q f_0/k$ .

We can also express this in noise density,

$$n_{kts \text{ sensor}} = \sqrt{8} \frac{k}{S_q f_0} n_{amp} \frac{f_{mod}}{A}. \quad (72)$$

For both needle and qPlus sensors, the sensitivity is proportional to  $k$ . We find for the needle sensor that

$$\delta k_{ts \text{ needle sensor}} = \sqrt{\frac{8}{3}} \frac{n_{amp} t B^{3/2}}{d_{21} L A f_0} \quad (73)$$

for the ideal case of  $L_e = L$ . For the qPlus sensor, we find

$$\delta k_{ts \text{ qPlus sensor}} = \sqrt{\frac{8}{3}} \frac{n_{amp} t^2 B^{3/2}}{6 d_{21} L^2 A f_0}, \quad (74)$$

again assuming the ideal case of  $L_e = L$ . Thus, deflection detector noise depends on the properties of the sensor and the amplifier. If we assume a charge noise density of  $n_{amp} = 90$  zC/ $\sqrt{\text{Hz}}$  (such as achieved by the commercial FEMTO amplifier<sup>60</sup> when loaded with a 1 m coaxial cable corresponding to a 100 pF cable capacitance), we can now calculate an explicit number for the deflection detector noise contribution to the force gradient noise with  $A = 100$  pm and the geometrical values after Table I. For the needle sensor, we find a theoretical deflection detector noise contribution of

$$\delta k_{ts \text{ needle sensor}} = 33.2 \mu\text{N/m} \frac{B^{3/2}}{\text{Hz}^{3/2}}, \quad (75)$$

and for the qPlus sensor, we find a theoretical deflection detector noise contribution of

$$\delta k_{ts \text{ qPlus sensor}} = 25.7 \mu\text{N/m} \frac{B^{3/2}}{\text{Hz}^{3/2}}. \quad (76)$$

For a bandwidth of 100 Hz, the theoretical deflection detector noise contribution is thus 33.2 mN/m for the needle sensor and 25.7 mN/m for the qPlus sensor. However, we have based this calculation on the theoretical sensitivity of the sensors, and we found out experimentally that while the sensitivity of the needle sensor matches theory, the qPlus sensor develops only about 50% of the theoretical sensitivity. As deflection detector noise depends dramatically on bandwidth, it can be reduced substantially by bandwidth reduction. At low temperatures, where slow scanning is possible, the bandwidth can be reduced to 1 Hz or less and tiny force gradients can be detected in this case. For a bandwidth of 1 Hz, the deflection detector noise contribution is thus 33.2  $\mu\text{N/m}$  for the needle sensor and 25.7  $\mu\text{N/m}$  for the qPlus sensor. However, at very low bandwidth, the remaining three noise sources are typically much larger than the deflection noise.

### 3. Oscillator noise for quartz sensors

As oscillator noise is white, it is hard to distinguish it from thermal noise. For the Q values from above, we find room temperature values of  $\delta k_{ts \text{ osc}} = 4.6 \text{ (mN/m)/}\sqrt{\text{Hz}}$  for the needle sensor and  $\delta k_{ts \text{ thermal}} = 0.6 \text{ (mN/m)/}\sqrt{\text{Hz}}$  for the qPlus sensor. At  $T = 4 \text{ K}$ , the contribution of oscillator noise to the minimal detectable force gradient is  $\delta k_{ts \text{ osc}} = 1.4 \text{ (mN/m)/}\sqrt{\text{Hz}}$  for the needle sensor and  $\delta k_{ts \text{ thermal}} = 9.5 \text{ (}\mu\text{N/m)/}\sqrt{\text{Hz}}$  for the qPlus sensor. Again, these calculations refer to  $A = 100 \text{ pm}$ .

### 4. Frequency drift noise for quartz sensors

Temperature variations cause a drift in eigenfrequency. For silicon cantilevers, the relative frequency variation is linear with temperature with a value of  $-35 \text{ ppm/K}$  at room temperature.<sup>100</sup> Thus, a hypothetical Si cantilever with  $k = 1 \text{ kN/m}$  (this large stiffness would be required to enable stable oscillation at small amplitudes) would be subject to a  $\langle k_{ts} \rangle$  drift of  $-35 \text{ mN/m/K}$ .

Quartz sensors show a quadratic frequency shift with temperature, and the eigenfrequency varies with temperature as an inverted parabola centered around the turnover temperature  $T_p$ .<sup>163</sup>

$$\frac{\delta f_{\text{sensor}}}{f_0} = -\chi(T - T_p)^2. \quad (77)$$

The turnover frequency depends on the crystal cut (see Fig. 9 in Ref. 170). Tuning fork crystals are often cut to yield a turnover temperature  $T_p = 298 \text{ K}$ , as this is close to the temperature of a watch in thermal equilibrium with a wrist. Length-extensional-resonators, by contrast, are often oriented such that their turnover temperature is around  $313 \text{ K}$ ,<sup>163</sup> probably because  $1 \text{ MHz}$  crystals are typically not worn on the wrist but built into printed circuit boards that have higher operating temperatures than the human body. This thermal frequency drift causes a thermal drift in force gradient measurement given by

$$\delta k_{ts \text{ drift}} = -2k\chi(T - T_p)^2. \quad (78)$$

Although the temperature stability of quartz is excellent with very small values of  $\chi = 35 \cdot 10^{-9} \text{ K}^{-2}$ ,<sup>163</sup> the net effect on the precision on the measurement of  $\langle k_{ts} \rangle$  is proportional to the effective stiffness of the sensor  $k$ , and drift noise can be a challenge for very stiff sensors such as the needle sensor.

The quadratic dependence of the frequency variation with temperature is only valid for temperatures around  $T_p$ . For the temperature range from  $300 \text{ K}$  to  $4 \text{ K}$ , the frequency variation has been measured by Hembacher *et al.*<sup>110</sup> and fits well to a semi-empirical relation given by

$$\frac{\delta f_{\text{sensor}}}{f_0} \approx -0.00081[1 + \cos(\pi T/T_p)] \quad (79)$$

with a total relative frequency change of  $-1620 \text{ ppm}$  over the temperature range from  $300 \text{ K}$  to  $4 \text{ K}$  (see Fig. 20). An *et al.* have found a similar frequency change in a needle sensor (Fig. 3 in Ref. 7) from  $998\,066 \text{ Hz}$  at  $300 \text{ K}$  to  $996\,314 \text{ Hz}$ , corresponding to  $-1755 \text{ ppm}$ . This equation shows that frequency drift with temperature is particularly large for temperatures

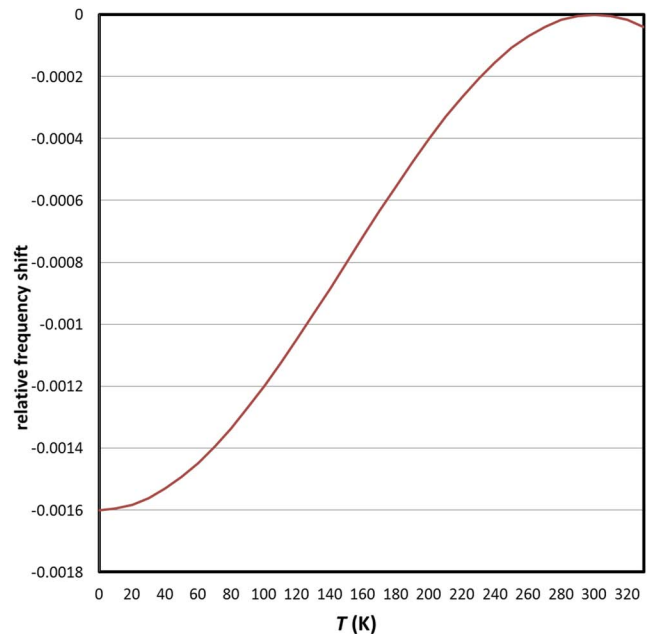


**FIG. 20.** Approximate relative frequency change  $(f(T) - f(300 \text{ K}))/f(300 \text{ K})$  of a quartz tuning fork and a qPlus sensor as a function of temperature from  $T = 0$  to  $330 \text{ K}$ . For temperatures below  $40 \text{ K}$ , an anomaly is observed (see Fig. 21). Although the relative frequency shift is much smaller for quartz sensors than for silicon cantilevers, the effect on the measured force gradient scales with stiffness  $k$ .

between room temperature and absolute zero. However, while this approximate formula models the data measured by Hembacher *et al.*<sup>110</sup> quite precisely down to liquid helium temperatures, a detailed measurement of the eigenfrequency of several types of quartz sensors has shown that the frequency shows a minimum around  $23 \text{ K}$  and an increase as the temperature decreases to  $4 \text{ K}$  at a rate of approximately  $-7.5 \text{ ppm/K}$  at  $4 \text{ K}$ . Figure 21 shows the dependence of the

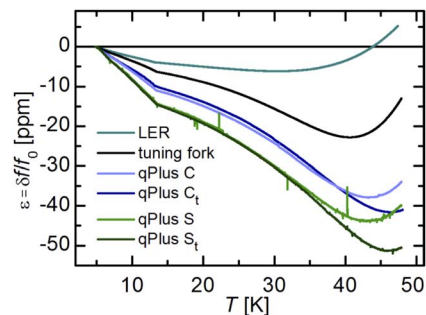


**FIG. 21.** Measured relative frequency change  $(f(T) - f(3 \text{ K}))/f(3 \text{ K})$  of quartz length extensional resonators (LER), tuning forks, and qPlus sensors in the temperature range between  $3$  and  $50 \text{ K}$ .<sup>191</sup> The minimal frequency does not occur at absolute zero but approximately at  $46 \text{ K}$ . At a temperature of  $4 \text{ K}$ , the relative frequency drift is  $-7.5 \text{ ppm/K}$ . An anomaly is observed around  $12 \text{ K}$ . Reprinted with permission from Pielmeier *et al.*, Beilstein J. Nanotechnol. **5**, 407–412 (2014). Copyright 2014 Author(s), licensed under a Creative Commons Attribution 2.0 License.<sup>36</sup>



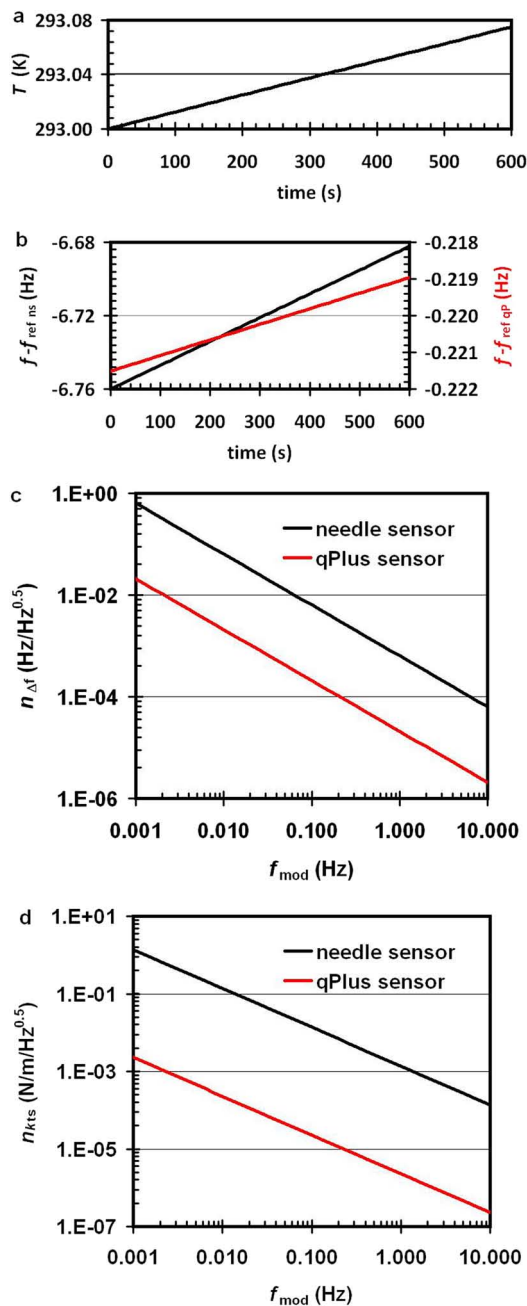


**FIG. 22.** Effect of temperature drift on frequency drift, frequency noise at the PLL output, and force gradient noise. (a) A temperature drift of  $125 \mu\text{K/s}$  is assumed, yielding a temperature increase of  $75 \text{ mK}$  over  $10 \text{ min}$ . (b) Frequency drift at a temperature of  $10 \text{ K}$  above or below the turnover temperature  $T_p$ ; see Eq. (77). For the needle sensor, the absolute frequency change over  $10 \text{ min}$  is  $78 \text{ mHz}$ , while for the qPlus sensor, it is  $2.5 \text{ mHz}$ . (c) Power spectral density of the frequency drift noise for needle and qPlus sensors. A linear frequency drift with time causes a  $1/f$  power spectrum. (d) Power spectral density of the tip-sample force gradient noise due to drift. This noise contribution is linear with the force constant of the sensor, i.e., it is 600 times larger for the needle sensor than for the qPlus sensor. Reprinted with permission from Giessibl *et al.*, Phys. Rev. B **84**, 125409 (2011). Copyright 2011 The American Physical Society.

relative frequency shift for low temperatures. Because the relative frequency shift is mainly dependent on the variation of the velocity of sound with temperature (p. 38 in Ref. 167), we expect a similar relative frequency shift for the qPlus sensor and the needle sensor also in the temperature range from  $4 \text{ K}$  to  $30 \text{ K}$ .

We now analyze the effect of temperature drift on the measured tip-sample force gradient. First, we look at the frequency drift of the sensor for a given rate of temperature change. Figure 22(a) shows temperature versus time for a constant drift rate of  $dT/dt = 125 \mu\text{K/s}$  at  $T - T_p = 10 \text{ K}$  over a time interval of  $10 \text{ minutes}$ . The frequencies of quartz sensors vary according to Eq. (77) by a rate  $r_{ns} = 100 \mu\text{Hz/s}$  for the needle sensor and  $r_{qp} = 3.3 \mu\text{Hz/s}$  for the qPlus sensor.

Because the frequency drift rate is proportional to  $f_0$ , the force gradient noise due to thermal drift is proportional to the stiffness of the sensor  $k$ , and thus this noise source is 600 times larger for the needle sensor than for the qPlus sensor.

To obtain the variation in the measured tip-sample force gradient  $\langle k_{ts} \rangle$ , the relative frequency shift has to be multiplied by  $2k$ . For the qPlus sensor, we obtain a  $\langle k_{ts} \rangle$  drift of  $-27 (\mu\text{N/m})/\text{mK}$ , and for the needle sensor, we get  $-16 (\text{mN/m})/\text{mK}$ . Because variations in ambient pressure cause a slight change in boiling temperature of the helium bath, we expect that temperature drift can become a significant issue for the needle sensor even at low temperatures.

We can estimate the influence of temperature changes at  $4.2 \text{ K}$  by noting that a change in ambient pressure of  $1 \text{ hPa}$  results in a change in boiling temperature of helium of about  $1 \text{ mK}$ . The change in sensor frequency is then about  $7.5 \text{ ppb}$ , i.e., a frequency change of  $-0.25 \text{ mHz}$ . This is still small compared to the expected frequency stability of the PLL detector.

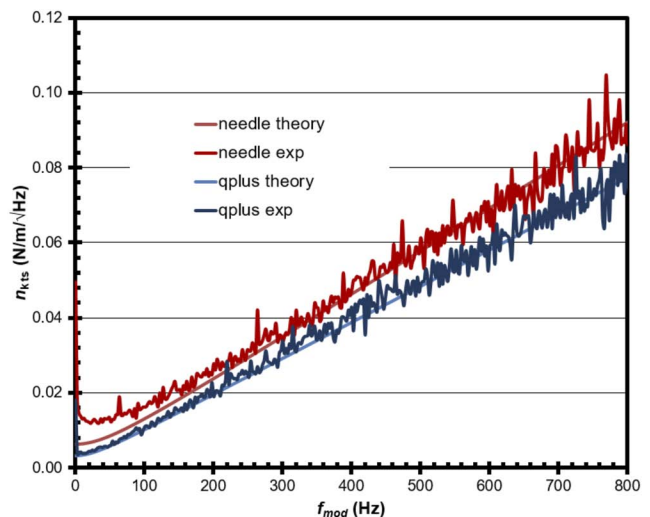


**FIG. 23.** Total experimental (jagged lines) and calculated (smooth lines) force-gradient-noise densities as a function of modulation frequency for a qPlus sensor and a needle sensor at room temperature. The calculated force-gradient-noise-densities are derived with the experimental values for  $S$ ,  $k$ ,  $n_{amp}$ ,  $Q$ , and  $f_0$  at an amplitude of  $A = 100 \text{ pm}$ .

**TABLE II.** Noise contributions of the four noise sources for the qPlus sensor and needle sensor in ambient conditions, vacuum at ambient temperature, and vacuum at 4 K. The row indicated by qPlus 4 K UHV\* indicates ideal conditions with the most recent amplifier and a sensor with a very high Q. For both sensors, the  $\delta k_{ts \text{ drift}}$  data are based on Fig. 21.

Sensor	$n_q$ (fm/ $\sqrt{\text{Hz}}$ )	Q	$\delta k_{ts \text{ det}}/B^{3/2}$ ( $\frac{\mu\text{N}}{\text{m}}/\text{Hz}^{3/2}$ )	$\delta k_{ts \text{ th}}/B^{1/2}$ ( $\frac{\mu\text{N}}{\text{m}}/\text{Hz}^{1/2}$ )	$\delta k_{ts \text{ osc}}/B^{1/2}$ ( $\frac{\mu\text{N}}{\text{m}}/\text{Hz}^{1/2}$ )	$\delta k_{ts \text{ drift}} (\frac{\text{mN}}{\text{m}})$ at $\Delta T = 0.1 \text{ K}$
qPlus 300 K air	62	2 900	105	3300	544	0.00126
qPlus 300 K UHV	62	15 000	105	1450	105	0.00126
qPlus 4 K UHV	31	200 000	52.6	398	4	−2.7
qPlus 4 K UHV*	16	1500 000	27.1	145	0.275	−2.7
Needle 300 K air	1.89	18 500	57.7	5550	1560	0.756
Needle 300 K UHV	1.89	27 000	57.7	4590	1070	0.756
Needle 4 K UHV	1.89	50 000	57.7	3370	577	−1620

Even oven-controlled quartz oscillator as used in Nanonis control systems<sup>173</sup> have typical frequency errors on the order of 20 ppb. Generally, frequency drift noise is low, even more so at low temperatures. Frequency drift noise can be minimized by using a PLL with an oven controlled quartz time base and by allowing it enough time to settle between powering on of the PLL and starting the measurement.

### C. Comparison between experimental and theoretical noise data

Figure 23 shows the calculated (smooth lines) and experimental (jagged lines) power spectral density of the force gradient noise  $n_{kts}$  as a function of modulation frequency  $f_{mod}$ . This graph is produced by inserting the output of the phase-locked-loop detector to a FFT analyzer (Agilent) and multiplying the frequency shift by the corresponding scaling factor ( $k_{ts} = 2k/f_0 \cdot \Delta f$ , thus  $n_{kts} = 2k/f_0 \cdot n_{\Delta f}$ ). The total noise of the force gradient measurement is given by

$$\delta k_{ts} = \sqrt{\int_0^B n_{kts}^2(f_{mod}) df_{mod}}. \quad (80)$$

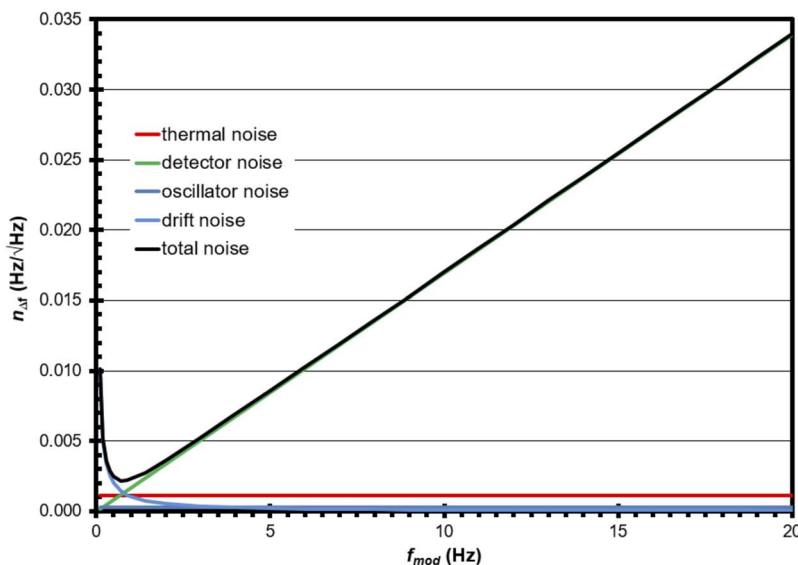


**FIG. 24.** Spectral density of theoretical output of PLL. Parameters:  $f_0 = 60 \text{ kHz}$ ,  $k = 1800 \text{ N/m}$ ,  $A = 50 \text{ pm}$ ,  $n_q = 60 \text{ fm}/\sqrt{\text{Hz}}$ ,  $T = 4 \text{ K}$ ,  $Q = 100\,000$ , drift rate  $r = 10^{-4} \text{ Hz/s}$ , measuring time  $\tau = 1000 \text{ s}$ .

The calculated graphs include deflection detector noise (linear with  $f_{mod}$ ), thermal noise (constant with  $f_{mod}$ ), and oscillator noise (also constant with  $f_{mod}$ ). Frequency drift noise, which is large for long measuring times (i.e., small  $f_{mod}$ ), is not included in the calculation but clearly apparent in the measurement by the increase of the experimental needle deflection detector noise density for small  $f_{mod}$ . The increase in noise for small  $f_{mod}$  in the needle sensor data is related to the strong influence of thermal frequency drift. A random walk in temperature would lead to a random walk in frequency, and the Fourier transform of a random walk function leads to a  $1/f$  power distribution.<sup>245</sup>

Table II lists the individual noise contributions and typical parameters for qPlus sensors and needle sensors at ambient conditions, UHV, and low temperatures.

Figure 24 displays the four noise sources and their contributions to the frequency spectrum of the PLL output for typical qPlus sensors at liquid helium temperature. Thermal noise and oscillator noise are constant with respect to frequency. Due to the high Q value, oscillator noise is negligible here—even smaller than thermal noise. However, although

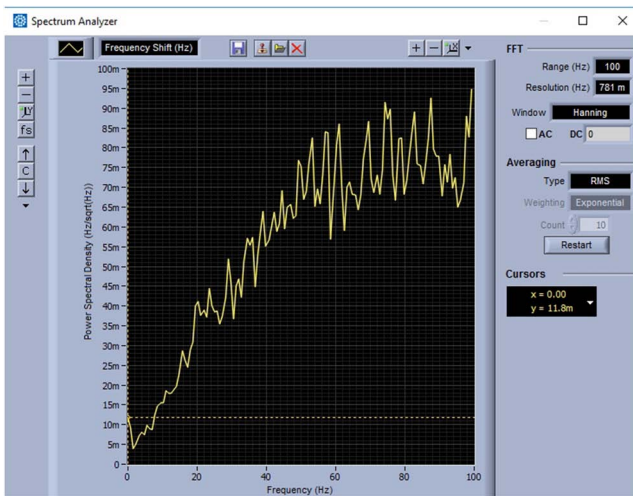


**FIG. 25.** Experimental frequency spectrum of the PLL output. Parameters:  $f_0 = 46\,602.6$  Hz,  $k = 1800$  N/m,  $Q = 384\,300$ ,  $A = 50$  pm, PLL phase bandwidth 50 Hz. Equation (20) connects the slope of the experimental  $n_{\Delta f}$  curve above to  $n_q$ , yielding  $n_q \approx 50$  fm/ $\sqrt{\text{Hz}}$ . Note that the linear increase in noise with frequency rolls off at the bandwidth setting of the PLL detector.

thermal noise is proportional to  $(T/Q)^{0.5}$ , thermal noise (red) is noticeable at a density of about 1 mHz/ $\sqrt{\text{Hz}}$ . Drift noise is apparent at very low frequencies—the noise density reaches a minimum at about 0.75 Hz, showing that noise could be decreased until the time per pixel reaches 1/0.75 s corresponding to an acquisition time of more than 1 h for a  $64 \times 64$  pixel image. For even lower scanning speeds, noise would go up again. Detector noise is clearly dominant and, in theory,

increases linearly forever with higher modulation frequencies. In practice, the finite bandwidth of the PLL detector sets an end to that increase. Figure 25 shows an experimental noise spectrum (see the figure caption for sensor parameters). The linear increase in noise starts to roll off at about a frequency of 50 Hz, corresponding to the bandwidth setting of the PLL detector that provides a low pass filter of at least second order that turns the linear increase of noise with  $f_{\text{mod}}$  to a decaying noise for frequencies above the bandwidth setpoint.

#### D. Identification of sensor noise in an experimental FM-AFM image

The four noise sources that have been identified above can be seen directly when performing a Fourier transformation of the frequency shift signal. Thus, one either needs a FFT Analyzer or a control software that allows us to display the frequency shift signal in frequency space. Interestingly, one can also partially distinguish the noise sources in postprocessing of the images. When looking at a constant-height image of a flat and periodic surface such as shown in Fig. 26(a), we use imaging processing software such as WSXM<sup>122</sup> to create a FFT (Fast Fourier Transform) image in (b). Figure 26(b) essentially shows six peaks that correspond to the reciprocal unit cell vectors of the  $\text{CaF}_2$  lattice imaged in (a). Figure (c) shows a Gaussian filtered image, using a  $10 \times 10$  Gauss filter. The original image had an average frequency shift of  $-6.5$  Hz with a corrugation of  $\pm 2.1$  Hz, and the corrugation is reduced to  $\pm 1.25$  Hz due to Gauss filtering. Figure 26(d) shows the same sample area but imaged at a distance increment of 250 pm. The contrast is mainly due to electrostatic interactions, and the fields decay with distance  $z$  as  $\exp(-z/53.2 \text{ pm})$ . Therefore, the contrast between Figs. 26(a) and 26(d) should decay to less than one percent ( $\exp(-250 \text{ pm}/53.2 \text{ pm}) = 0.0091$ ). Indeed,

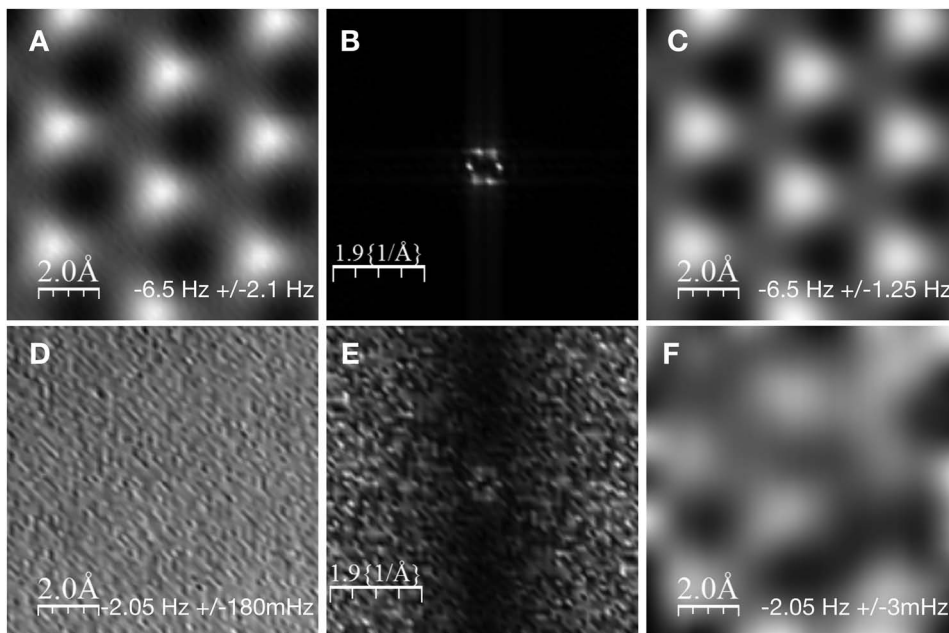


**FIG. 26.** Experimental images of  $\text{CaF}_2(111)$  recorded with a qPlus sensor terminated with a CO tip. Top row [(a)–(c)]: data taken at an approximate closest distance between the cores of the O tip atom and the  $\text{F}_{\text{top}}^-$  ion of 350 pm.<sup>157</sup> Bottom row [(d)–(f)]: data taken at a distance of about 600 pm [250 pm further away than (a)–(c)]. Left column: raw data. Center column: fast Fourier transformed (FFT) image. Right column: Gaussian low pass filtered images of (a) and (d), width of Gaussian 10 pixels. Image size is 1 nm,  $64 \times 64$  pixels, recorded at  $T = 4.4$  K, acquisition time 660 s/image. Sensor properties (type M4, see Table I):  $k = 1800$  N/m,  $f_0 = 55\,051.4$  Hz,  $Q = 811\,500$ ,  $A = 50$  pm. Data recorded by Liebig, see Ref. 157.

we see only noise in Fig. 26(d) because the expected 20 mHz corrugation is masked by noise. The FFT image in Fig. 26(e) shows that this noise is mainly due to detector noise, as the detector noise density increases linearly with frequency [see Eq. (72)]. The V-shaped FFT spectrum shows that detector noise strongly dominates overall noise. As detector noise rises sharply with frequency, it can be curtailed by bandwidth reduction. The region around the center of the FFT spectrum in Fig. 26(b) still shows the six data peaks that also appear in Fig. 26(b), although they are more than a factor of 100 higher in (b). In principle, the V-shaped detector noise floor is also present in B. Low-pass filtering in the time domain can be performed after the data have been taken by low pass filtering in the spatial frequency domain as when using a Gaussian filter. Figure 26(f) is a double low pass filtered version of Fig. 26(d)—it clearly shows the atomic structure similar to Fig. 26(c), yet at only about 1% of contrast as it is recorded 250 pm further away (actually, the contrast is even smaller due to applying a Gauss filter).

## V. APPLICATIONS

The qPlus sensor has many applications, and today, hundreds of microscopes are in use that utilize this sensor. Therefore, this section provides some of the typical applications that have emerged so far in our group as well as other groups from various parts of the world. As this article is mainly concerned with instrumentation, the applications are structured by environment: ambient, ultrahigh vacuum (UHV), low temperature UHV, and ultralow temperature UHV. Incidentally, this is also more or less in line with the historic development.

### A. Ambient and liquid environments

#### 1. First results in ambient conditions

The first images using the qPlus sensor were obtained in ambient conditions on a test grating and a CD in intermittent contact mode (see Fig. 27). The forces that were used in these early images were relatively large—at least 30 nN repulsion or more, but the scanning speed was relatively fast, up to 100  $\mu\text{m/s}$ . The oscillation amplitudes in these early experiments were very large—250 nm and needed for stability due to several reasons that will be discussed below (poor amplifier, analog amplitude control with little dynamic range). After these experiments, we moved to vacuum (Subsection V B 1) and obtained atomic resolution within about a year. We revisited the challenge of obtaining atomic resolution in ambient conditions using the qPlus sensor after a detailed understanding about the imaging contrast was obtained in controlled vacuum conditions.<sup>267</sup>

#### 2. Atomic resolution of KBr, calcite, and graphene

In ambient conditions, surfaces are continuously changing because of adsorption and desorption and they are usually covered with a film of adsorbates. This was the main reason, why it took a few years after great success in vacuum to obtain atomic resolution. Nevertheless, true atomic resolution in ambient conditions, where samples are usually covered by

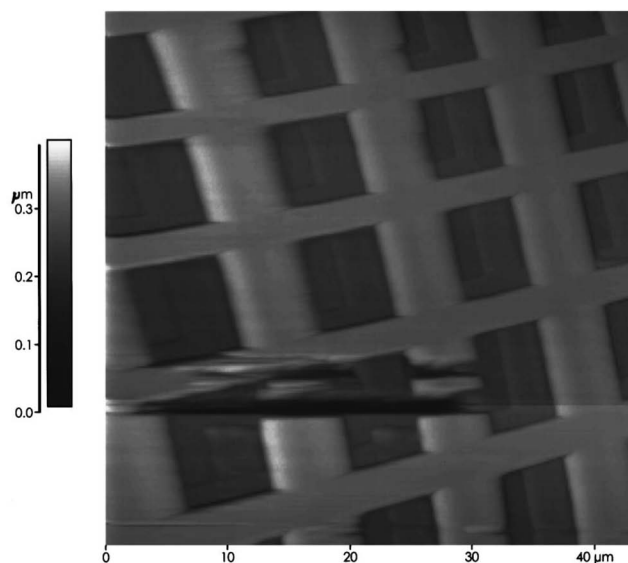


**FIG. 27.** AFM image of a scratched test grating with 10  $\mu\text{m}$  pitch and 100 nm height, scanning speed 0.7 lps, sapphire tip,  $k = 3300 \text{ N/m}$ ,  $A = 250 \text{ nm}$ ,  $\Delta f = +15 \text{ Hz}$ ,  $f_0 = 27\,214 \text{ Hz}$ . Reproduced with permission from F. J. Giessibl, Appl. Phys. Lett. **73**, 3956 (1998). Copyright 1998 AIP Publishing LLC.

a contamination layer, as shown in Fig. 28, or immersed in liquid, is possible as shown by Iichii *et al.*<sup>129</sup> and Wastl *et al.*<sup>252</sup> These contamination layers are a severe challenge because they cause a strong damping of the cantilever, as shown in Fig. 29. For the wet sample, the drive signal had to increase from less than 1 mV when the oscillating tip is outside of the adsorption layer at  $z = 9 \text{ nm}$  to about 40 mV at  $z = 0 \text{ nm}$  for the immersed tip [see Fig. 29(d)], while for a dry sample, the drive only had to increase from about 1 mV at  $z = 2 \text{ nm}$  to about 2.5 mV at  $z = 0 \text{ nm}$  [see Fig. 29(e)]. The analog amplitude controllers we used in the early days of qPlus did not provide enough dynamic range to bridge these large changes in damping. That is why it took 13 years for us after having obtained atomic resolution in late 1999 in vacuum<sup>81</sup> to achieve the same feat in ambient environments. The bottom part of Fig. 29 shows the damping and frequency shift for a dried sample, where the drive signal only had to increase by a factor of three. Figure 30 shows atomically resolved data of KBr. The corresponding publication<sup>252</sup> also describes experiments where craters were made into KBr and the healing process was observed later. Other samples, where atomic resolution in ambient conditions was demonstrated, include graphene<sup>253</sup> and calcite.<sup>254</sup>

#### 3. Atomic resolution of lipid bilayers in thin liquid films

High-resolution imaging of soft biological samples with atomic force microscopy (AFM) is challenging because they must be imaged with small forces to prevent deformation. Typically, AFM of those samples is performed with soft silicon cantilevers ( $k \approx 0.1\text{--}10 \text{ N/m}$ ) and optical detection in a liquid environment. Several complex biologically relevant solutions



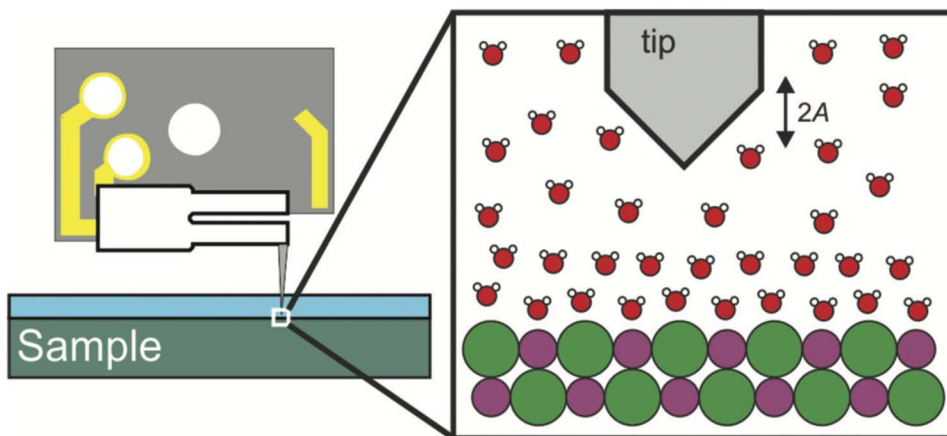


**FIG. 28.** Schematic view of a qPlus sensor on a sample in ambient conditions, where surfaces are covered with a contamination layer.<sup>252</sup> Reprinted with permission from Wastl *et al.*, Phys. Rev. B **87**, 245415 (2013). Copyright 2013 The American Physical Society.

are non-transparent and even change their optical properties over time, such as the cell culture medium we used. Therefore, it makes sense to try these experiments with qPlus sensors. The high stiffness of the qPlus sensor allows us to use small amplitudes in frequency-modulation mode and obtain high  $Q$  factors even in liquid. The samples are immersed in solution in a liquid cell and long tips are used, with only the tip apex submerged. Figure 31 shows molecularly resolved image of lipid membranes in which the individual head groups are resolved. The corresponding publication<sup>195</sup> also shows atomic resolution of mica in ambient conditions and various solvents. Other samples, where atomic resolution in ambient conditions was demonstrated, include graphene<sup>253</sup> and calcite.<sup>254</sup>

#### 4. Atomic resolution in bimodal AFM

As outlined in the second chapter, silicon cantilevers are not stiff enough to allow stable operation at small amplitudes.

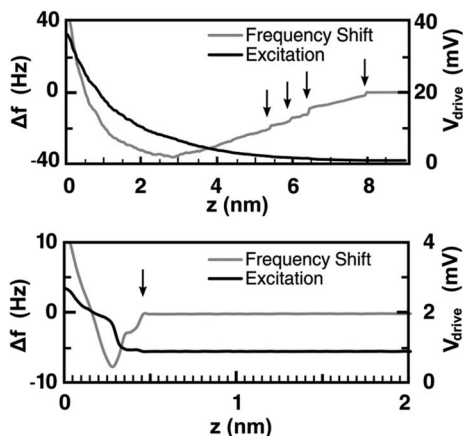


**FIG. 29.** Top: Frequency shift and drive voltage versus distance spectrum for a KBr sample that has been exposed to ambient air at a relative humidity of 53% for three days. Bottom: Spectrum taken within about 10 min after drying the sample with a heat gun. Reprinted with permission from Wastl *et al.*, Phys. Rev. B **87**, 245415 (2013). Copyright 2013 The American Physical Society.

Garcia *et al.*<sup>65</sup> found a workaround: multifrequency AFM, and in particular bimodal AFM, where the cantilever is oscillated with a large amplitude at the fundamental mode and with a small amplitude at the simultaneously excited higher flexural mode. The advantage is that the higher flexural mode is more sensitive to the short range interaction.

We operated a qPlus sensor simultaneously in the fundamental mode 32(a) as well as in the second flexural mode with one node [see Fig. 32(b)].<sup>178</sup> Although the stiffness of the sensor is about 40 times higher in the second flexural mode, we could obtain atomic resolution both in the fundamental mode [see Fig. 32(c)] and in the second flexural mode [see Fig. 32(d)]. However, we found that when both modes are excited, simultaneous atomic resolution in the fundamental and the higher flexural modes is only possible if the sum of the two amplitudes is approximately below 100 pm. As a consequence, the excitation of the fundamental mode reduces the signal-to-noise ratio in the higher flexural modes (and vice versa), and although bimodal AFM is a workaround to prevent jump-to-contact with soft cantilevers, a more straightforward approach is to use cantilevers with sufficient stiffness to prevent instabilities at small amplitudes right away.

However, there is a possible highly interesting application of bimodal AFM. If the mass of the tip is chosen appropriately, the node of the second flexural mode in Fig. 32(b) can move close to the tip position, and the motion of the tip is mainly lateral. This would allow a simultaneous detection of normal forces with the fundamental mode and lateral forces with the second flexural mode. Currently, we are investigating this mode and the future will tell if this approach is feasible.

#### 5. Magnetic force microscopy (MFM)

Force gradients due to the magnetic interaction between the tip and the sample are very small compared to chemical bonding forces. To provide a large signal, i.e., a large frequency shift, the sensor should be as soft as possible to allow operation at the ideal amplitude without suffering from jump-to-contact. As the decay length of magnetic dipole forces is on

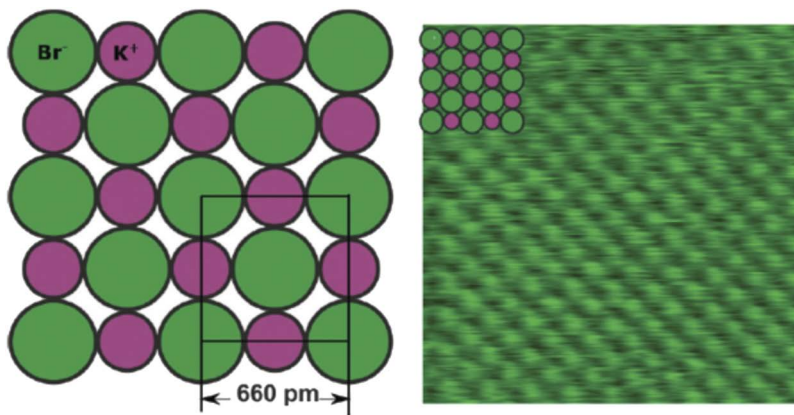


**FIG. 30.** Atomic resolution on KBr in ambient conditions showing atomic resolution. Due to the hydrophilic nature of ionic crystals, the surface is covered by a water layer. Parameters:  $k = 1000$  N/m,  $A = 75$  pm,  $\Delta f = +190$  Hz,  $f_0 = 38\,853$  Hz. Reprinted with permission from Wastl *et al.*, Phys. Rev. B **87**, 245415 (2013). Copyright 2013 The American Physical Society.

the order of the domain size, and the ideal amplitude is on the order of the decay length, large amplitudes on the order of 50 nm are ideal in conventional magnetic force microscopy (MFM) and soft Si cantilevers are ideally suited for this. The qPlus sensor is not ideal for these types of measurements as the sensor should be as soft as possible while maintaining stability at the optimal oscillation amplitude. Nevertheless, Schneiderbauer *et al.*<sup>210</sup> could demonstrate magnetic resolution on a hard disk with milli-Hertz frequency resolution in Fig. 33. The advantage of using the qPlus sensor for MFM is that the same setup that performs the MFM measurement can be used to perform atomically resolved AFM-, STM-, and possibly even exchange force- measurements, once the domain structure has been measured by MFM. The transition from performing MFM to atomically resolved AFM would then merely require amplitude reduction from the ideal MFM value of about 50 nm to the ideal atomic value of about 50 pm.

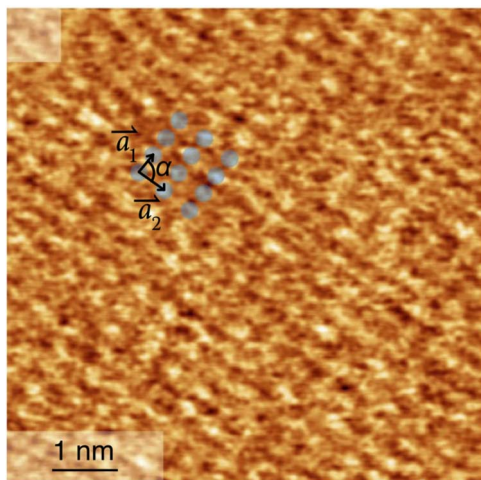


**FIG. 31.** Molecular resolution of a lipid bilayer in solution. Parameters:  $k = 1800$  N/m,  $A = 100$  pm,  $\Delta f = +20$  Hz,  $f_0 = 15\,570$  Hz. Reprinted with permission from Pürckhauer *et al.*, Sci. Rep. **8**, 9330 (2018). Copyright 2018 Author(s), licensed under a Creative Commons Attribution 4.0 License.<sup>36</sup>

## B. Ultrahigh vacuum at room temperature

### 1. Subatomic spatial resolution on silicon and CoSm

In 2000, only two years after the introduction of the qPlus sensor, we reported about the observation of subatomic features by force microscopy.<sup>82</sup> In this experiment (see Fig. 34), a Si covered tungsten tip mounted on a qPlus sensor imaged the Si(111)-(7 × 7) surface. Each adatom appeared as two crescents, interpreted as two dangling bonds. The tip and sample switched roles here, as the dangling bonds on the Si adatoms imaged the front atom of the tip just as the tip

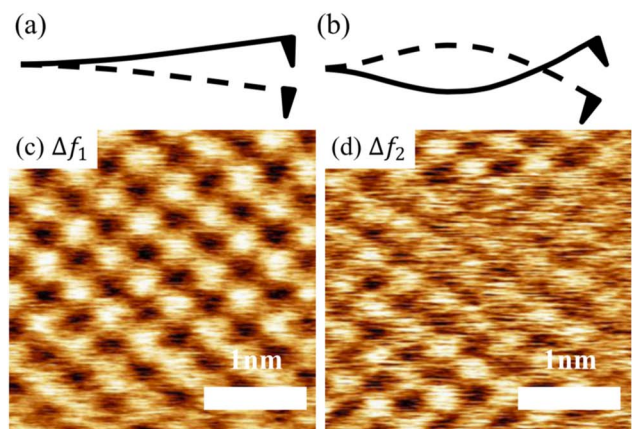


**FIG. 32.** Bimodal AFM with a qPlus sensor.<sup>178</sup> (a) Cantilever deflection in the fundamental oscillation mode. (b) Cantilever deflection in the second flexural mode with one node. The frequency of the second flexural mode is about 6 times as high as the fundamental mode; more precisely  $f_1 = 32\,596.7$  Hz, a quality factor of the first mode  $Q_1 = 2906$ , a free resonance frequency of the second mode  $f_2 = 194\,858.2$  Hz, and a quality factor of the second mode  $Q_2 = 1848$ . The left image is obtained with the fundamental oscillation mode, and the right image is obtained in the first flexural mode. (c)  $\Delta f_1$  image with only the first flexural mode excited at  $A_1 = 75$  pm. (d)  $\Delta f_2$  with only the second flexural mode excited at  $A_2 = 75$  pm. The scan area is  $3 \times 3$  nm<sup>2</sup> and the scan speed is 58 nm/s. For clarity, all images were line-flattened, the frequency shift ranges from 164 to 352 Hz in (c) and from 166 to 220 Hz in (d). Reproduced with permission from Ooe *et al.*, Appl. Phys. Lett. **109**, 141603 (2016). Copyright 2016 AIP Publishing LLC.

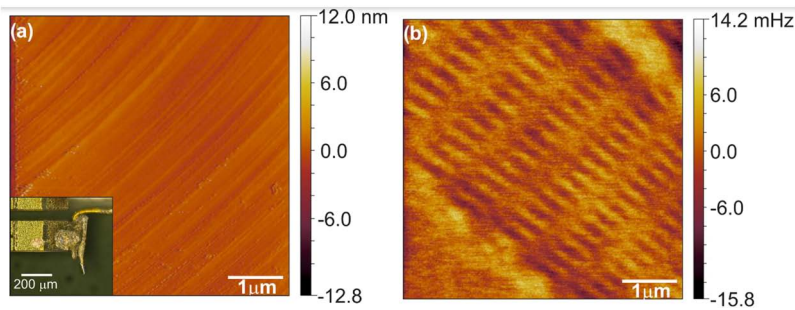


**FIG. 33.** Magnetic force microscopy with a qPlus sensor.<sup>210</sup> (a) Topographic image and (b) magnetic image obtained at a tip height of a few dozen nanometers with the same tip. Reprinted with permission from Schneiderbauer *et al.*, Beilstein J. Nanotechnol. 3, 174 (2012). Copyright 2012 Author(s), licensed under a Creative Commons Attribution 2.0 License.<sup>36</sup>

imaged the surface. The data were explained using the angular dependent Stillinger-Weber potential. The claim of having achieved subatomic resolution raised lively discussions.<sup>127</sup> While the explanation of the data was confirmed by density functional theory,<sup>123,270</sup> the science of tip preparation in 2000 was not as sophisticated as today, where subatomic resolution with atomically characterized tips has been obtained, as discussed in Subsection V C 7. On a side note, the eminent visual artist Gerhard Richter used the orbital image of Si as an inspiration for his offset print “Erster Blick (First View).”<sup>176,199</sup>

Figure 35 is another example where the adatoms of the Si(111)-(7 × 7) produce repeated subatomic images of the front atom of a Co<sub>6</sub>Fe<sub>3</sub>Sm tip.<sup>114</sup>

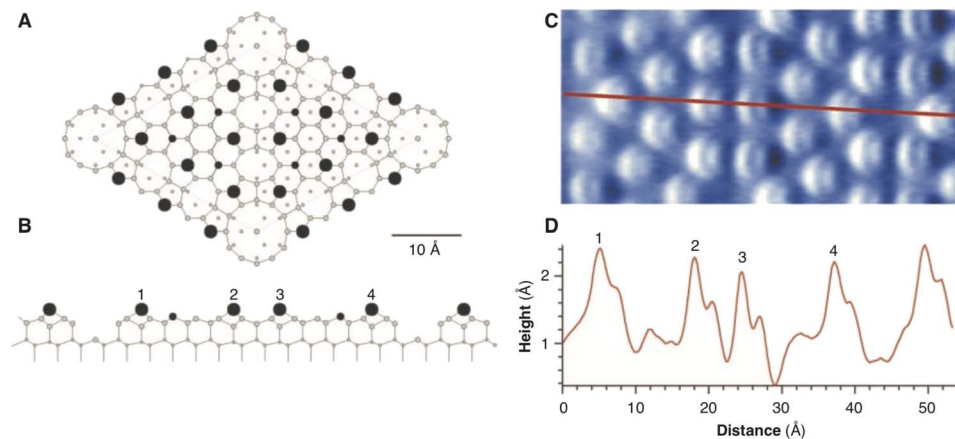
## 2. Insulators—CaF<sub>2</sub>(111) and NiO(100)

Figure 36 shows the atomically resolved CaF<sub>2</sub>(111) surface, highlighting a total contrast inversion due to a tip change—a common occurrence when imaging at close distance at room temperature. Figure 37 displays NiO(100) at room

temperature—as the Neel temperature of NiO is significantly above room temperature, we tried to measure spin contrast due to exchange interaction—this would have produced a 2 × 1 superstructure. Both samples have been revisited using low temperature AFM: CaF<sub>2</sub>(111) was imaged over days with the same tip, and at very high precision<sup>157</sup> and spin contrast, measurements including force spectroscopy on Ni(100) were achieved as well.<sup>190</sup>

## 3. Friction studies by lateral AFM on Si(111) and Si(100)

In 2002, we performed first frictional studies by lateral force microscopy using a laterally oriented qPlus sensor at room temperature and measuring the energy it takes to excite a Si adatom.<sup>85</sup> The dissipation data were explained using the Tomlinson-Prandtl model<sup>194,240</sup> of friction as a plucking action on single molecules. Figure 38 shows a refined experiment on a sample that shows a clear directional dependence of lateral stiffness: Si(100).<sup>260</sup> In Si(100), dimers form at the surface that changes their direction by 90° when going over an atomic step.



**FIG. 34.** (a) Top view and (b) side view of the dimer-adatom-stacking fault (DAS) model of the Si(111)-(7 × 7) surface. Adatoms and rest atoms are emphasized by large and small black spheres, respectively. The left half of the unit cell has a stacking fault, and the right half is unfaulted. The 12 adatoms within one unit cell belong to four different classes. The three adatoms within one class are related by symmetry operations (rotation by 2π/3). The theoretical equilibrium positions of adatoms 1, 2, and 4 are 8.5 pm, 3.1 pm, and 3.8 pm higher than adatom 3, while the height differences as measured by Low Energy Electron Diffraction (LEED) are 12 pm, 8 pm, and 4 pm (11). (c) FM-AFM image (raw data) of the Si(111)-(7 × 7) unit cell.<sup>82</sup> (d) Profile of C. Adatoms 1, 2, and 4 are 34 pm, 19 pm, and 15 pm higher than adatom 3. The split adatom images are explained by a tip exposing two orbitals. Parameters:  $f_0 = 16\,860$  Hz,  $k = 1800$  N/m,  $A = 800$  pm. Reprinted with permission from Giessibl *et al.*, Science 289, 422 (2000). Copyright 2000 AAAS.



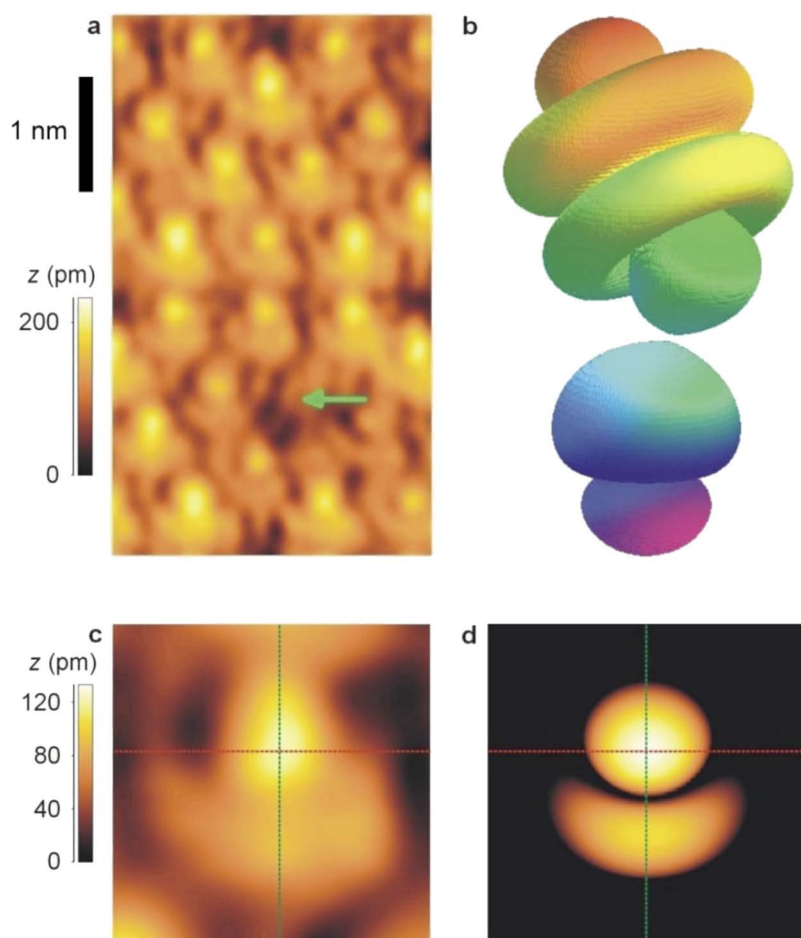


**FIG. 35.** (a) Ultrahigh resolution image of a Si(111)-(7 × 7) surface, acquired by dynamic STM with a Co<sub>6</sub>Fe<sub>3</sub>Sm tip oscillating with an amplitude of  $A = 500$  pm at a sample bias voltage of 100 mV and an average tunneling current  $I_{av} = 200$  pA.<sup>114</sup> The green arrow marks an atomic defect—a missing center adatom. (b) Schematic presentation of the current carrying atomic states leading to the observed image shown in (a). The  $sp^3$  silicon states are tunneling mainly into a Sm  $4f_{z^3}$  tip state tilted by a fixed angle, determined to 37°. (c) Experimental image of a single Si adatom imaged with a Co<sub>6</sub>Fe<sub>3</sub>Sm tip. Average tunneling current  $I_{av} = 1$  nA, sample bias: 100 mV, amplitude  $A = 0.5$  nm. (d) Calculated dynamic STM topography image for a silicon  $3p_z$  sample state and a Sm  $4f_{z^3}$  tip state inclined 37° with respect to the  $z$  axis. The calculation is based on the modified Bardeen approach,<sup>33</sup> in which the cantilever oscillation amplitude  $A = 0.5$  nm is accounted for. Average tunneling current  $I_{av} = 1$  nA, sample bias: 100 mV. The color scales in (c) and (d) are identical. Reprinted with permission from Herz *et al.*, Phys. Rev. B **68**, 045301 (2003). Copyright 2003 The American Physical Society.

#### 4. Submolecular resolution of structure and work function on organic molecules

Submolecular resolution of organic molecules is now a standard practice at low temperatures, where CO terminated tips can be formed. At room temperature, those tips are not stable. Nevertheless, we did obtain high resolution STM, AFM, and decay constant images of semiconducting organic dye molecules (perylene-tetracarboxylic dianhydride, or short PTCDA) in Ref. 124, see Fig. 39. While we cannot be sure about the structure and chemical identity of the tip, it seems likely that we picked up a PTCDA molecule with the tip and that this molecule was oriented such as to expose a corner that terminates with a CO molecule. Similar effects may have played a role in the work of Jarvis *et al.*,<sup>134</sup> who provided atomically resolved images of NTCDI at  $T = 77$  K with a qPlus sensor and a nominal metal tip that might also have been contaminated with the molecule it was imaging—NTCDI also is rectangular and exposes CO terminations at the corners.

#### C. Ultrahigh vacuum at liquid helium temperature (4 K)

Liquid helium temperatures are required to induce some phase transitions, e.g., to obtain a transition from the

normal conducting to the superconducting state for classic superconductors. However, even when low temperatures are not required to cause a specific thermally induced state of the sample, low temperatures have two key advantages for high precision imaging: (a) tip stability and (b) the possibility of slow scanning to reduce noise by recording at low bandwidth  $B$ .

Tip stability is a function of temperature; tips usually change frequently at room temperature, but they can stay unchanged at 4 K for weeks of imaging. The CO tip termination that has been proven so successful in imaging organic matter is only stable for temperatures of liquid helium or slightly above.

When imaging at room temperatures, a relative drift between the tip and the sample induced by temperature gradients and thermal expansion normally requires a certain minimal scanning speed to limit the distorting effects of thermal drift. At low temperatures, distortions are close to zero, and the scanning speed and detection bandwidth of the PLL detector can be reduced to very low values. The all-electric deflection detection and the low power requirement of the amplifier have led to a wide utilization of the qPlus sensor at low temperatures.



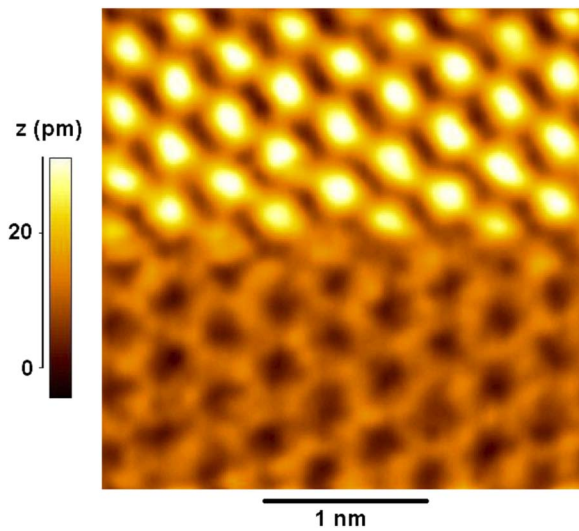


**FIG. 36.** Image of  $\text{CaF}_2(111)$  at room temperature in UHV showing a tip change.<sup>89</sup> Parameters: qPlus sensor with  $f_0 = 16\,740$  Hz,  $Q = 1700$ ,  $k = 1800$  N/m,  $A = 625$  pm,  $\Delta f = -8.8$  Hz, and a relatively blunt tungsten tip. Reproduced with permission from Giessibl *et al.*, *Nanotechnology* **15**, 84 (2004). Copyright 2004 IOP Publishing.

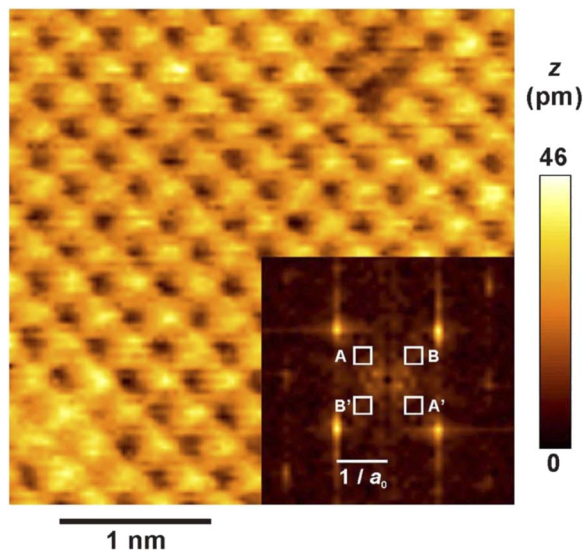


**FIG. 37.** FM-AFM image of a  $\text{NiO}(001)$  surface taken with a  $\text{NiO}$  tip in vacuum at room temperature.<sup>212</sup> Parameters:  $f_0 = 43\,618$  Hz,  $k = 4020$  N/m,  $A = 100$  pm, and  $\Delta f = -98$  Hz (raw data). The presence of the two defects in the upper right and in the lower left corner shows that true atomic resolution is obtained, i.e., a single tip atom is responsible for imaging. The inset shows the central section of the Fourier transform of the topographical image. A peak at half the spatial frequency of one of the two base peaks would be visible if the contribution of the exchange interaction was larger than instrumental noise. However, we did not observe a distinguished peak at half the inverse lattice vectors as would be expected for a  $2 \times 1$  spin superstructure. Reprinted with permission from Schmid *et al.*, *Phys. Rev. B* **77**, 045402 (2008). Copyright 2008 The American Physical Society.

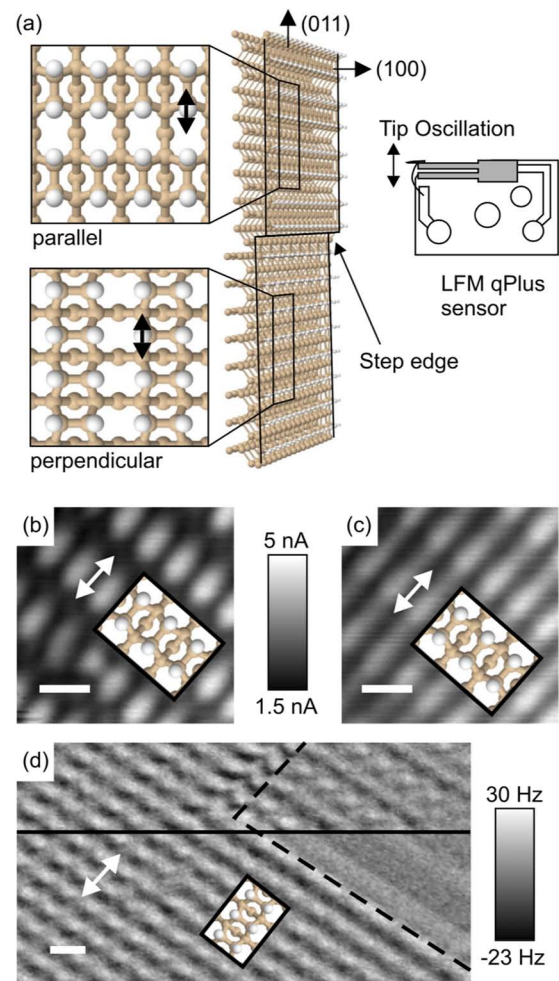


**FIG. 38.** Lateral force measurements on  $\text{Si}(100)$ .<sup>260</sup> (a) A schematic of the experimental setup. By cutting the Si wafer on the (011) planes, the (011) crystallographic direction can be aligned with the tip oscillation. By moving from one terrace to another, data can be acquired with the tip oscillating either parallel or perpendicular to the Si dimers. (b) Constant-height  $I_t$  data at a lateral oscillation amplitude of 50 pm. (c) Same as (b) but with an amplitude of 300 pm. (d)  $\Delta f$ -data over two terraces, with the step edge highlighted with a dashed line. A bias of 1.5 V was applied. Above the black line,  $I$  is used to control the tip height (set point of 4 nA). Below it, the feedback is switched off. The tip oscillation in all subfigures is indicated by double-headed arrows. Images are taken with a scan angle of  $45^\circ$ . White scale bars represent 500 pm. Reprinted with permission from Weymouth *et al.*, *Phys. Rev. Lett.* **111**, 126103 (2013). Copyright 2013 The American Physical Society.

This subsection is organized in the following way: we start by describing the first steps of qPlus operation at liquid helium temperatures that were conducted at the University of Augsburg from 2002. Then, a description of collaborations with the low-temperature STM laboratories at IBM Almaden in San Jose, USA, and R schlikon, Switzerland, follows. In parallel, several companies adopted the qPlus sensor for their commercial low temperature scanning probe microscopes, leading

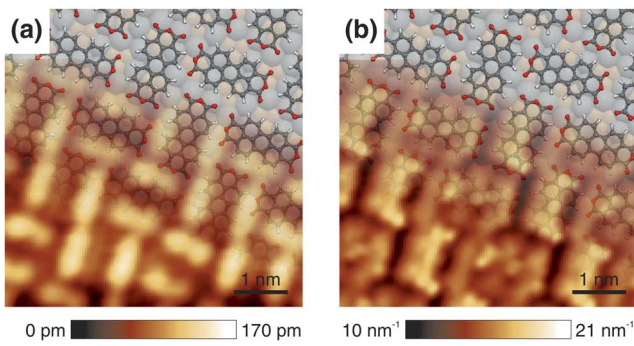


**FIG. 39.** Perylenetetracarboxylic dianhydride (PTCDA) imaged by simultaneous qPlus based STM/AFM.<sup>124</sup> (a) STM topography in which neighboring molecules appear to be similar and (b) simultaneously acquired  $\kappa$  (decay rate of tunneling current) image in which there is a clear contrast between neighboring molecules. Parameters:  $V_{\text{bias}} = -1.2$  V,  $I_t = 200$  pA,  $A = 50$  pm. Reprinted with permission from Huber *et al.*, Phys. Rev. Lett. **115**, 066101 (2015). Copyright 2015 The American Physical Society.

to an increasing number of external results. The early Augsburg results will be followed by new experiments that were conducted after my transition to Regensburg in 2006. From 2010 on, several groups installed commercial 4 K qPlus based STM/AFMs in their laboratories and many interesting results were obtained in parallel around the globe, and it is difficult to sort these results in a timeline. However, many of these groups focused on specific sample systems and the ordering is following a more or less arbitrary list of results obtained by various research groups.

### 1. Simultaneous STM and AFM on graphite

Graphite has been studied from the early days of scanning probe microscopy. When our first 4 K qPlus microscope became operational in Augsburg around 2002, graphite was one of the first samples we investigated.<sup>111,113</sup> Due to its stacking symmetry in the highest available grade of HOPG (highly oriented pyrolytic graphite), only one of the two basis atoms in one unit cell appears in an STM image, while both appear in AFM at close distance with repulsive interaction. The explanation is given by the electronic structure of graphite. In an isolated carbon atom, the six electrons display a  $1s^2 2s^2 2p^2$  distribution, following Hund's rules. In graphite, three of the four electrons in the second shell hybridize to  $sp^2$  orbitals that bond covalently with their three nearest neighbor atoms. The fourth electron of the second shell is in the  $2p_z$  state. The two atoms in the unit cell of graphite are different—the so-called  $\alpha$  atoms (or A atoms) have a direct neighbor in the atomic plane underneath and the  $2p_z$  states of these  $\alpha$  atoms overlap, leading to a slightly lower energy than the one of the  $\beta$  atoms (or B atoms) that do not have direct neighbors underneath and therefore expose a slightly higher energy. Therefore, the electronic states at the Fermi energy display a local maximum on top of the  $\beta$  atoms. As the STM image is a map of the charge density at the Fermi level, STM shows only the  $\beta$  atoms. By contrast, AFM (in the repulsive regime) is sensitive to the total charge density and therefore shows both  $\alpha$  and  $\beta$  atoms.

Figure 40 shows the experimental data and simulation below. The repulsive forces that are imaged in the experimental AFM image (b) are increasing with the charge density; thus, a charge density plot is a good approximation for a

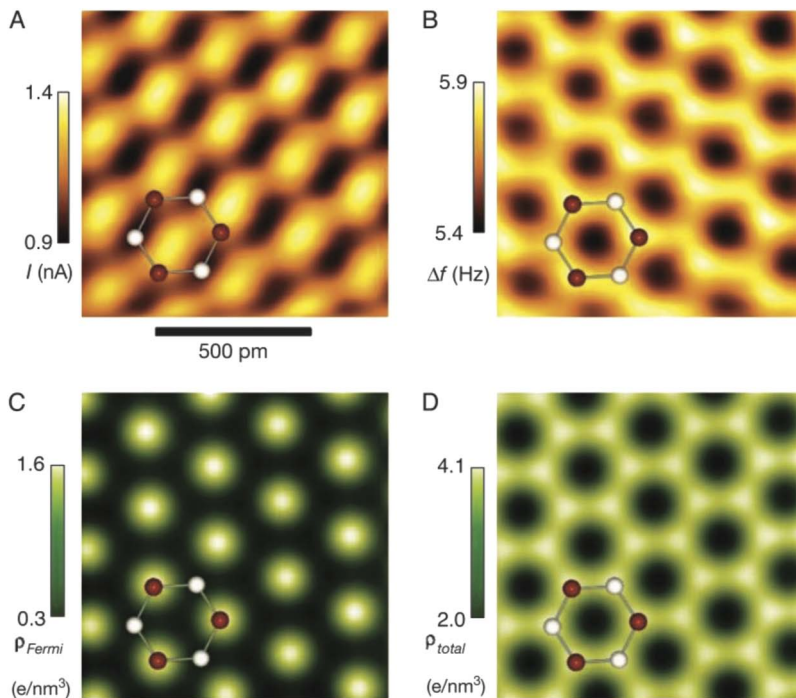


**FIG. 40.** Experimental [(a) and (b)] and simulated [(c) and (d)] STM and AFM images of graphite.<sup>111</sup> One hexagonal surface unit cell with the two basis atoms  $\alpha$  (white) and  $\beta$  (red) is superimposed for clarity. (a) Tunneling current image of graphite in the constant-height mode [parameters for (a) and (b)  $V_{\text{bias}} = 100$  mV,  $f_0 = 18\,076.5$  Hz,  $k = 1800$  N/m,  $A = 300$  pm, scanning speed 200 pm/s]. Only the  $\beta$  atoms appear in the STM image. Note that the experimental STM image is shifted slightly with respect to the AFM image (see text). (b) Frequency shift image, simultaneously recorded with (a) showing both  $\alpha$  and  $\beta$  atoms. (c) The calculated charge density of graphite at the Fermi level  $E_{\text{Fermi}}$  at a height of 200 pm over the surface plane. The maxima of  $E_{\text{Fermi}}$  are at the atom positions. (d) Calculated total charge density, also at a height of 200 pm over the surface plane. Reprinted with permission from Hembacher *et al.*, Proc. Natl. Acad. Sci. U. S. A. **100**, 12539 (2003). Copyright 2003 National Academy of Science (USA).



repulsive AFM image. Note that the experimental STM image (a) is shifted with respect to the AFM image by 68 pm toward the 1 o'clock position, probably caused by a slightly asymmetric tip. The experimental image in (b) and the calculated charge density shown in (d) have local maxima over  $\alpha$  and  $\beta$  sites. This experiment, in addition to the data on Si of 2000,<sup>82</sup> provided more evidence that AFM can provide greater spatial resolution than STM, in contrast to common experience at that time. The calculated charge densities have stimulated visual artist Gerhard Richter to create “Graphit (2005)” and some variations thereof in his reference collection “Atlas.”<sup>176,200</sup>

## 2. Higher harmonic AFM

As outlined in Subsection II E, the tip-sample interaction not only changes the oscillation frequency of the force sensor but also introduces higher harmonics if the tip-sample force is nonlinear. Although the magnitude of the higher harmonics is small, they are even more sensitive to short range interactions than the frequency shift for small amplitudes. Figure 41 from Ref. 112 shows a very high resolution image of the W tip atom as imaged by graphite. The higher harmonic image shows even better spatial resolution than the frequency shift image (see Ref. 91). This result is another example of the reciprocity principle outlined in Julian Chens book on STM<sup>33</sup>—similar to the example of Si in Ref. 82, the surface atoms of the sample image the front atom of the tip just as the tip images the sample. If the surface atoms of the sample are smaller than the tip atoms, they create a repeated image of the tip atom.

In Fig. 41, all the higher harmonics are summed up by routing the deflection signal into a high-pass filter and a

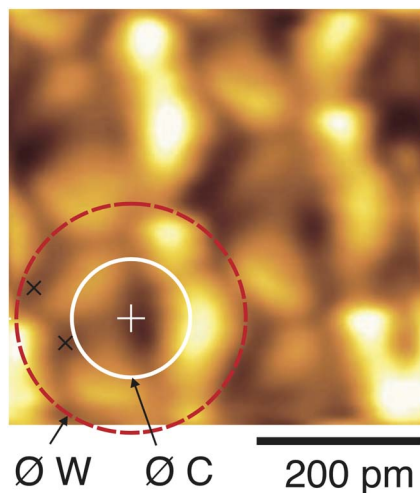


**FIG. 41.** High resolution higher harmonic constant-height image of a graphite surface imaging a W tip, demonstrating a lateral resolution of 77 pm (distance between the black crosses<sup>112</sup>). The solid circle has a diameter of 142 pm, indicating the diameter of a carbon atom. The dashed circle shows the diameter of a tungsten atom (274 pm). The white cross marks the center of the circles. Parameters:  $V_{\text{bias}} = 100$  mV,  $f_0 = 18\,076.5$  Hz,  $k = 1800$  N/m,  $A = 300$  pm,  $Q = 20\,000$ , scanning speed 200 pm/s. Reprinted with permission from Hembacher *et al.*, Science **305**, 380 (2004). Copyright 2004 AAAS.

rms-to-dc converter (see Ref. 112 for details). The simultaneously recorded tunneling current image [not shown here, see Fig. 2(e) in Ref. 112] ranged from 2.0 to 2.7 nA. It is interesting to note that only every second atom of the graphite surface images a tungsten tip atom, and it is therefore probable that the bonds between the surface atoms under the tip have been rehybridized to a diamond-like bonding under the pressure of the tip. Wright and Solares<sup>266</sup> calculated the contrast for such a tip terminated by a tungsten atom oriented in a (001) direction and confirmed the fourfold symmetry, but some open questions remain.

## 3. Current-induced electrostatic forces

In scanning tunneling microscopy, atomic resolution is usually possible over a quite large distance range. At a metallic single atom point contact, the conductance of the junction is approximately  $G_0 = 1/12.9$  k $\Omega$ , leading to a current of  $I = 1$   $\mu$ A for a bias of  $V_{\text{bias}} = 12.9$  mV. As the tunneling current typically decays by a factor of 10 for every distance increase of 100 pm, a distance of 600 pm is easily possible as a current of 1 pA can still be measured conveniently. In AFM, the situation is different. Initially, atomic resolution was only possible at very small distances where the forces are maximal and sufficiently large to be detectable. Thus, when approaching the probe of a combined STM/AFM from far to the sample, one usually first detects a tunneling current long before forces become noticeable. We were quite surprised when we performed a combined STM/AFM experiment on Si(111)-(7  $\times$  7) shown in Fig. 42(a). At a tunneling current of about 2 nA and the bias of  $V_{\text{bias}} = 1.5$  V in Fig. 42(a), we estimate an average distance on the order of 500 pm. Nevertheless, the frequency shift channel on the right shows a pronounced repulsion on top of the adatoms. As we could not explain the origin of this strong repulsive force immediately, we named it “phantom force.” This force was apparently related to the tunneling current, demonstrated by Fig. 42(b) where again STM and AFM channel were recorded at zero bias. Approaching the tip 340 pm closer to the surface in Fig. 42(c), again at zero bias, of course also did not show any current but the attractive forces on top of the adatoms, i.e., the adatoms appeared dark, indicating attraction. Based on the correlation between tunneling current and frequency shift shown in the bottom section of Fig. 43, we speculated that the phantom force may have its origin in the limited conductivity of our semiconducting sample. When a weakly conductive sample is subject to a local current injection, the surface potential can change over a larger area, reducing the voltage differential between the tip and the sample and thus reducing the electrostatic attraction, feigning a repulsive force that is proportional to the tunneling current. We tested this hypothesis with a setup outlined in the top of Fig. 43. In this experiment, a switch allows us to either directly connect the sample to the current-to-voltage converters (a) or to put a resistor  $R_1 = 10$  M $\Omega$  (b) or  $R_2 = 30$  M $\Omega$  in series with the sample. If our hypothesis was correct, a resistor in series to the resistance of the sample should increase the phantom force effect, verified by the increasing slope of the  $\Delta f(I)$  curves shown in the bottom of Fig. 43. The data perfectly agreed with the theory of the

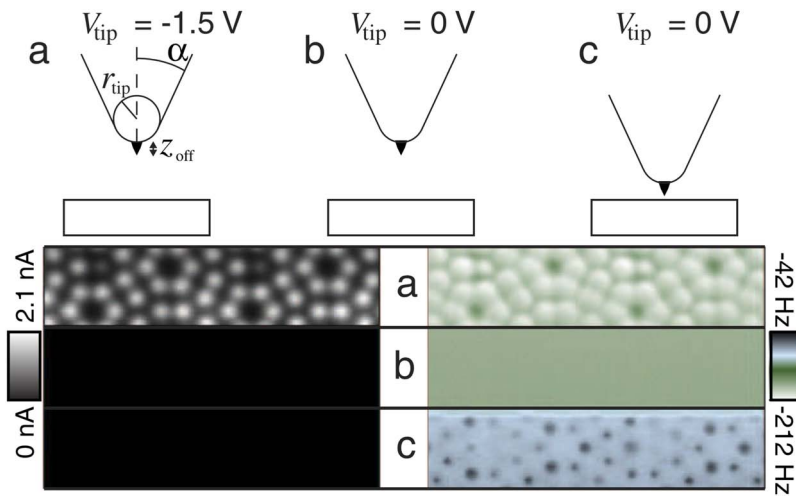


**FIG. 42.** Measuring current-induced forces with combined STM/AFM.<sup>259</sup> Top: Tip and sample arrangement of the experiment in states (a) (far away, bias  $V_{bias} = 1.5$  V), (b) [same distance as (a), bias  $V_{bias} = 0$  V], and (c) [340 pm closer than (a) and (b), bias  $V_{bias} = 0$  V]. Bottom: Simultaneous  $I$  (left) and  $\Delta f$  data (right) acquired at  $T = 4.5$  K. (a)  $V_{bias} = 1.5$  V. (b)  $V_{bias} = 0$  V. (c) Tip is approached 340 pm closer to the surface. Data were collected at  $A = 100$  pm,  $f_0 = 16\,777$  Hz, image size of each strip  $8 \times 2$  nm<sup>2</sup>. Reprinted with permission from Weymouth *et al.*, Phys. Rev. Lett. **106**, 226801 (2011). Copyright 2011 The American Physical Society.

phantom force as a current induced drop of differential tip-sample voltage.

Münnich *et al.* have studied a related phenomenon by combined STM and qPlus AFM—tip induced band bending.<sup>171</sup>

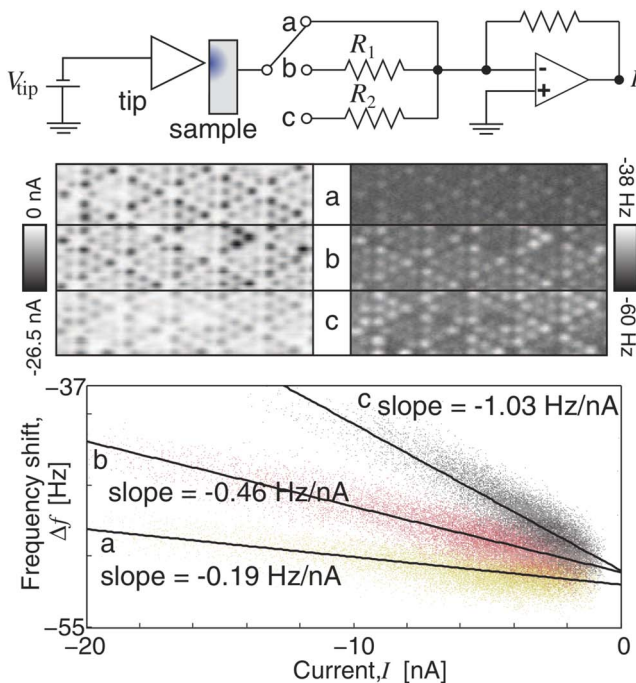


**FIG. 43.** Experiment where the current induced force is modified by external resistors in series.<sup>259</sup> Top: Schematic of the experiment showing the tip, the sample, and the current amplifier with a switch that allows us to connect resistors in series with the sample. Middle: Simultaneous  $I$  and  $\Delta f$  data. Bottom:  $\Delta f$  versus  $I$  data. (a)  $R = 0$  between the sample and ground. (b)  $R_1 = 10$  M $\Omega$ . (c)  $R_2 = 30$  M $\Omega$ . Data were acquired with  $V_{bias} = 1.5$  V,  $A = 400$  pm,  $f_0 = 19\,390$  Hz, image size  $10 \times 7$  nm<sup>2</sup>. Reprinted with permission from Weymouth *et al.*, Phys. Rev. Lett. **106**, 226801 (2011). Copyright 2011 The American Physical Society.

#### 4. Measurement of forces that act during atomic manipulation

In 1990, Donald Eigler and Erhard Schweizer used the tip of a 4 K STM to move individual Xe atoms on a Ni(110) surface and spelled out “IBM” at the IBM Research Laboratory in Almaden,<sup>51</sup> fulfilling Richard Feynman’s dream in his December 1959 lecture *There’s Plenty of Room at the Bottom: An Invitation to Enter a New Field of Physics*.<sup>61</sup> Toward the end of his talk, Feynman made the following statement: “But I am not afraid to consider the final question as to whether, ultimately – in the great future – we can arrange the atoms the way we want; the very atoms, all the way down! What would happen if we could arrange the atoms one by one the way we want them (within reason, of course; you can’t put them so that they are chemically unstable, for example).” This last comment “within reason, of course” is very important. Eigler and Schweizer used Xe atoms that bond mainly by the weak van der Waals interaction to the surface, and they picked the Ni(110) surface that has grooves in it in contrast to densely packed (111) surfaces to prevent thermally activated motion of the Xe atoms on the surface. The driving forces behind atomic manipulation were not accessible by STM. Therefore Andreas Heinrich, Eigler’s successor at IBM, was very eager to add AFM capability to STM to measure the forces that drive atomic manipulation. This upgrade was relatively simple by replacing the tunneling tip of Eigler’s STM with a qPlus sensor such that combined STM and AFM became possible.<sup>239</sup> In this study, we could finally measure the forces that act in atomic manipulation (Fig. 44). In atomic manipulation by STM, the tip remains steadily close to the atom that is manipulated. In combined STM/AFM, we need to oscillate the tip such that the distance between the tip and the atom varies by  $2A \approx 100$  pm. Nevertheless, atomic manipulation with a vibrating tip was possible with a similar behavior as with a steady tip. We label selected line scans with the closest approach  $z'$  during the oscillation [see note (15) in Ref. 239 for the determination of absolute  $z$  values]. The measurement occurs in several steps. First, the average force gradient in the  $z$ -direction is integrated twice to obtain



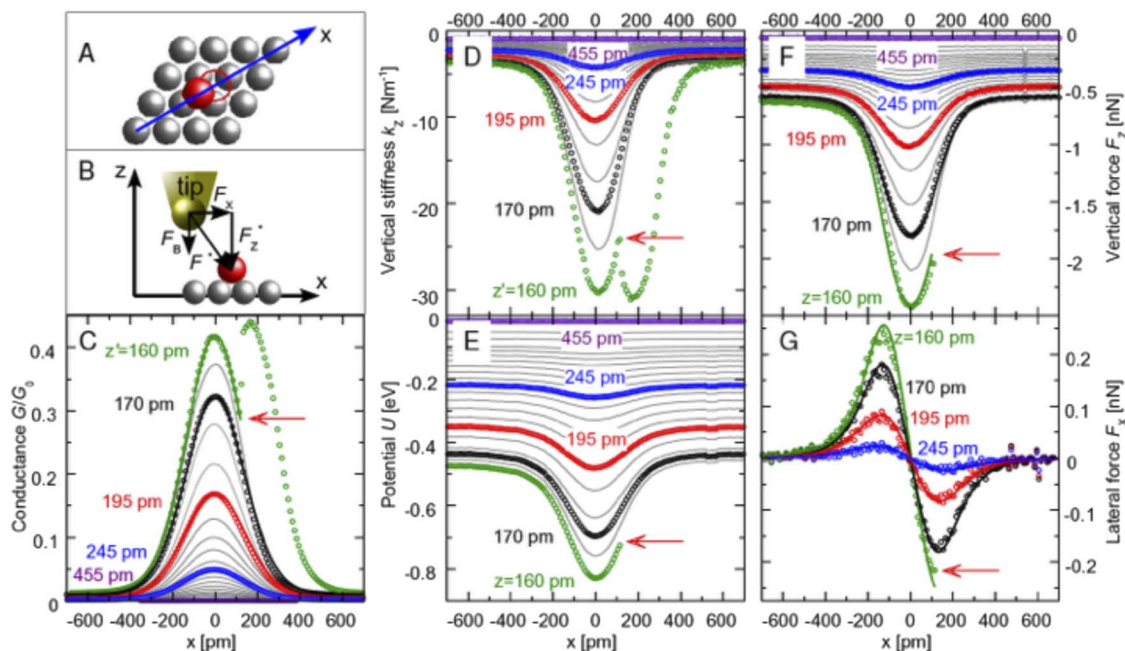


**FIG. 44.** Measuring the force to move a single Co atom on a Pt(111) surface.<sup>239</sup> (a) Schematic top view of the Pt(111) surface atoms (gray) and the adsorbed Co atom (red). In the following panels, constant-height line scans (b) in the direction of easiest adsorbate motion ( $x$  direction) were taken at successively reduced tip-sample separations until the Co atom hopped to the adjacent adsorption site [red circle in (a)]. The scan speed was approximately 500 pm/s. (b) The force  $F^*$  between the tip apex and the Co atom can be divided into the lateral force  $F_x^*$  and the vertical force  $F_z^*$ . The total vertical force  $F_z$  is the sum of  $F_z^*$  and the background force  $F_B$ . [(c) and (d)] Simultaneously measured conductance  $G$  and stiffness  $k_z$  (circles and gray lines). Note that these values are time-averaged over the cantilever oscillation between  $z = z'$  and  $z = z' + 2A$ . [(e)–(g)] Tip-sample interaction energy  $U$ , vertical force  $F_z$ , and lateral force  $F_x$  extracted from the stiffness  $k_z$  data in (d). Selected line scans are labeled with the tip height  $z$ ; here, the oscillation amplitude has been deconvolved from the curves. The red arrows in (c)–(g) indicate the hop of the Co atom to the neighboring binding site. Colored lines in (c), (f), and (g) are fits with the s-wave model. Reprinted with permission from Ternes *et al.*, Science 319, 1066 (2008). Copyright 2008 AAAS.

the potential energy. The lateral derivative of the inverted potential energy yields the lateral forces.<sup>117</sup> It turned out that the required forces depend both on the substrate and on the adsorbed species—it is easier to move a Co atom across Cu(111) than a CO molecule, and Pt(111) is stickier than Cu(111).<sup>239</sup> More recently, our Regensburg group found evidence for a lowering of the manipulation threshold due to the presence of the probe tip,<sup>52</sup> and very recently, we demonstrated atomic manipulation with CO terminated tips.<sup>18</sup> Atomic inlays created by controlled atom manipulation have been obtained using conventional Si cantilever AFM.<sup>228</sup>

### 5. Carbon monoxide front atom identification (COFI)

The carbon monoxide front atom identification (COFI) method was introduced in 2012<sup>257</sup> and uses a CO molecule that bonds upright to a closed packed metallic surface, e.g., Cu(111), as shown in Fig. 45. A constant-height STM image shows a dip in the current, and a simultaneously recorded frequency shift image shows much more structure. The initial interpretation concluded that all three tips shown in Fig. 45 were single tips, based on the similarity of their STM data. A later study<sup>53</sup> has proved that tip 2 was a dimer tip, and tip 3 was a trimer tip. This 2015 study points out the erroneous interpretation from 2012 in the abstract and provides a detailed comparison of the profound similarities between

single-, dimer-, and trimer tips interacting with CO/Cu(111) and a CO tip that images single adatoms, dimers, and trimers as shown in Fig. S11 of Ref. 53.

In addition to resolving the structure of the front section of the tip, COFI also allows us to draw information about the chemical identity of the tip, as found in Ref. 121. Figure 2 in this publication shows that tips that have a Cu atom at the apex display a maximal attractive force of about 130 pN to CO/Cu(111), while Fe and W terminated tips show a maximum of about 250 pN. This chemical identification by the maximal attractive force follows the work of Sugimoto *et al.* who distinguished three atomic species silicon, tin, and lead by their force profile.<sup>229</sup>

### 6. Metallic surfaces and metal clusters

In preparation to the studies that later determined the forces that act in atomic manipulation at the IBM Almaden Research Laboratory,<sup>239</sup> we accidentally picked up CO on the tip and obtained high resolution images of the Pt(111) surface in an unpublished experiment of June 2007, shown in Fig. 46. The dark spots in the STM channel coincide with the dark spots in the frequency shift channel, and they are located at the positions of the Pt surface atoms. The reason of contrast inversion in the STM channel is due to the  $p_x$ ,  $p_y$  states that lead to reverse contrast,<sup>33</sup> and the dark spots above Pt in the AFM

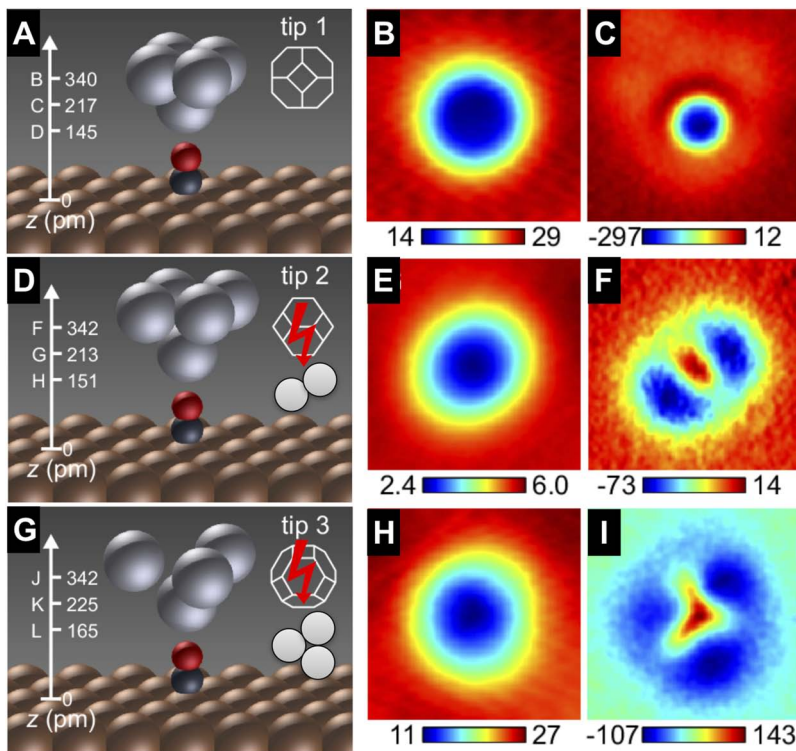


**FIG. 45.** Carbon monoxide front atom identification as a tool to precisely measure the tip structure.<sup>257</sup> Left column: schematic setup of the tip and sample. A CO molecule that bonds vertically to a densely packed metal surface as Cu(111) acts as a probe to inspect the tip. For low bias voltages, CO appears dark. Because the width of the minima over CO was similar for all three tips, the initial assumption was that all three tips expose a single atom at the front that only changes by its bonding orientation indicated by the orientation of the bcc Wigner-Seitz cell in the right top inset of the left column images. A later study<sup>53</sup> has confirmed that panels (a)–(c) had a single atom tip but also has clearly shown that tip 2 in panels (d)–(f) had two atoms at the front and tip 3 in panels (g)–(i) had three front atoms. Center column: constant-height data of tunneling current in nA. Right column: constant-height force data in pN. Reprinted with permission from J. Welker and F. J. Giessibl, *Science* **336**, 444 (2012). Copyright 2012 AAAS.

channel denote increased attraction. The increased attraction of CO tips over metallic surface atoms was later also observed on Cu(111)<sup>53,213</sup> and Cu(100).<sup>211</sup>

The measurement of the distance dependence of current and forces of single adatoms on a metallic surface allowed to precisely determine the force versus distance dependence of metallic bonding forces—it turned out that they have a similar exponential distance dependence as the tunneling current that decreases to 1/10 for every distance reduction of 100 pm.<sup>238</sup>

In scanning tunneling microscopy, metal clusters consisting only of a few atoms usually cannot be resolved atomically. Instead, the number of atoms involved can be inferred by their height (see the top row in Fig. 47). A qPlus sensor with a CO terminated tip resolves the atoms one by one, as shown in the second and third rows of Fig. 47.<sup>53</sup> The bottom row shows the adsorption sites, calculated by DFT.

Wedge-shaped Pb islands grown on silicon were studied by Mao et al.<sup>158</sup>

### 7. Subatomic spatial resolution on copper and iron adatoms

Three examples of silicon or graphite samples that produce repeated subatomically resolved images of the tip's front atom had been collected in the first five years of using the qPlus sensor in AFM. Non-spherical images of the tip's front atom had been found in a possible Si front atom in Ref. 82, in a possible Sm front atom,<sup>114</sup> and in a possible W front atom.<sup>112</sup> While these results were promising steps forward, they revealed the structure of the tip atom being imaged by the sample. The real purpose of microscopy is to image a sample, not to inspect the probe tip. Therefore it was an important step to create very well defined tips and image a precisely defined adatom as a sample at subatomic resolution. Starting

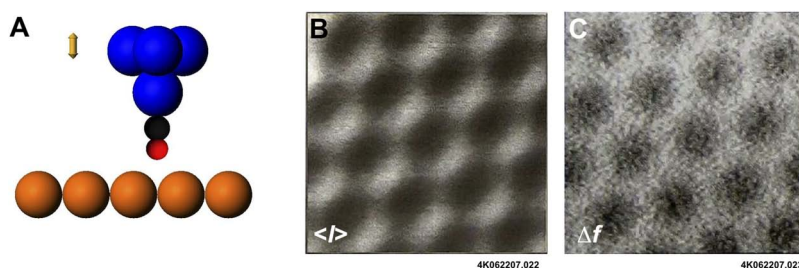


**FIG. 46.** (a) A metal tip terminated by a CO molecule. The tip is attached to a qPlus sensor with  $f_0 = 21\,860$  Hz,  $Q = 50\,000$ , and  $k = 1800$  N/m that oscillates at an amplitude of 50 pm. (b) Constant-height current image and (c) simultaneously recorded constant-height AFM (frequency shift) image. The bias voltage was 10 mV, and the current ranges from 4.5 to 5.5 nA. The frequency range in (b) ranges from  $-10.6$  to  $-8.7$  Hz.<sup>90</sup>



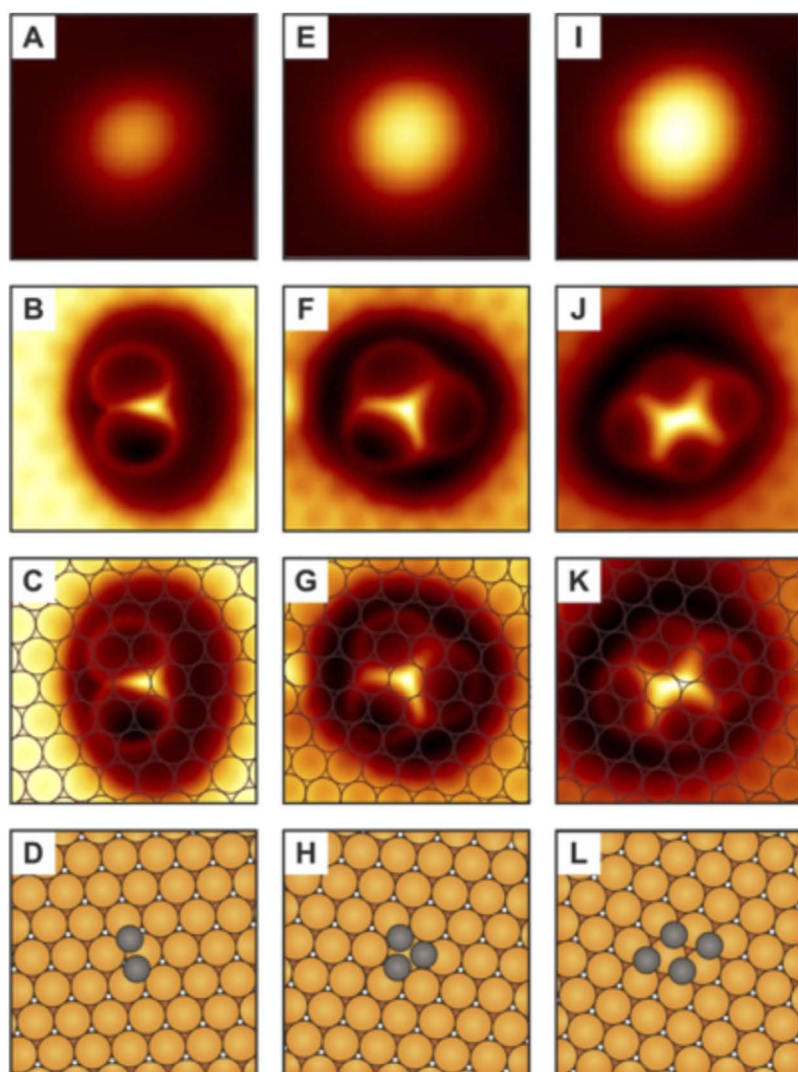


**FIG. 47.** Dimers, trimers, and tetramers imaged by STM, AFM, and their calculated adsorption sites.<sup>53</sup> The first row shows constant-current STM data using a metal tip [(a), (e), and (i)] of an Fe dimer on Cu(111) (left column), Fe trimer (center column), and Fe tetramer (right column). The second row [(b), (f), and (j)] shows the AFM signal (frequency shift) recorded in constant-current topographic imaging with a CO-terminated tip. The dark spots in the flat regions correspond to Cu surface atoms that allow us to register the lattice overlay in the third row [(c), (g), and (k)]. The last row [(d), (h), and (l)] shows the proposed adsorption sites, indicating top, fcc, and hcp positions. An adatom centered on a fcc site thus continues the bulk fcc structure, whereas an adatom on a hcp site would break the crystalline order of the bulk. DFT calculations reveal that dimers (D) adsorb the two Fe atoms close to two next-nearest bridge sites. Reprinted with permission from Emmrich *et al.*, *Science* **348**, 308 (2015). Copyright 2015 AAAS.

in 2012, we imaged single adatoms on flat surfaces with CO terminated tips, discussed in Ref. 53. Figure 48(a) shows a Cu adatom on Cu(111) at very close imaging distance. We see a repulsive center and a repulsive ring. Figure 48(b) shows a Cu adatom on Cu(110) at very close imaging distance, displaying

a repulsive ring with two bumps. For the iron adatom on Cu(111), displayed in Figs. 48(c) and 48(a), a repulsive ring with three bumps on it emerges. The subatomic features in the experimental images of Cu and Fe adatoms have recently been reproduced with DFT calculations by Ref. 271.

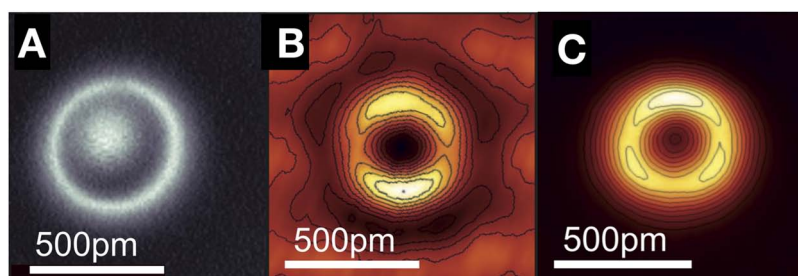


**FIG. 48.** AFM images of single adatoms on a copper surface using a CO terminated tip.<sup>53</sup> (a) AFM image of a Cu adatom on Cu(111) at very close imaging distance. (b) Cu adatom on Cu(110) at very close imaging distance. (c) Fe adatom on a Cu(111) surface. Reprinted with permission from Emmrich *et al.*, *Science* **348**, 308 (2015). Copyright 2015 AAAS.

## 8. Kelvin probe measurements

In parallel to the introduction of the qPlus sensor to the IBM Almaden laboratory, the technology was also transferred to Gerhard Meyer's group at IBM Rüschlikon. In 2004, Repp *et al.* had found a way to charge gold atoms on a NaCl layer.<sup>197</sup> Meyer *et al.* repeated these experiments with the added AFM capabilities offered by the qPlus sensor. A Kelvin probe measurement would allow to confirm that charge transfer, predicted by density functional theory before,<sup>197</sup> actually took place. The combined STM/AFM experiment in Ref. 94 as outlined in Fig. 49 confirmed the charging of the single gold adatom by a shift of Kelvin parabolas for charged versus uncharged gold adatoms. In a combined STM and AFM constant-height experiment, the charged Au atom showed less current in the STM image than the neutral Au atom because the charged Au atom sinks into the surface as depicted in the inset of Fig. 49(a). However, the charged Au atom shows a more negative frequency shift than the neutral Au atom due to the larger electrostatic interaction, also indicated by the more negative frequency shift of the Au<sup>-</sup> Kelvin parabola in Fig. 49(a).

Kelvin probe measurements using the qPlus sensor have also been performed on Si surfaces<sup>19</sup> and on Pb islands.<sup>156</sup> Equalizing the local contact potential by Kelvin probe microscopy is a standard procedure to minimize

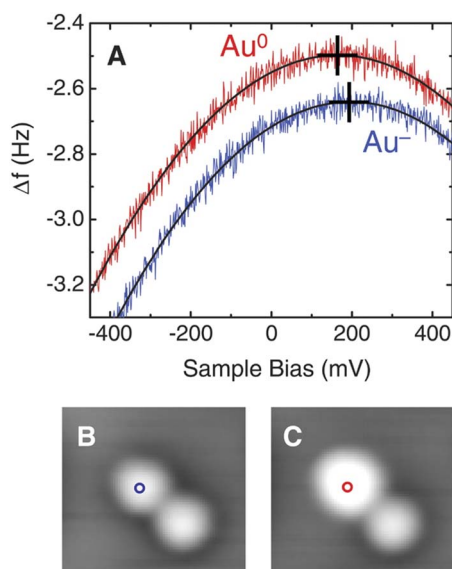


**FIG. 49.** Kelvin probe microscopy on an adsorbed gold atom.<sup>94</sup> (a) Frequency shift measured as a function of the voltage above Au<sup>-</sup> and Au<sup>0</sup>. Both measurements are performed without moving the tip ( $A = 60$  pm and  $\Delta z = 0.58$  nm; raw data). After measuring  $\Delta f(V)$  above Au<sup>-</sup>, the charge state is switched to Au<sup>0</sup> by applying a bias pulse of  $V = 1$  V for a few seconds. Parabolic fits and corresponding parabola peaks are indicated. STM images ( $I = 7.4$  pA,  $V = 50$  mV, and size =  $2.9$  nm  $\times$   $2.7$  nm) before (b) and after (c) the  $\Delta f(V)$  measurements confirm the charge-switching event and show that the switched Au atom has maintained its lateral position. Reprinted with permission from Gross *et al.*, *Science* **324**, 1428 (2009). Copyright 2009 AAAS.

electrostatic interaction in imaging insulators, e.g., in imaging NiO(001).<sup>190</sup>

## 9. Atomic resolution of organic molecules, graphene, and graphene nanoribbons

In 2009, Leo Gross *et al.* discovered that picking up a CO molecule on the metal tip of a qPlus sensor resulted in a dramatic increase in resolution in the AFM channel<sup>95</sup> of an organic (pentacene) molecule displayed in Fig. 50(a). The group used a qPlus sensor with a PtIr tip and noticed that a functionalization of the AFM's metal tip by picking up CO as previously described for STM by Bartels *et al.*<sup>12</sup> improved the resolution profoundly. The inertness of the oxygen termination of a CO molecule is important for accessing the repulsive regime and for achieving high resolution. Mohn *et al.* found that functionalization of metal tips with inert gases also provides inert tips that allow us to probe the repulsive regime.<sup>166</sup> This beautiful image of pentacene was followed by the detection of the bond order in a C<sub>60</sub> molecule<sup>97</sup> shown in Figs. 50(b) and 50(c). Bonds that are part of two hexagons, labeled h, are of greater bond order than bonds that are part of a pentagon and a hexagon, labeled p. At medium tip height in Fig. 50(c), bonds appear with different brightness, with bonds of greater bond order appearing brighter. At small tip heights in Fig. 50(d), bonds appear with different apparent lengths, with bonds with greater bond order appearing shorter.

Imaging of molecules with a qPlus sensor terminated by a CO tip opened a new field that is covered in recent overviews by Pavlicek and Gross<sup>184</sup> and Gross *et al.*<sup>98</sup> Figures 50(e) and 50(f) show breitfussin A, a quite complex molecule. Figure 50(g) shows molecular compounds of heavy oil. For each of the eight different samples investigated on the order of 100, molecules were imaged. A typical molecule is displayed for each mixture. Analysis of the structures found by AFM provided insight into the molecular geometry, aromaticity, types and locations of heterocycles, occurrence, length and connectivity of alkyl chains, and content of archipelago-type architectures. Figure 50(h) shows molecules that undergo a reversible Bergman cyclization. The Br atoms from dibromoanthracene (DBA) are dissociated to form first a radical and then a diradical. The latter can be reversibly switched into a diyne and back by tunneling electrons at  $V > 1.6$  V. With an applied voltage below 1.6 V, the molecule remains stable and can be imaged by AFM (bottom panel, AFM at  $V = 0$  V). A potentially unknown molecule from the deep sea was identified,<sup>96</sup> reaction products of molecules were identified,<sup>42</sup> and more studies of oil compounds that were analyzed at the submolecular level can be found in Refs. 58 and 59.

Imaging works well for flat molecules, but Jascha Repp's group even succeeded in imaging of "butterfly"-shaped dibenzo[a,h]thianthrene (DBTH) molecules that extend in the third dimension,<sup>183</sup> a much harder task. Pavlicek *et al.* showed in this experiment (see Fig. 51) that AFM data reveal the handedness of the molecule, while STM does not. Albrecht *et al.* from the same group identified the conformational response of individual nonplanar molecules.<sup>4</sup>



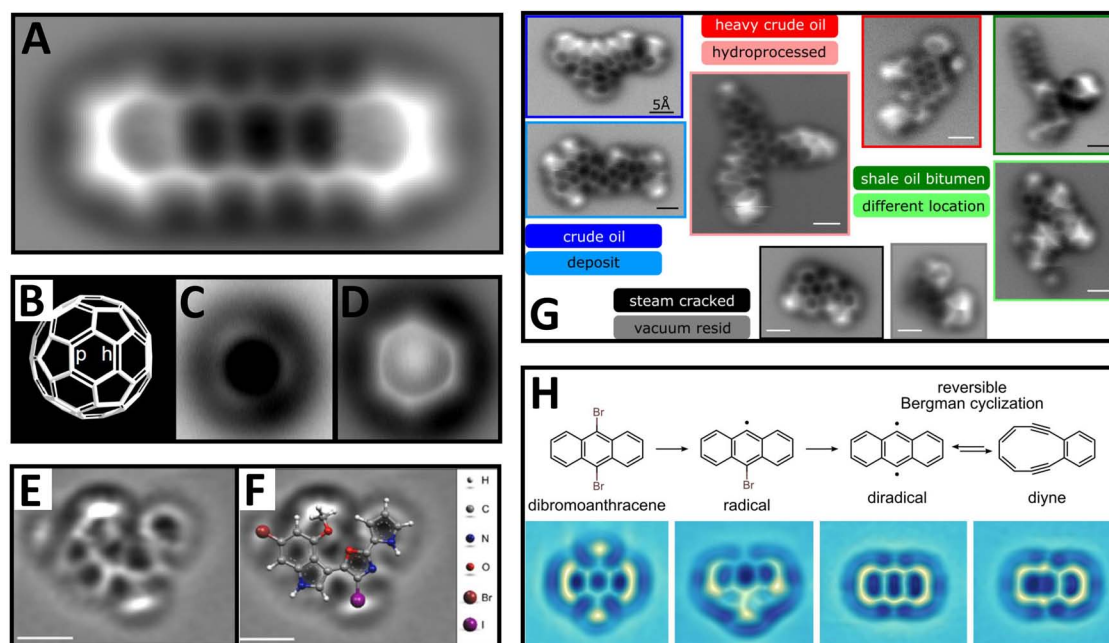


**FIG. 50.** Selection of results from the group of Meyer and Gross *et al.* at IBM Rüschlikon, Switzerland. Molecules imaged with NC-AFM using CO functionalized tips with a qPlus sensor in the constant-height mode. (a) First atomically resolved image of an organic molecule [pentacene on Cu(111)].<sup>95</sup> Reprinted with permission from Gross *et al.*, Science **325**, 1110 (2009). Copyright 2009 AAAS. The color scale corresponds to  $\Delta f = -2$  Hz (white) to  $-7$  Hz (black). Parameters  $f_0 = 23$  kHz,  $k = 1800$  N/m,  $A = 20$  pm. All measurements [(b)–(h)] are recorded with resonance frequencies of  $f_0 \approx 30$  kHz and oscillation amplitudes of  $A \approx 50$  pm. [(b)–(d)] Bond-order discrimination in C<sub>60</sub>.<sup>97</sup> Reprinted with permission from Gross *et al.*, Science **337**, 1326 (2012). Copyright 2012 AAAS. (b) C<sub>60</sub> structural model. [(c) and (d)] Constant-height AFM images of C<sub>60</sub> on Cu(111) for two tip heights, corresponding to estimated differences of 380 pm and 340 pm between the O atom of the CO tip and the plane of the hexagon tile of the C<sub>60</sub> imaged, respectively. [(e) and (f)] AFM image of breifussin A used for its identification and the same AFM image with the identified molecular structure overlaid.<sup>102</sup> Scale bars: 500 pm. Reprinted with permission from Hanssen *et al.*, Angew. Chem., Int. Ed. **51**, 12238 (2012). Copyright 2012 Author(s), licensed under a Creative Commons Attribution 4.0 License.<sup>36</sup> (g) Heavy oil related molecular mixtures of different origins and treatments studied by resolving individual molecules with AFM.<sup>215</sup> Reprinted with permission from Schuler *et al.*, Energy Fuels **31**, 6856 (2017). Copyright 2017 American Chemical Society. (h) Reversible Bergman cyclization.<sup>214</sup> Upper panel: reaction scheme; lower panel: AFM images. Measurements on bilayer NaCl on Cu(111). Reprinted with permission from Schuler *et al.*, Nat. Chem. **8**, 220 (2016). Copyright 2016 Nature/Springer.

The group of Qiu in Beijing was one of the first users of a commercial qPlus based AFM and reported a strange appearance of lines between adjacent 8-hq molecules on surfaces<sup>269</sup> that were interpreted as evidence for hydrogen bonds, shown in Fig. 52. The interpretation of these lines as a possible evidence for hydrogen bonds is a subject of an ongoing fruitful debate; see Refs. 57, 101, 103, and 165.

The possibility to resolve the structure of organic molecules as demonstrated by Gross *et al.* is also very helpful when molecules undergo transformations due to chemical reactions. Crommie and Fisher from the University of Berkeley first imaged the precursors of a chemical reaction, then applied heat to induce a chemical reaction, cooled down for imaging again, and imaged the products in Fig. 53(a). The same group imaged oligomers by combined AFM and scanning tunneling spectroscopy in Fig. 53(b) and even studied the anchoring of molecules to graphene nanoribbons in Fig. 53(c). Molecular reactions were also studied by Albrecht *et al.* using qPlus based AFM.<sup>3</sup>

Figure 54 shows images of graphene nanoribbons imaged with a CO terminated metal tip (a) and a plain metal tip (b).<sup>231</sup> As already apparent in imaging organic molecules, the CO tip

termination has the advantage that CO is very inert, allowing to probe the repulsive regime. The metal tip shows an inverted contrast; i.e., attraction between C atoms and the metallic tip atom prevails. The edge of the nanoribbon exerts strong attractive forces to the metal tip—this is much less pronounced for CO terminated tips. More data on using the qPlus sensor to study graphene and graphene nanoribbons from this group<sup>28,132,244</sup> and other researchers are available in the literature.<sup>138,142,147,202,222</sup> Schwarz *et al.* studied the structure of hexagonal BN on Cu(111) using a combination of qPlus AFM and X-ray standing waves.<sup>216</sup>

The group of Jelinek in Prague is also an early adaptor of the qPlus AFM technique. Figure 55(a) from this group shows simultaneously recorded STM, AFM, and inelastic tunneling spectroscopy (IETS) data of iron-phthalocyanine (FePc) on Au(111).<sup>39</sup> Figure 55(b) shows FePc molecules on nitrogen doped graphene by combined STM/AFM/IETS.<sup>40</sup> Figure 55(c) focusses on a single substitutional nitrogen dopant in graphene on silicon carbide.<sup>40</sup> Figure 55(d) displays self-assembled triple(phthalocyaninato)terbium (III) (Tb<sub>2</sub>Pc<sub>3</sub>) molecules on a Ag(111) surface.<sup>109</sup>

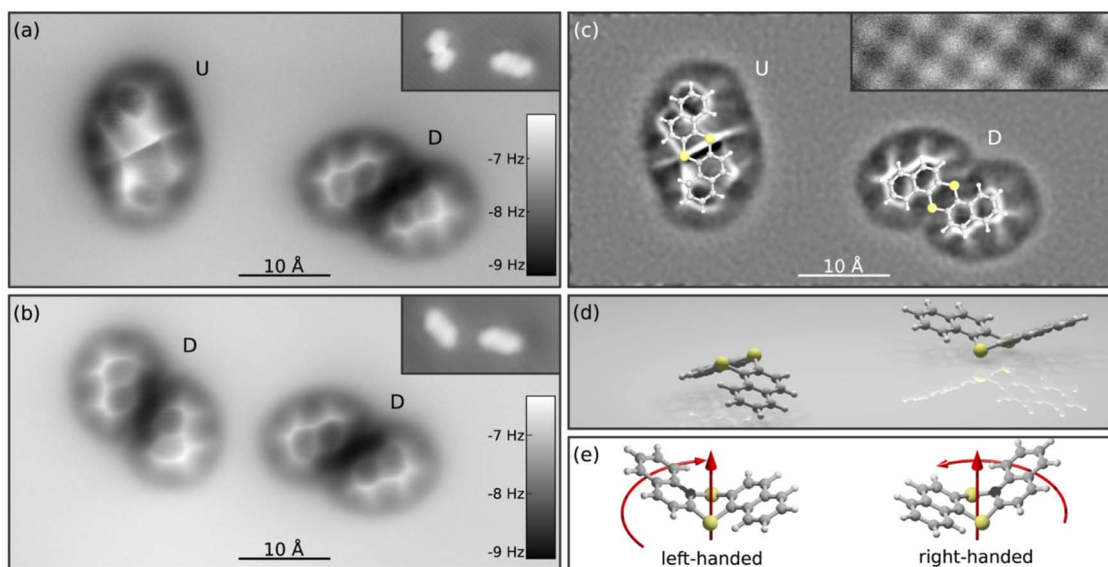


**FIG. 51.** AFM measurements on dibenzo[a,h]thianthrene (DBTH) on two monolayers of NaCl(2ML)/Cu(111) with a CO-functionalized tip.<sup>183</sup> (a) Constant-height AFM image. Imaging parameters: oscillation amplitude  $A = 50$  pm,  $V = 0$  V,  $\Delta z = 0$  pm.  $\Delta z$  corresponds to a distance decrease with respect to an STM set point of  $I = 0.5$  pA,  $V = 0.4$  V above the clean NaCl(2ML)/Cu(111). (b) Image of the same area as in (a) after both molecules changed their adsorption position  $A = 50$  pm,  $V = 0$  V,  $\Delta z = 10$  pm. Insets in (a) and (b) show constant-current STM images of the same frame. Panel (c) represents the curvature of the image in (a) obtained by calculating the Laplacian. Molecular models (drawn to scale) for U and D are overlaid as a guide to the eye; the slightly larger appearance of molecules has been discussed previously.<sup>29</sup> The inset shows an atomically resolved NaCl lattice. (d) Model representing molecules in U and D configuration on a surface. (e) Model depicting chiral enantiomers of the free molecule. Reprinted with permission from Pavlicek *et al.*, Phys. Rev. Lett. **108**, 086101 (2012). Copyright 2012 The American Physical Society.

The group of Tautz at the Forschungszentrum Jülich was also quite an early user of the qPlus sensor. Figure 56 shows three central fields of their study consisting of controlled pick up of large molecules from surfaces (a), the utilization of molecules attached to the tip as sensitive probes (b), and the controlled deposition of vertical molecules that can act as controlled emitters of electrons. Their study<sup>236</sup> shows in Fig. 56(a) how a PTCDA molecule (see figure caption) is peeled off a metal surface. The forces needed to peel off the molecule were quite constant as demonstrated by 226 traces in Fig. 56(a) middle and a 2D histogram of 226  $\Delta f(z)$  traces.<sup>247,248</sup> Fitting  $\Delta f(z)$  with a molecular mechanics model reveals the evolution of the junction geometry and helps quantify long-range van der Waals<sup>249</sup> as well as the short range interactions acting between

the molecule and the surface.<sup>247</sup> Figure 56(b) illustrates scanning quantum dot microscopy (SQDM)—a tool for the nanoscale imaging of electrostatic potential  $\Phi$  where a Kelvin parabola is recorded at a specific spot on the sample, and characteristic dips occur at a voltage  $V^-$  corresponding to electron removal and at voltage  $V^+$  when adding an electron. The molecule peeled off the surface remains hanging on the tip, acting as a quantum dot (QD) that can be charged with single electron precision if a sufficient bias is applied to the tip-surface junction.<sup>67,237,250</sup> The electrostatic potential is then given by  $\Phi \propto -V^-/(V^+ - V^-)$  [see the center part of Fig. 56(b) and caption]. As an application, the quadrupole potential of a flat-lying PTCDA molecule probed at a distance of  $17$  Å from the Ag(111) surface is depicted in the right part of Fig. 56(b).<sup>67,250</sup>

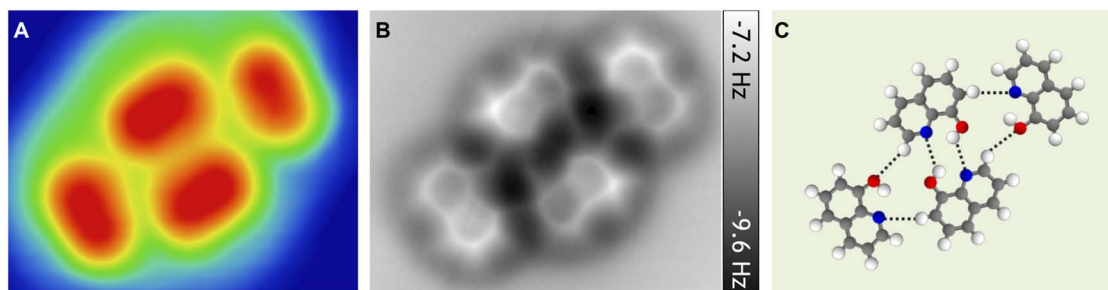


**FIG. 52.** STM and AFM measurements of 8-hydroxyquinoline (8-hq) assembled clusters on Cu(111).<sup>269</sup> (a) Constant-current STM image ( $2.5 \times 2$  nm<sup>2</sup>,  $V = -100$  mV,  $I = 100$  pA). (b) Constant-height frequency shift image ( $2.5 \times 2$  nm<sup>2</sup>,  $V = 0$  V,  $A = 100$  pm,  $f_0 = 27.0$  kHz,  $k = 1800$  N/m). (c) The corresponding structure model. The dashed lines refer to the intermolecular H-bonds. Reprinted with permission from X. Qiu. Copyright Xiaohui Qiu, Beijing.

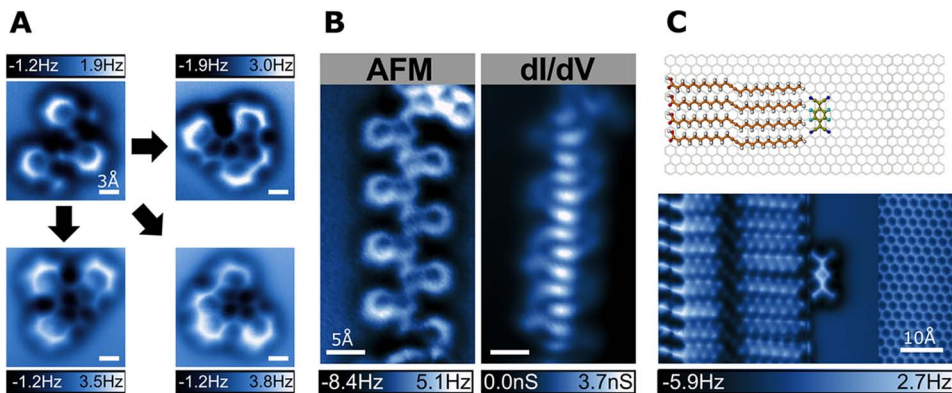


**FIG. 53.** Selection of results from the groups of Crommie and Fischer *et al.*, Berkeley. (a) AFM image of single-molecule reactant and products.<sup>42</sup> (b) Local chemical and electronic structure of an oligomer.<sup>201</sup> (c) Tetrafluoro-tetracyanoquinodimethane ( $F_4TCNQ$ ) anchored by 10,12-pentacosadiynoic acid (PCDA) molecules on the graphene surface.<sup>264</sup> Parameters for all data  $k = 1800$  N/m,  $A = 60$  pm,  $f_0 = 29\,730$  Hz. Reprinted with permission from M. F. Crommie. Copyright M. F. Crommie, University of Berkeley, USA.

In Fig. 56(c), it is demonstrated how moving the tip along a special 3D trajectory<sup>66,154,155</sup> enables a single PTCTA molecule to be erected onto a pedestal of two silver adatoms into a stable, vertically standing configuration.<sup>55</sup> In the middle of Fig. 56(c), it is demonstrated that a standing PTCTA also acts as a quantum dot (QD): An electron can be added to the QD if a large negative bias is applied to the surface. Due to field-emission, this electron leaves the QD quickly and moves toward the tip. The right part of Fig. 56(c) shows the intensity map of the field-emission current imaged 7 nm away from the surface, caused by the quantum-mechanical interference of single electron trajectories.

A vast array of applications of qPlus based AFM is found in the structural arrangement and reactions of molecules on surfaces; see, e.g., Refs. 27, 107, 182, and 251.

### 10. Van der Waals forces

The van der Waals interaction is an important force in nature that acts between all matter. For noble gases, it is the

most important bonding mechanism. Kawai *et al.* have studied the van der Waals interaction between a Xe terminated AFM tip and Ar, Kr, and Xe surface atoms in Fig. 57(a).<sup>139</sup> They also studied the sliding forces of a graphene nanoribbon on Au(111) in Fig. 57(b)<sup>140</sup> as well as boron- and nitrogen-doped graphene nanoribbons in Fig. 57(c).<sup>138,142</sup> Figure 57(d) shows the AFM images of the smallest atom, hydrogen—the upright standing propellane molecules are terminated by H-atoms.<sup>141</sup>

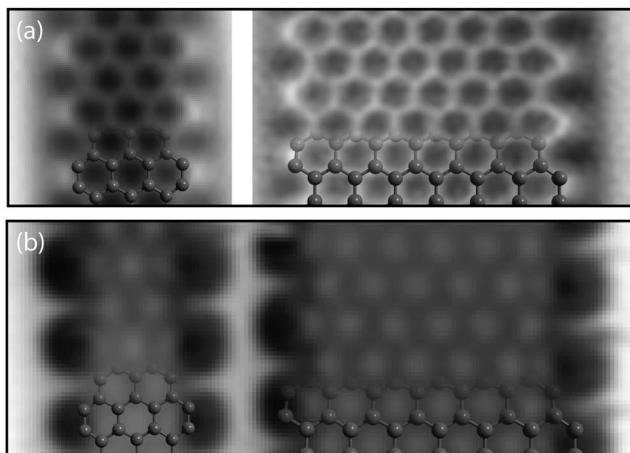


**FIG. 54.** AFM measurements of graphene nanoribbons. (a) Graphene nanoribbons that are 3 and 6 rings wide imaged with a qPlus sensor with a CO tip termination. (b) Same nanoribbons imaged with a metal tip.<sup>231</sup> Reprinted with permission from I. Swart. Copyright Ingmar Swart, University of Utrecht.

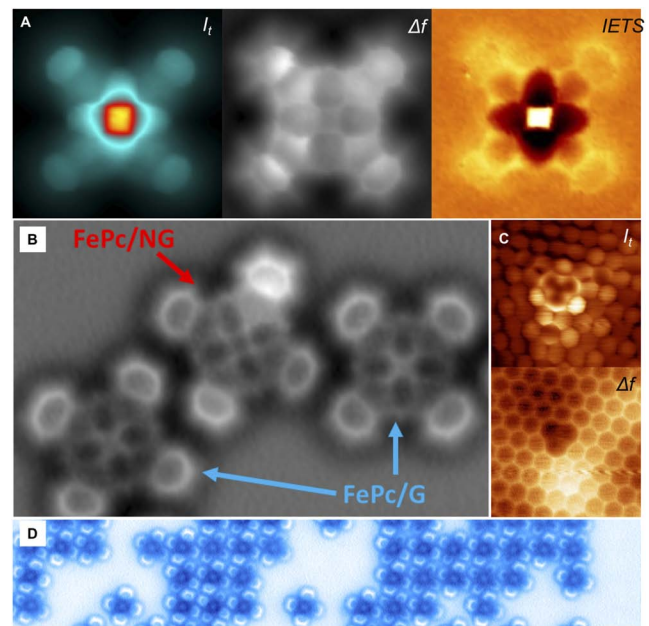


**FIG. 55.** (a) Simultaneously acquired STM/AFM/IETS constant-height image of iron phthalocyanine (FePc) on an Au(111) surface. Lock-in technique with a modulation of 3 mV at a frequency of 963 Hz; see Ref. 39 for details. (b) Constant-height AFM image of FePc molecules deposited on nitrogen doped graphene.<sup>40</sup> (c) Constant-height simultaneous STM/AFM images of a single substitutional nitrogen dopant in graphene grown on the SiC(0001) surface.<sup>40</sup> (d) Constant-height AFM image of self-assembled triple(phthalocyaninato)terbium (III) ( $Tb_2Pc_3$ ) molecules on a Ag(111) surface.<sup>109</sup> Parameters for all data  $f_0 = 30$  kHz,  $A = 50$  pm,  $k = 1800$  N/m. Reprinted with permission from P. Jelinek. Copyright Pavel Jelinek, Czech Institute of Physics, Prague, Czech Republic.



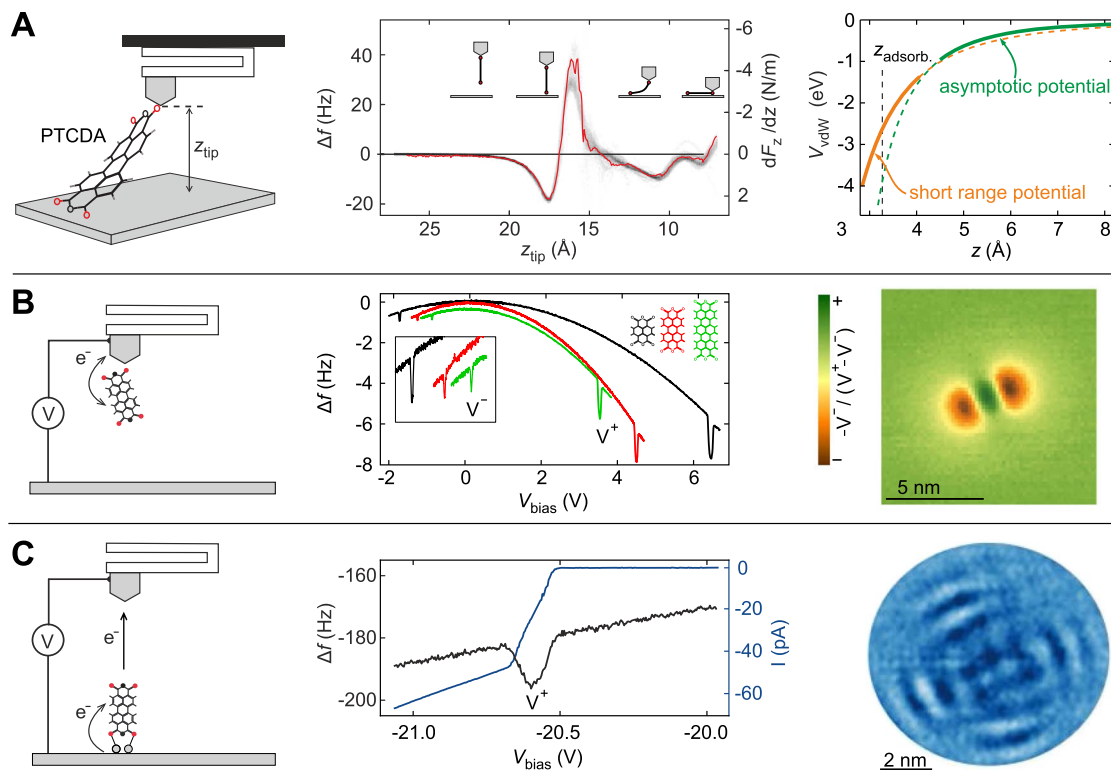


**FIG. 56.** Molecular manipulation and scanning quantum dot microscopy with a qPlus sensor in the groups of Tautz and Temirov, FZ Jülich, Germany.<sup>66,237,250</sup> (a) Left: A bond between the tip of the qPlus sensor and one of the carbonyl oxygens of PTCDA (3,4,9,10-perylene tetracarboxylic acid dianhydride) can be used to peel the molecule off a metal surface.<sup>236</sup> Middle:  $\Delta f(z)$  can be measured reliably during the peeling.<sup>63</sup> An exemplary single curve is shown in red. Right: Fitting  $\Delta f(z)$  with a molecular mechanics model.<sup>249</sup> (b) Left: The molecule attached to the tip acts as a quantum dot (QD) that can be charged with single electron precision.<sup>67,250</sup> Middle: QD charging causes characteristic dips in the Kelvin parabola: the dip at  $V^-$  is caused by a removal, and the dip at  $V^+$  is caused by an addition of one electron to the QD.  $V^\pm(z)$  reflect both the properties of the tip-surface junction and the type of molecular QD.<sup>237</sup> Right: Lateral mapping of  $V^\pm$  enables scanning quantum dot microscopy (SQDM).<sup>66,154,155</sup> (c) Left: It is possible to erect a single PTCDA molecule onto a pedestal of two silver adatoms into a stable, vertically standing configuration.<sup>55</sup> Middle: Standing PTCDA also acts as a QD: An electron can be added to the QD if a large negative bias is applied to the surface. Right: The intensity of the field-emission current imaged 7 nm away from the surface reveals the quantum-mechanical interference of single electron trajectories. Reprinted with permission from R. Temirov. Copyright Stefan Tautz, Ruslan Temirov, Forschungszentrum Jülich, Germany.

## 11. Silicon

The imaging of the Si(111)-(7 × 7) reconstruction has been an important benchmark test of the AFM utility as a tool for surface science.<sup>88</sup> The first result [see Fig. 58(a)] was obtained with a self-sensing silicon cantilever<sup>71</sup> in 1995, originating from covalent bonding between tip and sample.<sup>187</sup> Much nicer results that even showed evidence for the presence of the rest atoms were obtained later at low temperatures in 2000<sup>150,151</sup> and at room temperature with very sharp Si cantilevers.<sup>50</sup>

The first successful imaging of Si with the qPlus sensor was obtained in 2000 at room temperature,<sup>82</sup> showing even strong indications for subatomic resolution where the Si adatoms repeatedly image two tip orbitals that originate in one Si tip atom [see Fig. 58(b)].

Low temperature qPlus AFM with CO terminated tips that proved so successful in imaging organic molecules<sup>95</sup> has also helped obtain clearer images of silicon. Figure 58(c) shows an image of silicon, obtained with a CO terminated tip,

featuring very small local maxima for the twelve adatoms and even clear local maxima for the six rest atoms in each unit cell.<sup>53</sup> The group of Moriarty at the University of Nottingham has studied the switching of the dimer buckling structure on Si(100) shown in Fig. 59(a) via direct mechano-chemical interaction with the apex of a scanning probe tip. The insets in Fig. 59(b) show the position of the atoms in the tip-sample junction at each stage of the manipulation. In Fig. 59(c), reverse imaging of a C<sub>60</sub> molecule attached to the scanning probe tip occurs similar to the imaging process in Fig. 58(b) or in the comparison of COFI and Si adatom imaging in Ref. 258. Figure 59(d) shows the measurement and calculation of the chemical force responsible for sub-molecular atomic contrast. Figures 59(e) and 59(f) describe the interaction of C<sub>60</sub> terminated tips with C<sub>60</sub> molecules on the surface.

The group of Wolkow<sup>126,196</sup> worked on silicon based atomic logic circuits on the atomic scale and used a low temperature qPlus based microscope. Figure 60 shows the construction of an OR gate on a silicon surface by dangling



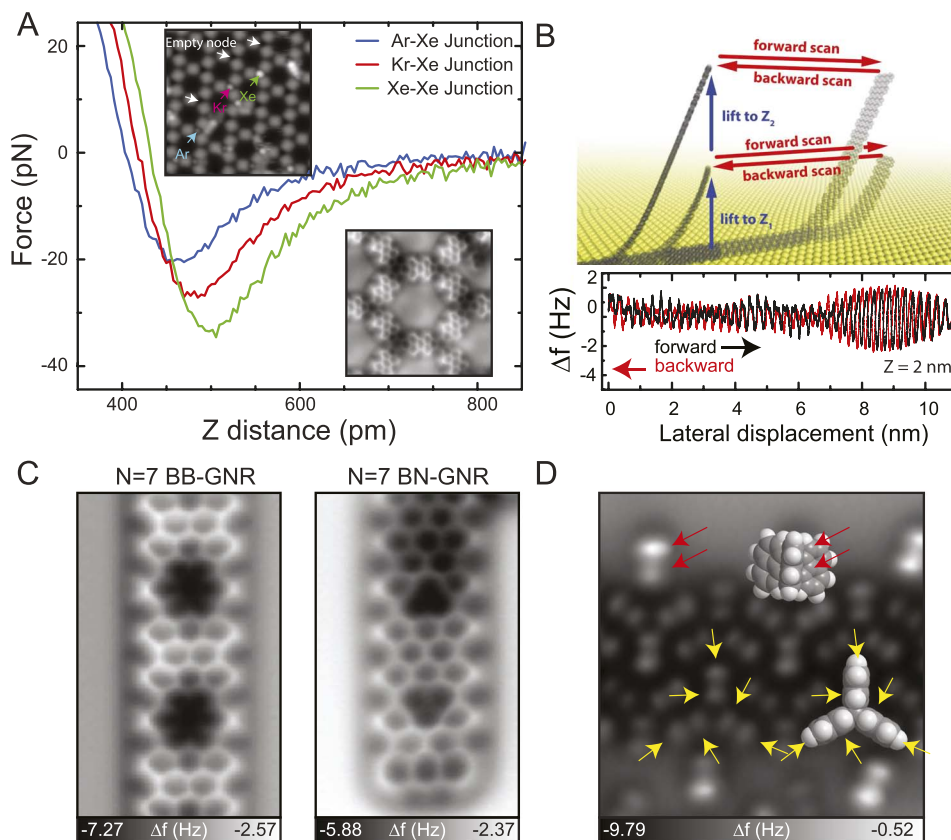


**FIG. 57.** Some examples of AFM experiments from the group of Meyer, University of Basel, Switzerland. (a) Van der Waals force measurement of Ar-Xe, Kr-Xe, and Xe-Xe junctions with a Xe terminated tip. Insets show the STM topography (top) of a two-dimensional metal-organic framework with various rare gas atoms and AFM image (bottom) taken with a CO terminated tip; see Ref. 139 for details. (b) Friction measurement via the frequency shift accompanying the lateral motion of the graphene nanoribbon on Au(111).<sup>140</sup> (c) AFM images of boron-doped (left) and boron-nitrogen doped graphene nanoribbons (right); see Refs. 138 and 142. (d) AFM image of hydrogen atoms of propellane molecules; see Ref. 141. Measurement parameters:  $A = 38$  pm,  $f = 23\,064$  Hz. Inset:  $A = 60$  pm in (a).  $A = 38$  pm,  $f = 24\,733.7$  Hz in (b).  $A = 38$  pm,  $f = 24\,764.3$  Hz (left) and  $A = 60$  pm,  $f = 24\,805.5$  Hz (right) of (c).  $A = 60$  pm,  $f = 23\,128.6$  Hz in (d). Reprinted with permission from E. Meyer. Copyright E. Meyer, University of Basel, Switzerland.

bonds, i.e., unsatisfied bonds that are created by removing the H atoms from the otherwise hydrogen-terminated silicon surface with the application of a voltage pulse. The AFM signal provides the electron location as shown in the second row of Fig. 60.<sup>126</sup> Yamazaki and Shiotari *et al.* have also studied atomic switches with qPlus based detection (see Refs. 272 and 273).

## 12. Topological insulators

Topological insulators are materials that conduct electrical currents on the surface but not inside. Spin and momentum are locked in the topologically protected conductive

surface states.<sup>104</sup> The surface of the topological insulator  $\text{TiBiSe}_2$  has been resolved atomically with the qPlus sensor in 2015.<sup>192</sup> The surface was imaged before by STM, displaying only wormlike structures that did not reveal the true structure of the cleaved surface. The AFM data shown in Fig. 61 indicate that the layered material cleaves along TI planes, leaving approximately half of the TI atoms on either cleavage plane.

## 13. Atomically resolved damping

As outlined in Subsection II D, FM-AFM is very sensitive to local dissipation, i.e., hysteresis in the force versus

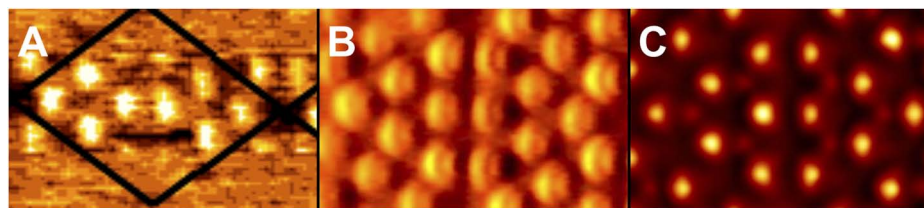


**FIG. 58.** Evolution of imaging Si(111)-(7 × 7) by AFM. (a) First result, obtained with a piezoresistive Si cantilever in 1995.<sup>71</sup> The adatoms appear quite noisy and a tip change is apparent. (b) First result obtained by using a qPlus sensor in 2000.<sup>82</sup> Noise is much lower, and the tip is stable; however, the Si adatoms image the tip of the AFM showing subatomic contrast. (c) Resolving rest atoms with a qPlus sensor with a CO tip from 2015.<sup>55</sup> Here, the diameter of the adatom images is much smaller, and even the rest atoms appear as local maxima, although they are located more than 100 pm deeper than the adatoms. Reprinted with permission from F. J. Giessibl, *Science* **267**, 68 (1995). Copyright 1995 AAAS (a), Reprinted with permission from F. J. Giessibl, *Science* **289**, 422 (2000). Copyright 2000 AAAS (b), Reprinted with permission from Emmrich *et al.*, *Science* **348**, 308 (2015). Copyright 1995 AAAS (c).

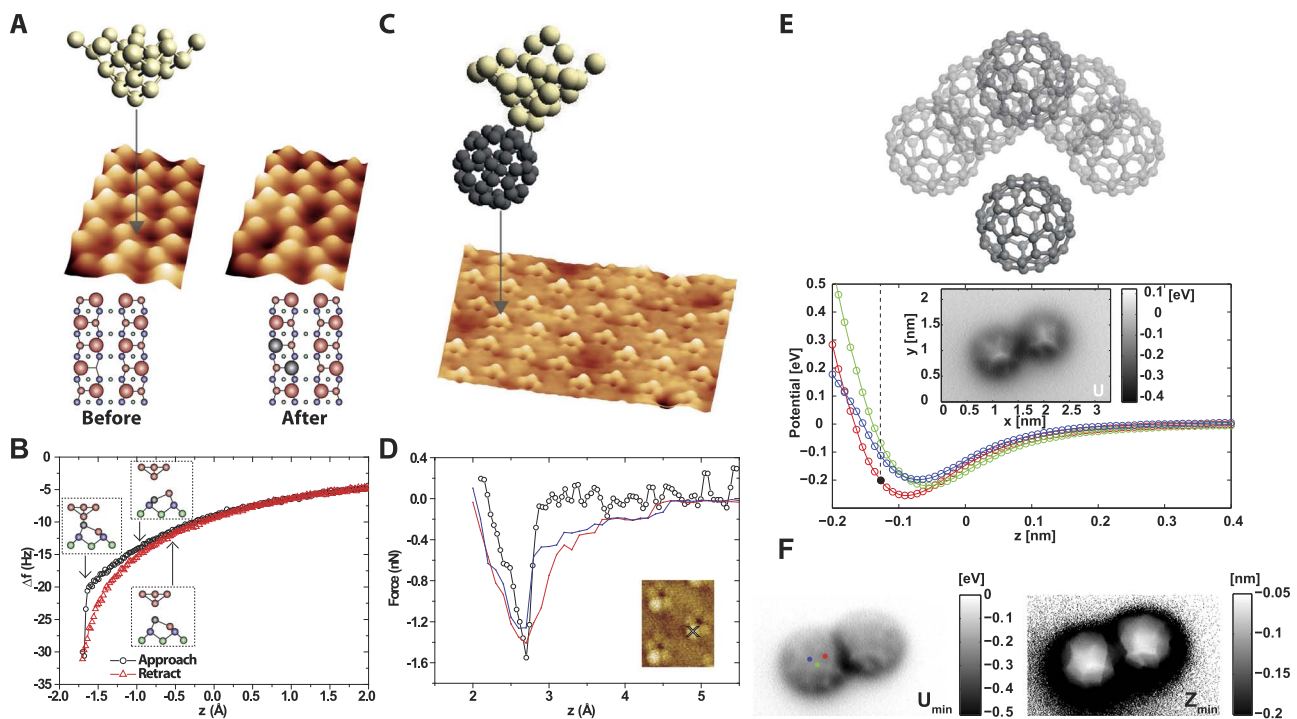


**FIG. 59.** Results from Moriarty's group at the University of Nottingham, UK. (a) Manipulation of the dimer buckling structure on the Si(100) surface. Left image: constant  $\Delta f$  image before manipulation and position of tip during manipulation. Right image: the same region after manipulation. Schematic of the surface structure below. (b)  $\Delta f(z)$  curves showing  $\Delta f$  curves during the tip approach (black circles) and retraction (red triangles). Experimental parameters:  $A = 250$  pm,  $\Delta f = -9.1$  Hz. (c) Constant  $\Delta f$  image showing "inverse imaging" on the Si(111)- $7 \times 7$  surface of a  $C_{60}$  molecule mounted on the scanning probe tip.<sup>232,233</sup> Pentagon-down orientation, where a maximum in the tip-sample interaction is observed for each atom in the pentagonal face of the  $C_{60}$  molecule. (d) Experimental and calculated force spectroscopy for a  $C_{60}$  terminated tip and Si(111). A comparison of an experimentally determined  $F(z)$  curve (open circles) with force-displacement relationships calculated using DFT for a silicon adatom directly below a carbon atom (red line) and a C-C single bond (blue line) at the position shown in the inset. Experimental parameters:  $A = 200$  pm,  $\Delta f = -22.3$  Hz. (e) (Top) Experimental 3D mapping of variation in potential between  $C_{60}$  molecules at different positions. (Below) Graph of representative site-specific intermolecular potentials at different tip-sample positions and (inset) experimental constant-height potential image taken at  $z \approx -0.13$  nm indicated by the dotted line.<sup>234</sup> (f) x-y maps of variation in minimum of intermolecular potential ( $U_{min}$ ) and height of minimum in intermolecular potential ( $Z_{min}$ ) extracted from 3D potential. The positions of the curves shown in E are marked. Experimental parameters:  $A = 110$  pm. Common parameters of all subfigures:  $f_0 \approx 24$  kHz,  $k \approx 1800$  N/m,  $V_{bias} = 0$  V.<sup>34,234</sup> Reprinted with permission from P. Moriarty and A. Sweetman. Copyright Philip Moriarty and Adam Sweetman, University of Nottingham, United Kingdom.

distance curve. Such a hysteresis occurs in particular over loosely bonded atoms. The topological insulator TlBiSe<sub>2</sub> consists of stacked layers. Cleaving occurs preferentially on Tl layers, leaving two new surfaces with about a 50% occupation of the Tl sites, as shown in Fig. 61. At room temperature, these Tl atoms are quite mobile such that the surface appears to be flat (Fig. 5 in Ref. 192). While these Tl atoms freeze out at 4 K to form wormlike structures, the atoms can still be deflected laterally as the vibrating tip approaches it. These deflections equilibrate when the tip oscillates away from the Tl adatoms, causing moderate dissipation of up to about 20 meV per oscillation cycle. In the first proposal on highly spatially resolved dissipation measurements,<sup>41</sup> induced electric currents were discussed as the origin of damping. Apparently, this is not the case in Fig. 62, as voltage and current are 20 times larger in the lower row compared to the top row, although the measured dissipation plotted in the right column is quite similar.

#### 14. Imaging involving superconductors

Jorge Hirsch proposed an experiment regarding screening of charges by a superconductor,<sup>116</sup> where the Thomas-Fermi screening length that shields charged impurities in a metal with its typical range of less than 100 pm would increase to the London penetration depth in a superconducting transition. We have attempted to check this effect and so far could not confirm it<sup>188</sup> because the difference in frequency shift versus distance curves in Fig. 63 between normal and superconductive tips is not larger than the experimental errors. Possibly, the density of normal conductive electrons was still high to observe a clear effect at the minimal temperature of 2.4 K we could reach so far. However, we could demonstrate that the tip of a qPlus sensor is colder than the transition temperature of niobium (9.5 K for bulk  $T_c$ ) and was indeed superconductive. An analysis of the  $dI/dV$ -spectrum (see the inset in Fig. 63) shows that the tip is

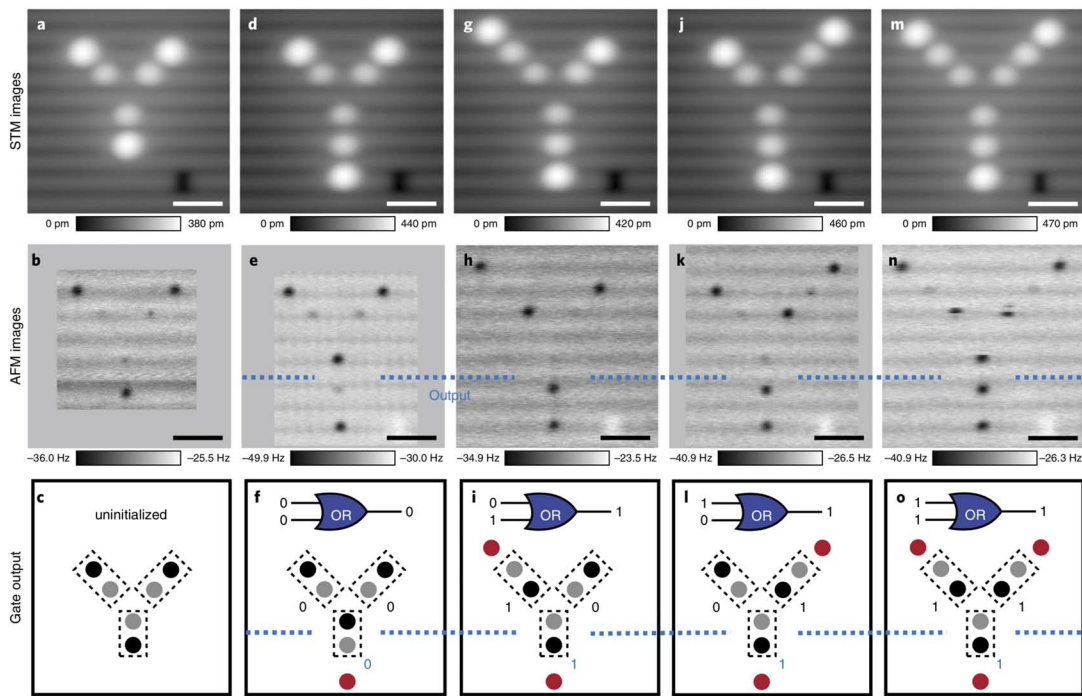


**FIG. 60.** Silicon based logic on the atomic scale from the group of Wolkow, University of Alberta, Edmonton, Canada. OR gate constructed of dangling bonds. First row: Constant-current filled state STM images ( $V = -1.8$  V,  $I = 50$  pA) of the OR gate in various actuation states. Second row: corresponding constant-height  $\Delta f$  images ( $V = 0$  V,  $z_{rel} = -350$  pm) of the gate, displaying electron location as the dark depressions, with the output DB marked in red. Bottom row: The complete truth table of an OR gate with models for the four distinct outputs corresponding to the gates displayed vertically above them in rows one and two. Scale bars are 2 nm. Reprinted with permission from Huff *et al.*, Nat. Electron. 1, 636 (2018). Copyright 2018 Nature.

at the same temperature as the sample, within fractions of 1 K. To our knowledge, this is the first demonstration of a superconductive tip for an operating atomic force microscope.

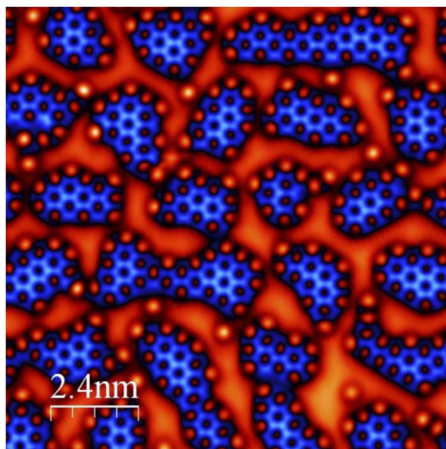


**FIG. 61.** Constant-height AFM image of a cleaved surface of the topological insulator TlBiSe<sub>2</sub> recorded at  $T = 4.4$  K.<sup>192</sup> Only about half the lattice sites are occupied by TI atoms, and the remaining half of TI atoms is found on the other part of the cleaved crystal. Imaging parameters:  $f_0 = 26\,666$  Hz,  $k = 1800$  N/m,  $V_{bias} = 10$  mV,  $\Delta f$  ranges from  $-60$  Hz (dark) to  $-10$  Hz (bright).

## 15. Water

Water is one of the smallest molecules and its chevron-like structure and permanent dipole moment leads to fascinating structural properties. Resolving its structure and adsorption geometries is an interesting challenge for AFM. The group of Sugimoto in Japan has imaged (Fig. 64) a pentagonal chain of water molecules on a Cu(110) surface, where the AFM channel on the right side shows much more features than the STM channel in the center.<sup>223</sup> Ying Jiang's group from Beijing, China, has imaged water dimers [Fig. 65(a)], tetramers [Fig. 65(b)],<sup>185</sup> and the ion hydrate  $\text{Na}^+ \cdot 4\text{D}_2\text{O}$  [Fig. 65(c)] adsorbed on the NaCl(001) surface<sup>186</sup> using a CO terminated metal tip. The submolecular features originate from the high-order electrostatic force acting between the quadrupole-like CO-tip and the strongly polar water molecules. The crooked depressions (see dashed curves) and the bright protrusions (see white arrows) in the AFM image arise from the positively charged hydrogen and the negatively charged oxygen, respectively.

## 16. Lateral force microscopy and friction measurements

While lateral forces can be derived when the tip-sample potential energy landscape is available, as possible in low-temperature force spectroscopy used in measuring force needed to move an atom,<sup>239</sup> a direct measurement is often



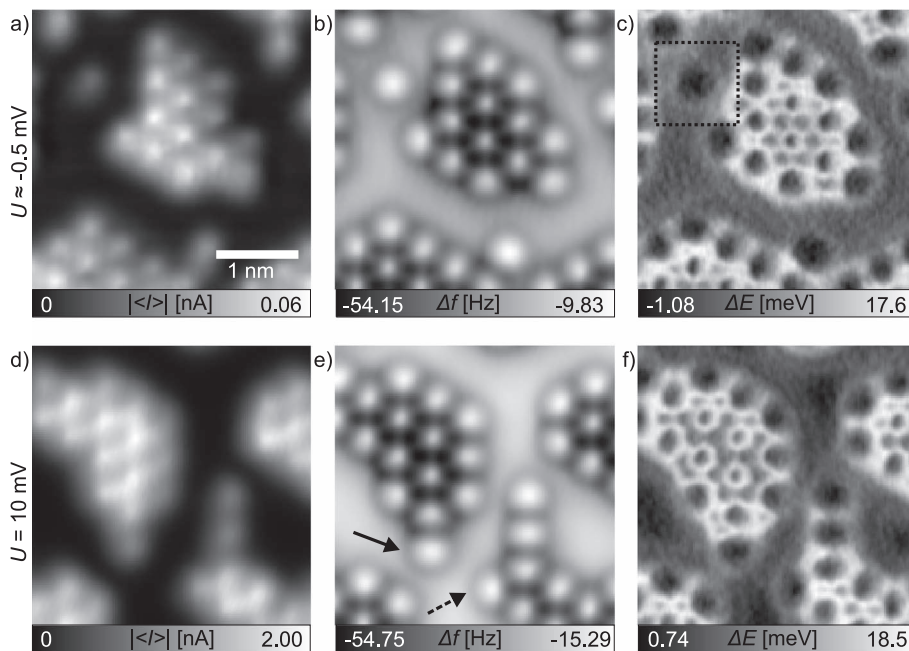


**FIG. 62.** Tunneling current (left), frequency shift (center), and tip-sample dissipation per cycle (right) of a cleaved surface of the topological insulator TlBiSe<sub>2</sub>. There is about a 50% occupation of the TI sites on the surface similar to Fig. 61. Dissipation shows a strong minimum above the TI atoms. Parameters: a qPlus sensor with  $f_0 = 26\,666.0$  Hz,  $k = 1800$  N/m,  $A = 50$  pm,  $Q = 28\,140$ .<sup>193</sup>

more elegant. The qPlus sensor can easily be rotated by 90°, and lateral forces can be measured with atomic resolution, as first shown in Ref. 85. At room temperature, the dependence of lateral forces on the orientation of dimer rows in Si(001) surfaces<sup>260</sup> was determined, as outlined in Fig. 38. The precision of these measurements can be increased dramatically by performing the experiments at low temperatures. The

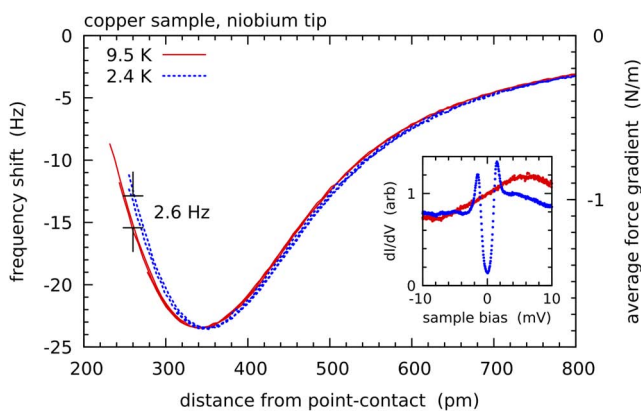


**FIG. 63.** Frequency shift spectra at two different temperatures on Cu(111), acquired with a superconductive Nb tip.<sup>188</sup> At  $T = 2.4$  K, the tip superconducts, as shown by the  $dI/dV$  spectroscopy of the superconducting gap (inset). These spectra are acquired on the same point on the surface, and multiple measurements are shown. The  $dI/dV$ -spectra are acquired at a tunneling set point  $V = -20$  mV and  $I = 200$  pA with a modulation voltage  $V_m = 200$   $\mu$ V<sub>pk</sub> at  $f_m = 590$  Hz. Parameters: a qPlus sensor with  $f_0 = 47\,388.0$  Hz,  $k = 1800$  N/m,  $A = 100$  pm,  $Q = 250\,000 - 540\,000$ . Reprinted with permission from A. Peronio and F. J. Giessibl, Phys. Rev. B **94**, 094503 (2016). Copyright 2016 The American Physical Society.

very weak interaction between one CO molecule attached to a tip and the other to a sample has been measured by lateral force microscopy;<sup>261</sup> see Fig. 66. The interaction of two CO molecules is on the order of a few milli-electron volts—a few orders of magnitude weaker than the interactions between atoms that form covalent bonds. A precise measurement of such small interactions is challenging, in particular, the separation from long-range van der Waals background forces.<sup>230</sup> The great advantage of lateral force microscopy is that the van der Waals interaction between a tip and a flat sample acts only in the  $z$ -direction. Therefore, even weak lateral forces are not concealed by a van der Waals background. The measurement shown in Fig. 66 enabled to determine the lateral stiffness of a CO attached to a tip at 0.24 N/m in agreement with the findings in an algorithm that allows us to correct for the CO-bending distortions that occur when imaging organic molecules.<sup>174</sup> A recent review of LFM can be found in Ref. 262.

## 17. Oxides

Atomic imaging of insulators is one of the key possibilities that were opened up by AFM. Thin oxide films such as titania have been studied by STM for a long time by the group of Diebold<sup>44</sup> and others. Diebold and Setvin *et al.* have started to apply AFM to understand the structural properties of oxides,<sup>220</sup> as shown in Fig. 67. Rutile TiO<sub>2</sub> is one of the most studied model systems in oxide surface science; well-defined surface oxygen vacancies (V<sub>O</sub>) are ideal for investigating defect related surface chemistry; see the structural model in Fig. 67(a). Figure 67(a) shows a structural model of rutile TiO<sub>2</sub>, a model system in the surface science of oxides. Figure 67(b) is a traditionally empty-state STM image, where the V<sub>O</sub>s appear as extra bright spots between rows of five-fold



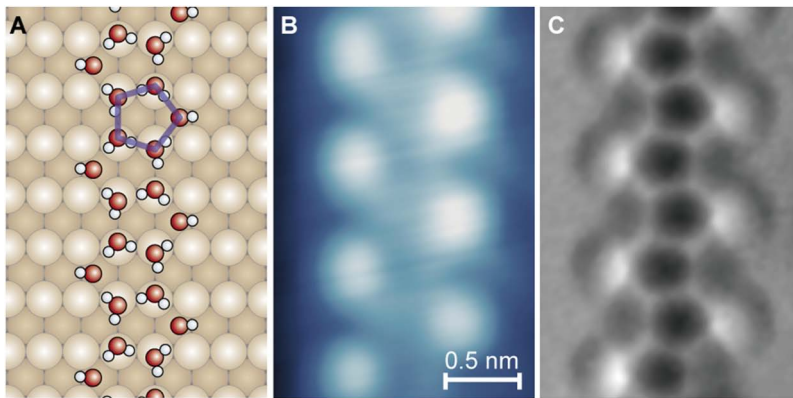


**FIG. 64.** (a) Schematic of the pentagonal water chain on a Cu(110) surface. Red and white spheres represent O atoms and H atoms, respectively. (b) STM topographic image of the chain.  $V_s = 30$  mV,  $I = 20$  pA. (c) Constant-height AFM image of the same chain as (b). The oxygen skeleton is visualized.  $A = 200$  pm,  $f_0 = 20.1$  kHz,  $k = 1800$  N/m; see Ref. 223. Reprinted with permission from Y. Sugimoto. Copyright Yoshiaki Sugimoto, University of Tokyo, Japan.

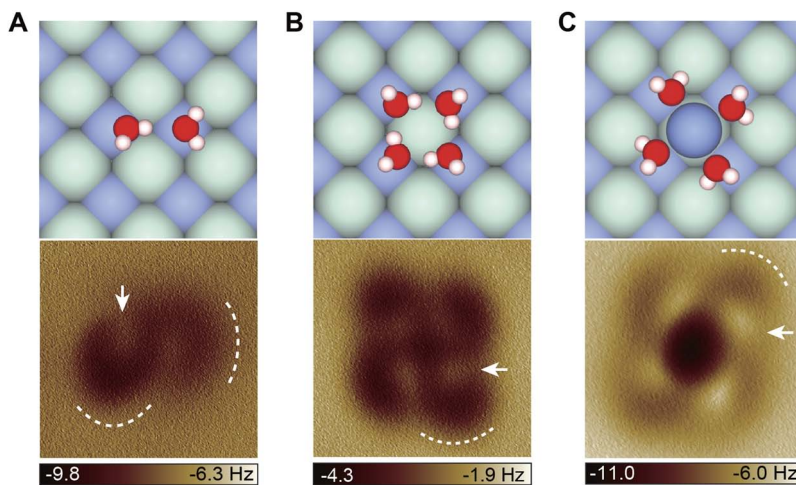


**FIG. 65.** Atomic models (top) and AFM images (bottom) of (a) water dimer, (b) tetramer, and (c) ion hydrate  $\text{Na}^+ \cdot 4\text{D}_2\text{O}$  adsorbed on the NaCl(001) surface acquired with a CO-tip. All the tip heights are 100 pm with reference to the STM set point on the NaCl surface (100 mV, 50 pA). All the oscillation amplitudes are  $A = 100$  pm. Size of the images:  $1.2 \times 1.2$  nm. Parameters of the qPlus sensor: spring constant  $k \approx 1800$  N/m, resonance frequency  $f_0 = 23.7$  kHz, and quality factor  $Q \approx 80\,000$ . H, O, Cl, and Na atoms are denoted as white, red, green, and purple spheres, respectively. See also Refs. 185 and 186 for more details. Reprinted with permission from Y. Jiang. Copyright Ying Jiang, Peking University, China.

coordinated Ti5c atoms. AFM reveals the two-fold =  $\text{O}_{2c}$  atoms shown in Fig. 67(c). The anatase phase of  $\text{TiO}_2$  is shown in Fig. 67(d).

Adsorbed  $\text{O}_2$  appears neutral and singly charged, showing vastly different force spectra in Fig. 67(e). The charge

state can be switched as shown in Fig. 67(f) similar to the experiments by Gross *et al.* on Au adatoms.<sup>94</sup> More recently, this group investigated the polarity compensation mechanisms on the perovskite surface  $\text{KTaO}_3(001)$  with qPlus based AFM.<sup>221</sup> The bottom row in Figs. 67(g)–67(i) shows results from

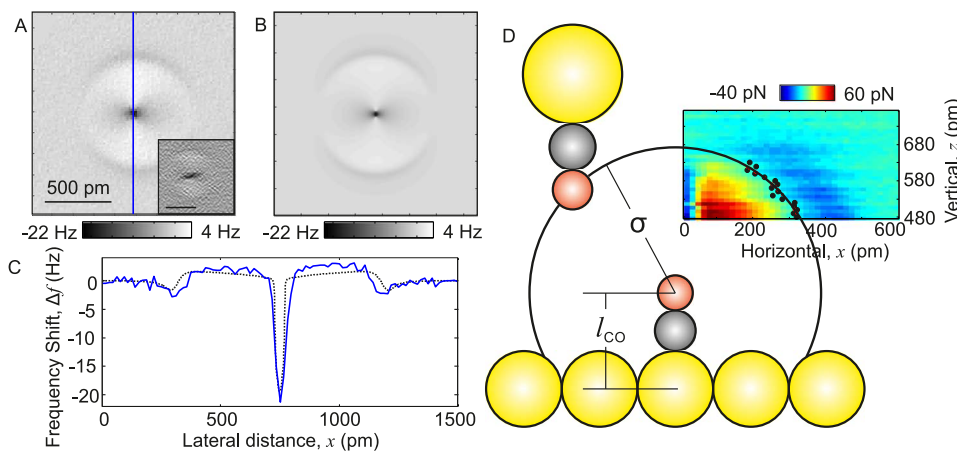


**FIG. 66.** Measuring the interaction energy of two CO molecules by lateral force microscopy.<sup>261</sup> The interaction between the two CO molecules is very small compared to the normal van der Waals forces. Therefore, the lateral force measurement provides greater sensitivity. Reprinted with permission from Weymouth *et al.*, Science **343**, 1120 (2013). Copyright 2013 AAAS.

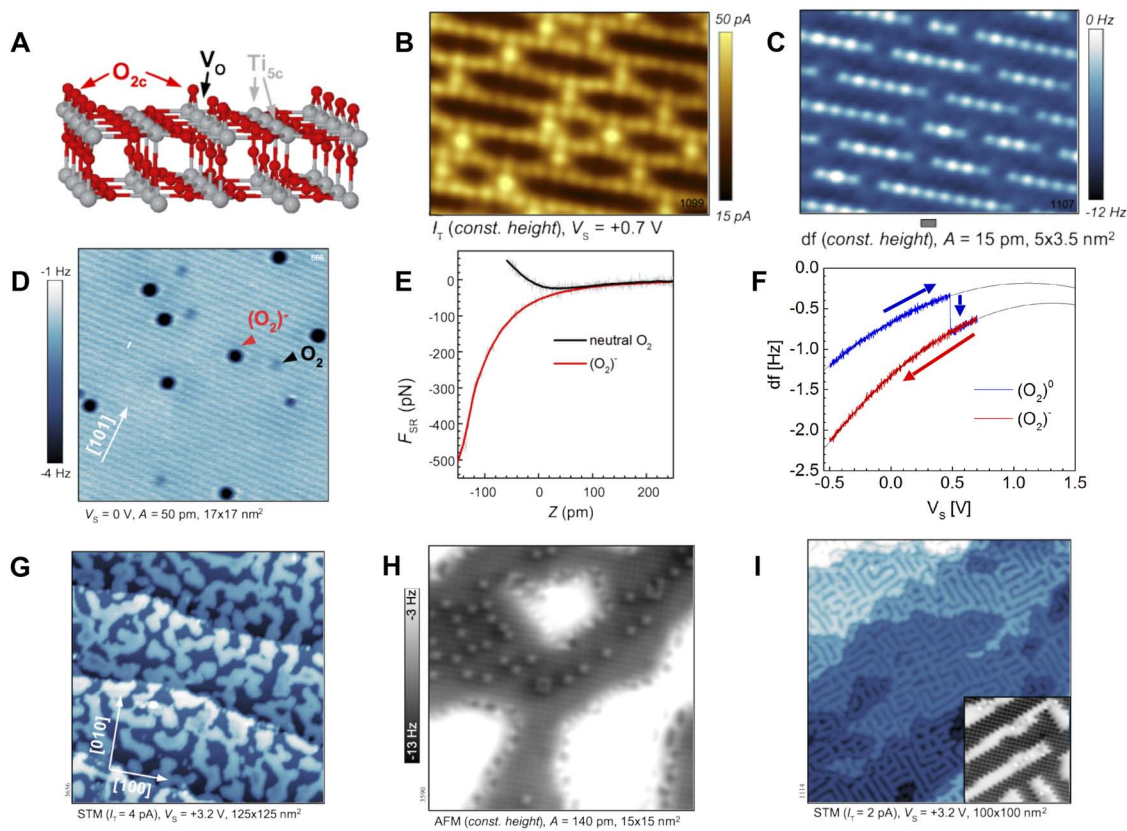


**FIG. 67.** Overview of nc-AFM results on oxides obtained in the group of Diebold in Vienna, Austria. Top row [(a)–(c)]: Rutile  $\text{TiO}_2$  with well-defined surface oxygen vacancies ( $V_O$ ) is a model system for defect related surface chemistry; see atomic model in (a). Traditionally, empty-state STM images are used, where the  $V_O$ s appear as extra bright spots between rows of five-fold coordinated  $\text{Ti}_{5c}$  atoms, as in panel (b). With non-contact AFM in the repulsive mode [(c) on the same area as in (b)], the two-fold  $\text{O}_{2c}$  atoms are apparent, and  $V_O$ s are clearly identified as missing atoms; see Refs. 198, 218, and 219. Middle row [(d)–(f)]: AFM is also an ideal tool to investigate the oxygen surface chemistry on anatase  $\text{TiO}_2(101)$ .<sup>220</sup> Upon exposure to molecular  $\text{O}_2$  at low temperatures, two species are apparent as spots with different contrast in panel (d). In force-distance curves (e), these are identified as neutral and singly charged ( $\text{O}_2^-$ ) species, respectively. By ramping the sample bias voltage  $V_s$ , a neutral  $\text{O}_2$  can be converted into a charged ( $\text{O}_2^-$ ) underneath the tip; see panel (f). The bottom row [(g)–(i)] shows results from  $\text{KTaO}_3(001)$ . Upon cleaving, islands are visible, with steps that have a height of half unit cell (g), identified as KO terraces with an undisturbed  $(1 \times 1)$  structure. Upon gentle heating,  $V_O$ s form at the center of the KO islands (h), and further heating induces a well-defined labyrinth structure (i). Reprinted with permission from U. Diebold. Copyright Ulrike Diebold, Technical University of Vienna, Austria.

a polar perovskite oxide,  $\text{KTaO}_3(001)$ . Upon cleaving, islands are visible, with steps that have a height of half unit cell in Fig. 67(g). With nc-AFM, these are identified as KO terraces with an undisturbed  $(1 \times 1)$  structure. Upon gentle heating,  $V_O$ s form at the center of the KO islands in Fig. 67(h), and further heating induces a well-defined labyrinth structure in Fig. 67(i). These and other features are explained as mechanisms for compensating the polarity in the system.<sup>221</sup>

The group of Schwarz in Yale looked at surface oxidized  $\text{Cu}(100)$  samples in Fig. 68(a). The total force contrast is 22 pN, and atomic corrugation is clearly observable on the plane of closest approach. The average force for each horizontal plane has been subtracted from the data to improve contrast. Figures 68(b) and 68(c) show the interaction forces and tunneling currents for the oxidized Cu surface. Figures 68(d) and 68(e) show forces and currents for a  $\text{TiO}_2$  surface in the rutile modification. Heyde *et al.* have used an AFM with a tuning

force based sensor to study the atomic structure of glasses and silica.<sup>29</sup> The IBM Almaden group investigated the structure and thickness of insulating films on metals that are used to provide isolated carriers for atomic spin structures.<sup>15</sup>

### 18. Exchange force microscopy

Nickel oxide ( $\text{NiO}$ ) is a very special metal oxide because of its antiferromagnetic structure. Shortly before atomic resolution by AFM was obtained, Mukasa *et al.* proposed to probe magnetic exchange forces by force microscopy.<sup>172</sup> More than a decade passed, until Kaiser, Schwarz, and Wiesendanger succeeded to image  $\text{NiO}$  and show the  $2 \times 1$  magnetic superstructure in 2007.<sup>135</sup> However, unit cell averaging was necessary to clearly show the  $2 \times 1$  magnetic superstructure and a 5 T magnetic field had to be applied to stabilize the magnetization of the iron covered Si tip. In 2013, the initial attempt to resolve the antiferromagnetic order on the  $\text{NiO}$  surface



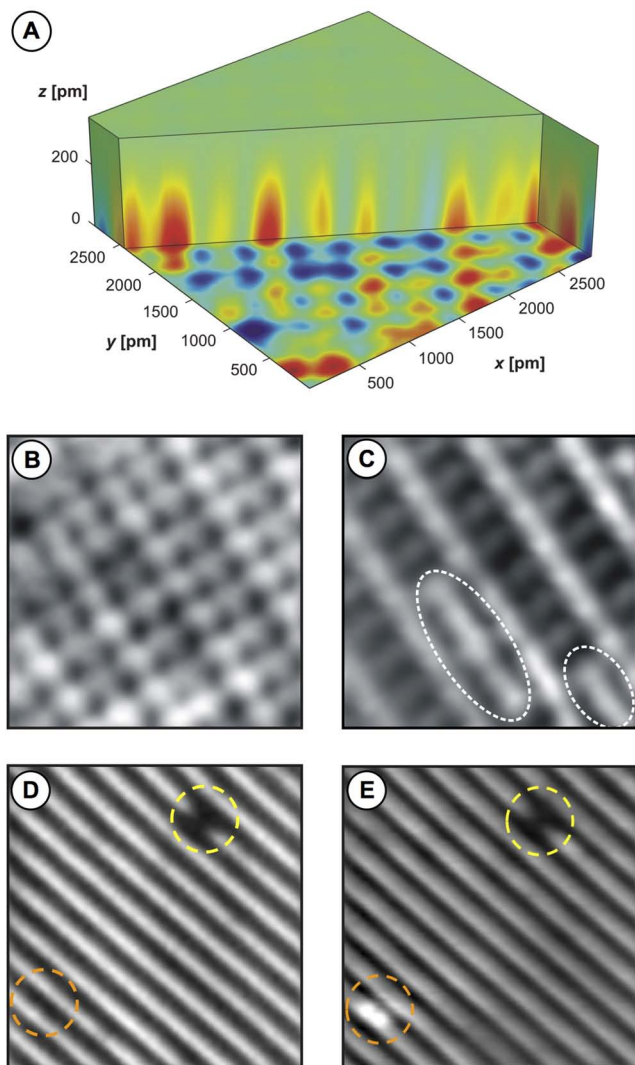


**FIG. 68.** Combined measurement of interaction forces and tunneling currents on metal oxide surfaces. (a) 3D plot of interaction forces recorded on a surface-oxidized Cu (100) crystal. Total force contrast is 22 pN (red: most attractive and blue: least attractive). (b) 2D map of interaction forces ( $2.89 \times 2.89 \text{ nm}^2$ ) extracted from the 3D data set in (a), maxima correspond to oxygen atoms on the surface. (c) 2D map of tunneling currents recorded simultaneously with the force map of (b). In contrast to forces, the maxima in the tunneling current coincide with the copper atoms on the surface. The presence of linear defects on the surface is highlighted by the dashed white ellipses. The total current contrast is 7 pA. (d) 2D map of interaction forces ( $6.55 \times 6.55 \text{ nm}^2$ ) extracted from a 3D data set recorded on rutile TiO<sub>2</sub> (110). The dashed yellow circle highlights an oxygen vacancy, whereas no perturbation is detected in the force data around the orange dashed circle. The total force contrast is 100 pN. (e) 2D map of tunneling currents recorded simultaneously with the force map of (d). While the oxygen vacancy is observed again, a subsurface, interstitial hydrogen atom causes an additional perturbation of the tunneling current at the location highlighted by the dashed orange circle. The total current contrast is 368 pA. The data in (a)–(c) have been acquired at  $T = 5 \text{ K}$  using a qPlus sensor with  $A \approx 1.00 \text{ nm}$ ,  $k \approx 2000 \text{ N/m}$ , and  $f_0 = 29\,177 \text{ Hz}$ .<sup>16</sup> The data in (d) and (e) have been acquired at  $T = 77 \text{ K}$  using a qPlus sensor with  $A \approx 1.50 \text{ nm}$ ,  $k \approx 2000 \text{ N/m}$ , and  $f_0 = 25\,328 \text{ Hz}$ .<sup>17</sup> Reprinted with permission from U. Schwarz. Copyright Udo Schwarz, Yale University, New Haven, USA.

at room temperature with a qPlus sensor<sup>212</sup> was repeated at low temperatures.<sup>190</sup> First experiments using a bulk iron tip resolved the antiferromagnetic order at close distance, but spin contrast was lost again at very close distance (supplemental to Ref. 190). The use of a hard magnetic tip material (CoSm) provided much better data, as shown in Fig. 69. Spin contrast was clearly visible in the raw data of Ref. 190, and force spectroscopy was performed to measure the magnitude of the exchange interaction. In addition, evidence for super exchange was found—the height of the O atoms in Fig. 69 also shows a  $2 \times 1$  structure, in agreement with calculations by Granovskij *et al.*<sup>93</sup> Exchange force microscopy combined with spin-polarized scanning tunneling microscopy to independently characterize the geometric as well as the electronic and magnetic structures of nonflat surfaces has recently been demonstrated in the group of Khajetoorians.<sup>106</sup>

## D. New frontiers

### 1. Atomic force microscopy combined with inelastic electron tunneling spectroscopy

Inelastic electron tunneling spectroscopy (IETS), pioneered by the group of Ho,<sup>227</sup> extends the capabilities of STM to measuring excitations. A further combination of STM with IETS and AFM provides new possibilities. The intensity of IETS signals usually varies from tip to tip. COFI analysis of tips allows us to repeatedly poke and check tips to confirm a single atom tip. Figure 70 shows five different experiments with five different tips that have all been checked by COFI to have a single atom tip, and those tips all produce highly similar IETS spectra with similar intensities.

A second example where the additional input provided by AFM is helpful is to assess the force that the probe tip exerts on vibrating molecules.<sup>181</sup> Figure 71 shows the five contributions that the force exerted from the probe tip to a vibrating CO molecule entails. First, the tip-sample force directly adds to the restoring forces provided by the molecular bonds themselves. Second, the force that acts on the molecule influences the strengths of bonds within the molecule and to the substrate. This is exactly what was found in the experiment—the direct impact of the forces did not suffice to explain the experimental changes in vibrational energies, and bond weakening due to the forces exerted by the tip was evident; see Fig. 72.

### 2. Ultrahigh vacuum at ultralow (mK) temperature and high magnetic fields

Currently, many exciting studies of qPlus based STM/AFM are performed in vacuum at liquid helium temperatures. Extending its operation into the mK regime is promising for a variety of reasons. When studying devices at ultralow temperatures,<sup>145,226</sup> it would often be desirable to approach and navigate on sections of the device that are nonconductive. Therefore, AFM would be mandatory. Another example is the study of the possible different screening of normal versus superconductive states that we attempted at temperatures down to  $2.4 \text{ K}$ ,<sup>188</sup> where lower temperatures are needed to find out if Jorge Hirsch's theory<sup>116</sup> on screening in the superconductive state is accurate.



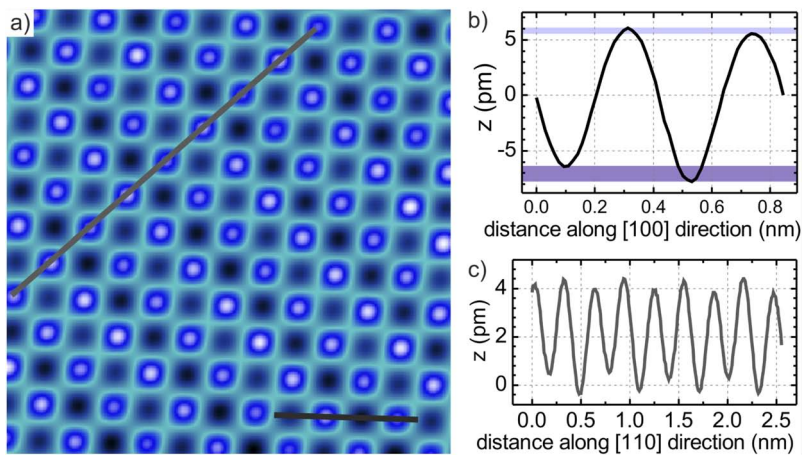


**FIG. 69.** Exchange interaction measured with a qPlus sensor.<sup>190</sup> While exchange force microscopy with spin resolution was first demonstrated with iron plated Si cantilevers<sup>135</sup> using unit cell averaging and an external field of 5 T, the data here were obtained at a very high signal-to-noise ratio (only Gaussian  $5 \times 5$  pixel low pass filtering applied) without an external magnetic field and a CoSm tip attached to a qPlus sensor. Reprinted with permission from F. Pielmeier and F. J. Giessibl, *Phys. Rev. B* **110**, 266101 (2013). Copyright 2013 The American Physical Society.

When getting from the room temperature of 300 K to a liquid helium temperature of 4 K, it may seem as a minor step to conquer the last percent toward absolute zero. Figure 73(a) shows a linear plot of the temperature scale, where it appears like there is not much difference between 4 K and ultralow temperatures at 10 mK. However, many processes in nature are governed by the Boltzmann factor  $\exp(-E/k_B T)$ . Therefore, a comparison of temperatures needs to take the ratio into account. The step from 300 K to 4 K reduces temperature by a factor of  $4/300 = 1/75$ , while the step from 4 K to 10 mK corresponds to a factor of  $1/400$ . Therefore, the instrumental challenges to go from 4 K to the mK regime are much harder than to go from room temperature to 4 K. Furthermore, liquid helium with its boiling temperature of 4.2 K is amply available in many laboratories with commercially available helium

liquefiers, while complicated refrigerators are needed to cool down to the mK regime. This larger challenge is visually evident on the logarithmic scale in Fig. 73(b).

Combinations of high magnetic fields and ultralow temperatures are, e.g., relevant when studying magnetic excitations with inelastic electron tunneling spectroscopy. Magnetic energy levels are given by multiples of  $\mu_B B$ , and the thermal energy is given by the Boltzmann constant times temperature  $k_B T$ . The thermal broadening in inelastic electron tunneling spectroscopy is about  $5.4 k_B T$ .<sup>149</sup> As the Bohr magneton  $\mu_B = 9.27 \cdot 10^{-24}$  J/T is a very small number, it takes high magnetic fields and ultralow temperatures for the two energies to match. The green line in Fig. 73(b) indicates the magnetic field strength  $B$  as a function of temperature  $T$  where  $5.4 k_B T = \mu_B B$ . One application of ultralow temperature IETS is to study Landau levels in graphene.<sup>226</sup>

Ultralow temperatures are a special challenge for scanning probe microscopy because the cooling power of mK cryostats is limited and the requirements of vibration isolation and ultralow temperatures often encounter conflicting objectives. The 10 mK STM of the Stroscio group at NIST Gaithersburg<sup>225</sup> has recently been upgraded to allow simultaneous STM/AFM operation.<sup>217</sup> The special challenge of a 10 mK AFM is the low cooling power of the cryostat and the conflicting needs of the amplifier to require an operating temperature of at least 50 K and a close distance to the sensor. A close distance is helpful to obtain low noise because the capacity of the wire that connects the amplifier and the sensor adds apparent current noise via the input voltage noise of the amplifier. In the case of the NIST microscope, a distance of about 1.2 m between the sensor and the amplifier is required. In most 4 K AFMs, the distance between the sensor and the amplifier is less than 0.1 m—less than one tenth of the distance of the NIST microscope. The wiring between the sensor and the amplifier has two components that contribute to its capacity: length and capacity per length. The capacity of a coaxial wire is given in Eq. (66), showing that a small inner radius  $r_i$ , a large outer radius  $r_a = 550$ , and a low value for the relative dielectric constant of the insulation material  $\epsilon_r$  of the wire are crucial. To minimize cable capacity at NIST

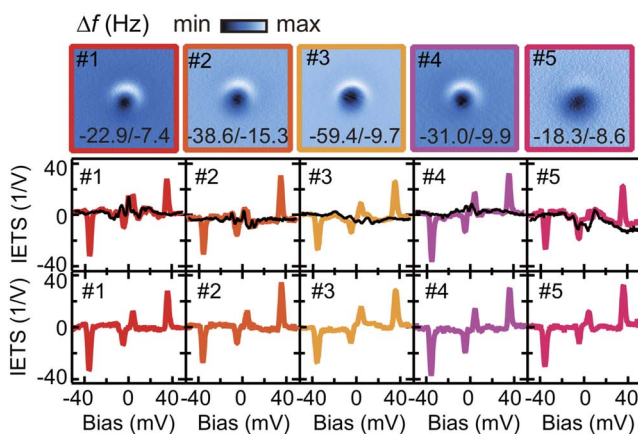


**FIG. 70.** Reproducibility of IETS spectra for five different single atom tips 1-5 that have been characterized by COF1.<sup>180</sup> The data display the individual spectra, including the background measurements. The top row shows the constant-height frequency shift profiles (in Hz) for the five different tips. The center row displays the IETS signal in color and the background spectra in black. The bottom row displays the net IETS signal after background subtraction. Reprinted with permission from Okabayashi et al., *Phys. Rev. B* **93**, 165415 (2016). Copyright 2016 The American Physical Society.

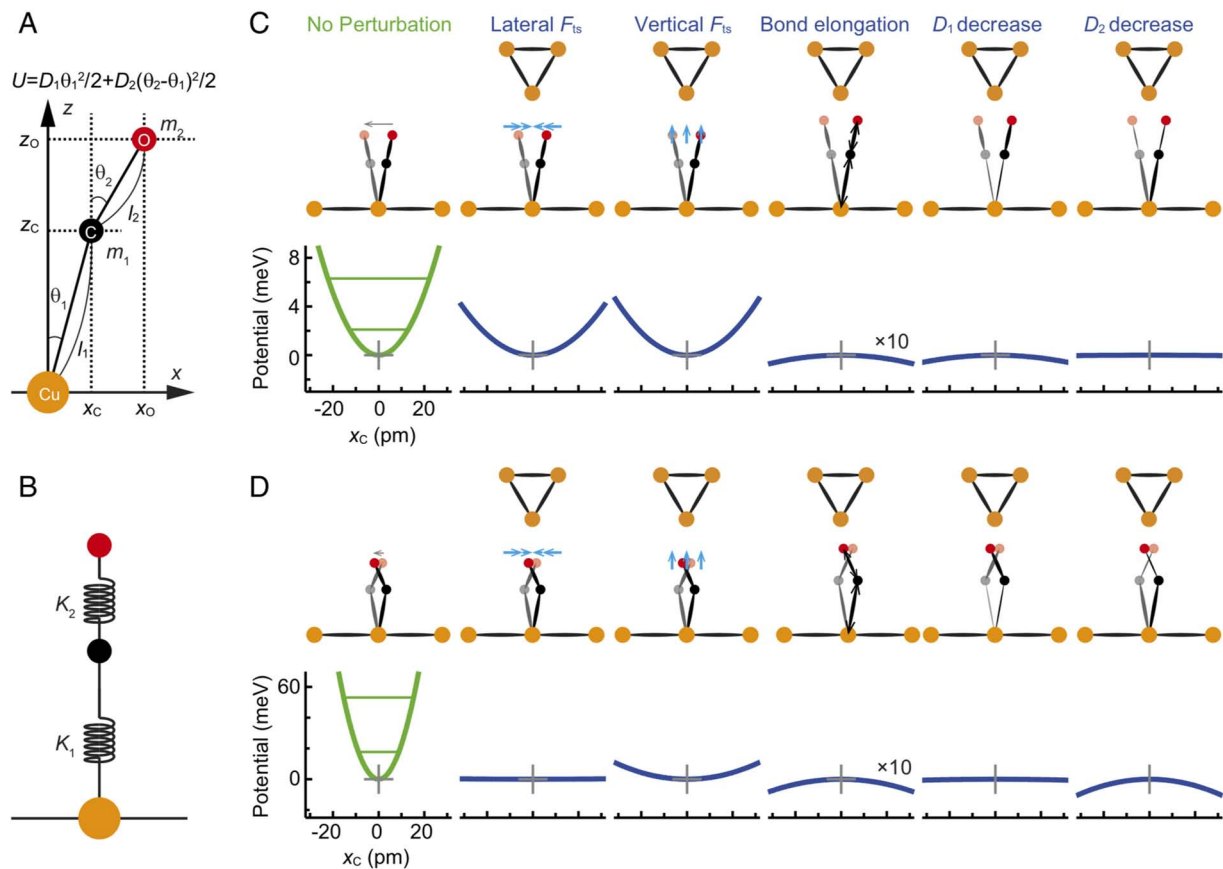


**FIG. 71.** Mechanical model describing the oscillation of a CO molecule on a Cu(111) surface under the force field of the tip.<sup>181</sup> (a) Model for the lateral oscillation modes; the angular force constant  $D_1$  keeps the angle between the Cu-C bond and the surface normal,  $\theta_1$ , close to its potential energy minimum at  $\theta_1 = 0$ , while  $D_2$  straightens the Cu-C-O bond by keeping  $\theta_2 - \theta_1$  close to the energy minimum at  $\theta_2 = \theta_1$ . (b) Model for stretch modes and bond elongations with longitudinal bond stiffness  $K_1$  for the Cu-C bond and  $K_2$  for the C-O bond. (c) Frustrated translational mode of CO and influence of the tip on the potential energy. For the free molecule, the mechanical model finds  $\theta_2 = 1.19\theta_1$ . Analysis of the measured frequency shifts at given external tip forces indicate five different mechanisms of energy shift. First,  $k'_x$ , the lateral gradient of the tip-sample force  $F_{ts}$  directly increases the lateral stiffness, leading to an increased oscillation frequency of the molecule. The vertical component of  $F_{ts}$ ,  $F'_z$ , also leads to an increase in oscillation frequency for attractive forces. The vertical force induces bond lengthening in  $l_1$  and  $l_2$  as well as a decrease in  $D_1$  and  $D_2$ . (d) Frustrated rotational mode of CO and influence of the tip-sample force on the effective bond stiffness. For the free molecule, the mechanical model finds  $\theta_2 = -2.33\theta_1$ . The rotational mode is subject to the same energy-shift mechanisms discussed for the frustrated translation. In contrast to the translational mode where  $k'_x$  and  $F'_z$  and a decrease in  $D_1$  are the main causes for energy shifts, the rotational mode is most susceptible to  $F'_z$  and a decrease in  $D_2$ . Reprinted with permission from Okabayashi *et al.*, Proc. Natl. Acad. Sci. U. S. A. **115**, 4571 (2018). Copyright 2018 National Academy of Sciences.

given the long distance, we designed a cable with a very low capacitance per length of about 25 pF/m and had this cable professionally manufactured.<sup>175</sup> This bicoaxial cable featured two coaxial leads within one external shield. Each of the two coax cables had an inner wire with radius  $r_i = 50 \mu\text{m}$  and a shield with radius  $r_a = 550 \mu\text{m}$ . The insulating material between the leads is PTFE (polytetrafluorethylene-Teflon) with a dielectric constant of  $\epsilon_r = 2$  at the operating frequency of the sensor. According to Eq. (66), this cable with  $r_a/r_i = 11$  yields a theoretical capacitance of 23 pF/m close to the experimental value. Typical capacities per length of coaxial cables are 100 pF/m, so the effort to design a custom cable has proven to be worth the cost and effort. In many 4 K systems, where the amplifier can be close to the sensor, the connection

between the sensor and the amplifier is just done by a pair of thin wires that float in vacuum. In that case, the ratio  $r_a/r_i$  is on the order of 10 to 100 with the dielectric constant of vacuum  $\epsilon_r = 1$ , yielding even lower capacities per length and much lower total capacities due to possible lengths on the order of 0.1 m.

The NIST team performed preliminary measurements applying a magnetic field up to 15 T with sensor type qPlus S1.0B (see Table I). The sensor still operates, but the Q value drops to about 20 000 at  $|\vec{B}| = 8 \text{ T}$ . An even stronger damping effect had been reported previously by James Hedberg<sup>108</sup> from Peter Grütter's group at McGill University using qPlus sensors made of tuning forks. In these experiments, Hedberg found a drop in Q to only 1700 at a field of 8.5 T. A plot of

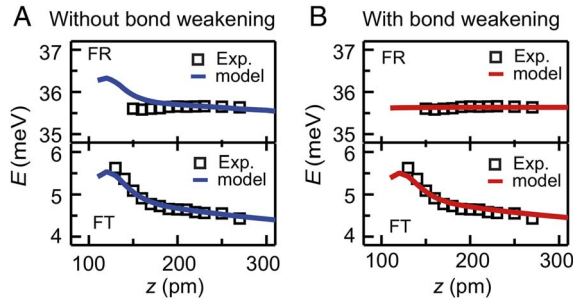


**FIG. 72.** Comparison of experimental and simulated FT and FR mode energies assuming constant (a) and modified (b) bond strength.<sup>181</sup> (a) Energy shift of the vibrational modes under the perturbation potential using fixed values for the angular force constants  $D_1 = 138$  zNm and  $D_2 = 217$  zNm, corresponding to the unperturbed vibrational energy of  $E_{FT} = 4.25$  meV and  $E_{FR} = 35.45$  meV. (b) Energy shift of the vibrational modes using softened angular force constants  $D'_{1,2} = D_{1,2} \cdot (1 - \beta \cdot F_z)$ . The best-fit values are  $D_1 = 143$  zNm,  $D_2 = 219$  zNm, corresponding to the unperturbed vibrational energy of  $E_{FT} = 4.32$  meV and  $E_{FR} = 35.64$  meV, and  $\beta = 0.033\%/pN$ . Reprinted with permission from Okabayashi *et al.*, Proc. Natl. Acad. Sci. U. S. A. **115**, 4571 (2018). Copyright 2018 National Academy of Sciences.

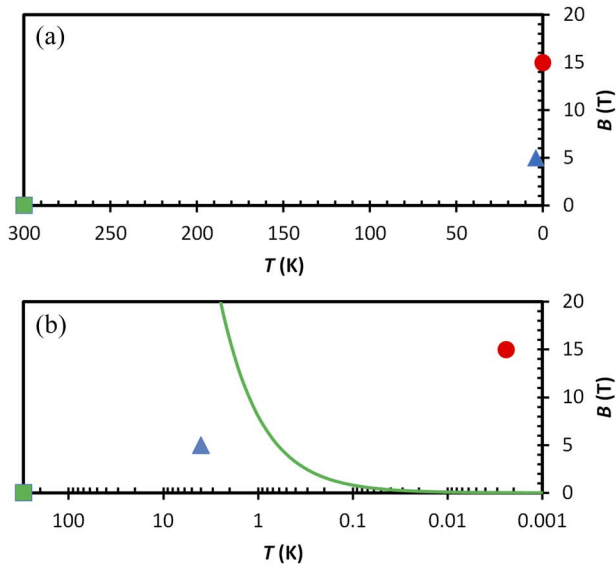


**FIG. 73.** Plot of temperature [linear in (a) and logarithmic in (b)] and magnetic field with three examples of microscopes: a room temperature AFM without a magnetic field (green squares), a 4 K AFM with a 5 T field (blue triangles), and a 10 mK AFM with a 15 T field (red circles). (a) On a linear temperature scale, the difference between a 4 K AFM and a 10 mK AFM seems little. (b) A logarithmic temperature scale is more appropriate to reflect the instrumental challenges of a 4 K microscope versus a 10 mK microscope—the step from 4 K to 10 mK is much larger on a logarithmic scale than from 300 K to 4 K. Magnetic fields allow us to study magnetic excitations on energy scales of  $\mu_B B$ , with the Bohr magneton  $\mu_B = 9.27 \cdot 10^{-24}$  J/T. The energy resolution of tunneling spectroscopy is on the order of  $5.4 k_B T^{226}$  with the Boltzmann constant  $k_B$ . The green line in (b) is given by  $\mu_B B = 5.4 k_B T$ ; i.e., to be able to resolve energies on the order of  $\mu_{Bohr} B$ , a microscope needs to provide a sufficiently large ratio between magnetic field and operating temperature, indicated by the region above and to the right of the green line in (b).

damping that is proportional to  $1/Q$  showed a proportionality to the square of the magnetic field  $B$ . While the lowering in  $Q$  leads to increased oscillator noise (scaling as  $1/Q$ ) and to a lesser extent increased thermal noise (scaling as  $\sqrt{T/Q}$ ), it does not prevent one to obtain atomic resolution.

The origin of this magnetic field induced damping is not clear yet, Hedberg discussed (p. 89 in Ref. 108) four potential origins: (1) (anti)ferromagnetic metals in the tuning fork electrodes, (2) eddy currents in the tuning fork electrodes, (3) eddy currents in the tungsten tip, and (4) intrinsic dissipation of the quartz crystal.

The following analysis suggests that eddy currents in the electrodes of the sensor that are strained with the oscillation of the beam are a relevant channel for damping. Faraday's law states that a voltage is induced in a closed conductor given by the time derivative of the magnetic flux (see Chap. 17 in Vol. II of Ref. 62). The induced voltage leads to eddy currents in a current loop, and these currents will cause dissipation. Eddy currents are therefore induced in conductors that move through a magnetic field gradient.

Figure 74(a) shows a qPlus sensor with a magnetic field  $\vec{B}$  applied in the  $z$ -direction, i.e., parallel to the tip and its motion. The oscillating magnetic flux in the sensor electrode in Fig. 74(b) induces a voltage (see the caption of Fig. 74) given by

$$V_{induced} = |\vec{B}| \cdot w \cdot L_e \cdot \epsilon \cdot \sin(2\pi f t) \cdot 2\pi f. \quad (81)$$

The strain  $\epsilon$  at deflection  $A$  of the sensor is not constant; according to Eq. (53), it is maximal at the root of the beam at  $x = 0$  and falls to zero proportional to  $x - L$ . With Eq. (53),  $F = k \cdot A$ , and Eq. (51), we find

$$\epsilon(x) = \frac{3}{8} \frac{(x - L) \cdot th}{L^3} \cdot A. \quad (82)$$

For an amplitude of  $A = 50$  pm and a sensor S1.0B with  $L = 2.36$  mm and  $th = 214$   $\mu$ m, we obtain a maximal strain at  $x = 0$

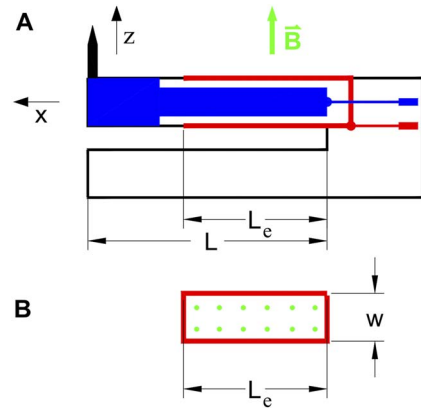


**FIG. 74.** (a) Schematic view of a qPlus sensor in a magnetic field  $\vec{B}$ . (b) Top (or bottom) electrode, penetrated by the magnetic field lines  $\vec{B}$  (green dots). Due to the oscillation of the tip, the area covered by the electrode and thus the magnetic flux  $\Phi$  is not constant but changes slightly according to  $\Phi(t) = |\vec{B}| \cdot w \cdot L_e \cdot (1 + \epsilon \cos(2\pi f t))$  where  $\epsilon$  is the strain at the top and bottom parts of the sensor beam when it is deflected at amplitude  $A$ .



amounting to  $\epsilon = 7.2 \cdot 10^{-10}$ , resulting in a peak voltage of  $V_{\text{induced } 0} = 0.42 \text{ nV}$  for  $|\vec{B}| = 10 \text{ T}$ . The current loop indicated in Fig. 74(b) has an approximate resistance of

$$R \approx \rho_{\text{el}} \cdot \frac{2 \cdot (L + w)}{w/2 \cdot th_{\text{Au}}}, \quad (83)$$

where  $th_{\text{Au}}$  is the thickness of the Au metallization in the electrodes and  $\rho_{\text{el}}$  is the specific resistivity of the electrode material (typically 300 nm Au on top of 25 nm Cr). At room temperature, the specific resistivity of gold is  $\rho_{\text{el}} \approx 20 \text{ n}\Omega\text{m}$  (similar to Ag and Cu). However, at low temperatures, resistance goes down by about two orders of magnitude (according to Ref. 128,  $\rho_{\text{el Au}} \approx 0.2 \text{ n}\Omega\text{m}$  between 1 and 10 K). However, defects are a main source of resistance and the actual value depends a lot on the pureness of the sample. Assuming a specific resistivity of  $\rho_{\text{el Au}} = 0.2 \text{ n}\Omega\text{m}$ , we find a resistance of  $R = 51 \text{ m}\Omega$  for this current loop. Due to the sinusoidal time dependence of the induced voltage, the average power dissipation of these eddy currents is  $P = V_{\text{induced}}^2 / (2R) = 1.7 \text{ aW}$  and the energy loss per oscillation cycle is  $\Delta E_{\text{loss}} = P/f = 57 \text{ yJ} = 0.71 \text{ meV}$  when considering both top and bottom electrodes. Equation (40) can be reversed to yield an expression for the Q factor as a function of  $\Delta E_{\text{loss}}$ ,

$$Q = 2\pi \frac{E_{q\text{Plus}}}{\Delta E_{\text{loss}}}, \quad (84)$$

where  $E_{q\text{Plus}} = kA^2/2$ . For an oscillation amplitude of  $A = 50 \text{ pm}$  and  $k = 1800 \text{ N/m}$ , we find  $E_{q\text{Plus}} \approx 14 \text{ eV}$ ; thus, if the Q factor was infinite without the magnetic field, Q would go down to about 125 000 due to this eddy current damping according to Eq. (84). This is still large compared to the experimental drop in Q to 1700 in Hedbergs case or 20 000 at NIST.

However, a change in magnetic flux and thus an induced voltage in the sensor electrodes also occurs if the magnetic field in the cryostat is even only slightly inhomogeneous. If the magnetic field changes by a similar magnitude as the strain ( $\epsilon = 7.2 \cdot 10^{-10}$  for the example above) on the lengthscale of the sensor's oscillation amplitude (typically 50 to 200 pm), there will be a similar damping effect. If the field would change by a relative amount of  $7.2 \cdot 10^{-9}$  over a distance of  $2 \cdot A = 100 \text{ pm}$ , corresponding to a field gradient of  $7.2 \cdot 10^{-9} \cdot 10 \text{ T}/100 \text{ pm} = 7.2 \text{ T/cm}$ , Q would drop to 12 500 due to this effect. Moreover, in an inhomogeneous magnetic field, all conductive and moving parts of the sensor (the tip in particular) would be subject to eddy current damping. Both suggested eddy current damping mechanisms, the strained electrode and the inhomogeneous field contributions, yield damping that is proportional to the square of the magnetic field as experimentally observed.

The homogeneity of the magnetic field in a high-field superconductive magnet directly determines the field dependent damping by eddy currents. American Magnetics<sup>5</sup> quoted homogeneities of  $\pm 0.1\%$  in a one-centimeter diameter spherical volume as routine. For a 10 T magnet, this homogeneity corresponds to a field gradient of  $0.002 \cdot 10/0.5 \text{ T/cm} = 40 \text{ mT/cm}$ , still small compared to the gradient quoted above. However, the sensor is mounted on a microscope, and the magnetic permeability of the materials used in the microscope

will change the local magnetic field and cause larger field gradients.

In summary, it appears reasonable that eddy current damping is the main reason for reduced Q values at high magnetic fields. However, more studies are needed to verify this mechanism. If this mechanism is correct, the use of the electrode and tip material with a higher resistivity, smaller tips and possibly changing the geometry of electrodes by applying cuts to prevent the occurrence of large current loops should greatly reduce the drop of Q in high fields.

## VI. SUMMARY AND OUTLOOK

The hurdles that had to be overcome in the introduction of the STM were deep and profound. Perhaps the largest hurdle was to imagine that a tip and a sample could be positioned and scanned at the required accuracy and to actually do the experiment. Many scientists and engineers considered this to be plainly impossible at the time the STM was introduced. However, the physics of the tunneling current as the STM's control signal, an exponential decay versus distance at a rate of a decade per Angstrom, helped immensely. The rapid decay meant that even a relatively blunt tip would enable atomic resolution because even then the tunneling current was focused on the front atom of the tip. The monotonic exponential decrease in the tunneling distance with distance allows us to create a very simple distance control loop. Neither of these two beneficial properties of the control signal holds for the AFM. Instead, four basic challenges that relate to the physics of the tip-sample forces emerged: (1) a soft spring used as a force sensor suffers from a jump-to-contact phenomenon, (2) tip-sample forces are not monotonic with distance, initially attractive, and then repulsive, making it difficult to establish a feedback loop, (3) long range forces of potentially large magnitude are overlayed on the short range forces that are needed for obtaining atomic images, and (4) the measurement of forces in the nN and pN regime is more difficult than measuring currents of magnitudes ranging from nA to pA.

Today, many companies provide commercial low temperature STM/AFMs that utilize the qPlus sensor. This helps the scientific community to study matter on the atomic scale with much greater precision and versatility, and breakthrough results are published monthly around the globe using this new technology.

## ACKNOWLEDGMENTS

Tiny machinery has fascinated me as long as I can think. I thank Gerd Binnig for having offered me the opportunity to explore atomic force microscopy as a graduate student at the IBM Physics Group Munich thirty years ago. Gerd had received the Nobel Prize in Physics together with Heinrich Rohrer for the invention of STM in 1986. He resisted the many temptations to constantly travel around the world giving talks that go along with this highest honor and moved on to set very ambitious new goals, offering a choice of three potential PhD projects to me: (a) sequencing DNA by STM, (b) designing a tunneling detector to measure gravitational waves, or (c)

explore and realize the potential of AFM to obtain true atomic resolution. I chose the latter, and that kept me busy for the rest of my life so far. Although Gerd started a highly successful company for computerized image analysis from 1995, he kept an open ear and door to discuss the further evolution of force microscopy even today. Christoph Gerber helped to set up the IBM Physics Group in Munich and set an example for boundless energy in cheerfully pursuing big scientific goals. He also helped me to return to science after almost 5 years in industry by establishing contact with Jochen Mannhart. I first met Calvin F. Quate in the late 1980s when he visited our group in Munich. He supplied us with cantilevers and served on the board of Park Scientific Instruments (PSI) where I worked as a senior scientist after receiving a PhD in Munich. In his visits to PSI, Cal would often drift into the UHV research area, patting my back and stating: “You can do it, Franz,” “it” meaning to atomically resolve the iconic silicon  $7 \times 7$  surface by AFM. He also worked with us in the late 1990s on a few projects involving the imaging of graphite. Theodor Hänsch had hosted the IBM physics group in his laboratory space at Ludwig Maximilians University Munich from 1988 until 1995. Ted also loaned me some equipment in 1996 when I took the first steps of the qPlus development in my home laboratory in Munich. McKinsey&Company, Inc., supported the first steps to the invention of the qPlus sensor by offering paid and unpaid vacation in the summer of 1996. At a time, where the potential of the qPlus sensor were mainly pipe dreams, Jochen Mannhart offered me a permanent position in Augsburg. He cheerfully encouraged exciting new AFM projects and was fully engaged with brains, hands, and heart. Diploma and PhD students Stefan Hembacher, Markus Herz, Martin Breitschaft, and Martina Schmid and visiting scientist Toyooki Eguchi worked hard on the first implementations of qPlus sensors at low temperatures in Augsburg. In Regensburg, the first PhD students Elisabeth and Thorsten Wutscher enabled first steps to AFM in ambient conditions using the qPlus sensors as well as the discovery of the phantom force. Joachim Welker achieved the first precise low temperature measurements in Regensburg, Florian Pielmeier achieved spin resolution by exchange force microscopy, and Maximilian Schneiderbauer and Matthias Emmrich built a custom designed low temperature microscope and produced wonderful data with it. Thomas Hofmann obtained very nice results on graphene, lateral force microscopy, and COFI data. Daniel Wastl was a huge driving force in ambient measurements, and the work in ambient conditions is continued forcefully with graduate students Dominik Kirpal, Korbinian Pürckhauer, and Hiroshi Ooe, guest from Kanazawa University. Ferdinand Huber perfected the science of force detection as well as subatomic resolution. Julian Berwanger worked on topological insulators and helped to get the NIST 10 mK STM/AFM of the group of Joseph Stroscio up and running. A big thank you also to Postdoctoral Fellows Sonia Matencio from Spain, Jay Weymouth from Canada, and Angelo Peronio from Italy. Sonia has performed beautiful experiments on clusters and on imaging molecules at room temperature. Jay arrived with an excellent knowledge about STM and surface science and has pushed forward ambient AFM, lateral force microscopy, and the phantom force

studies, culminating in an award winning habilitation. Angelo has provided great progress in the combination of STS with AFM, together with our frequent guest, co-author, and visiting professor Norio Okabayashi from Japan. Anja Merkel and Florian Griesbeck have provided expert technical assistance in designing and machining mechanical and electrical parts and components. A big thank you for proofreading goes to Korbinian Pürckhauer (chapter I), Ferdinand Huber (chapter II), Julian Berwanger (chapter III), Angelo Peronio (chapter IV), Dominik Kirpal, Alexander Liebig, and Jay Weymouth (chapter V). Thanks also to Petra Wild for obtaining all the reprint permissions. One of the benefits of working at a university is the constant flow of young people into our group. Many of these young bachelor and master students have provided important impact by bringing their skills and curiosity into our group.

I wish to thank the groups at IBM Almaden (Andreas Heinrich, Christopher Lutz, Don Eigler) and IBM Rüschlikon (Gerhard Meyer and Leo Gross) who were early adopters of the qPlus sensor and invited me to several visits and joint projects. Gerhard Meyer is a coinventor of the beam deflection technique<sup>159</sup> and demonstrated high resolution AFM in vacuum<sup>160</sup> as well as biaxial AFM<sup>161</sup> with it early on. The beam deflection technique is by far the most popular method to measure the deflection of cantilevers in an estimated 10 000 ambient AFMs around the globe. Usually, the “not-invented-here-syndrome”<sup>177</sup> would prevent a highly successful inventor to even try a competing technique, but Gerhard had the greatness to see some benefits, enabling his and Leo Gross’ breakthroughs in imaging organic molecules with the qPlus sensor that opened a new field. Joseph Stroscio at NIST invited me to spend a sabbatical in his group where we just started to explore the possibilities of qPlus based STM/AFM at ultralow temperatures and high magnetic fields. Also, a big thanks to Jascha Repp who runs a phantastic group on atomic scale science on insulating films using STM/AFM next door here in Regensburg and provides continuous physical insights into surface science and related topics in our joint group seminar and discussions.

A special thank you to many groups around the world who have contributed data to the section on applications (in alphabetical order): Mehmet Baykara and Udo D. Schwarz (UC Merced/Yale University, USA), Mike Crommie (University of Berkeley, USA), Ulrike Diebold and Martin Setvin (TU Vienna, Austria), Leo Gross and Gerhard Meyer (IBM Rüschlikon, Switzerland), Pavel Jelinek (Czech Institute of Science, Prague, Czech Republic), Ying Jiang (Peking University, China), Ernst Meyer and Shigeki Kawai (University of Basel, Switzerland and NIMS, Tsukuba, Japan), Philip Moriarty and Adam Sweetman (University of Nottingham, UK and University of Leeds, UK), Xiaohui Qiu (National Center for Nanoscience and Technology, Beijing), Yoshiaki Sugimoto (University of Tokyo, Japan), Jascha Repp (University of Regensburg, Germany), Joseph Stroscio (NIST Gaithersburg, USA), Ingmar Swart (University of Utrecht, Netherlands), Stefan Tautz and Ruslan Temirov and Christian Wagner (Forschungszentrum Jülich, Germany), and Robert Wolkow (University of Alberta, Edmonton, Canada).

Funding by Deutsche Forschungsgesellschaft through GRK 1570, SFB 689, and SFB 1277 is gratefully acknowledged.

Also, I thank Drs. Frank Fang, Bernd Studer, and Bernhard Schnyder for sensor fabrication. Furthermore, I wish to thank all the companies that have adopted the qPlus sensor in their instruments. This has widened the breadth of exploration enormously and enabled a very high output of exciting new research that became possible with high resolution AFM and its combination with STM. Finally, I thank the artist Gerhard Richter for many lessons on endurance, staying power, and a constant strive for quality.

## APPENDIX A: LIST OF SYMBOLS

### 1. General physical quantities and constants

Note: On 16 November 2018, the 26th General Conference on Weights and Measures (CGPM) voted unanimously in favour of revised definitions of the SI base units. In this revision, the elementary charge and the Boltzmann constant were fixed to the values given below. The new definitions will be effective on 20 May 2019.<sup>265</sup>

Symbol	Meaning	Value (unit)
$t$	Time	(s)
$T$	Temperature	(K)
$B$	Bandwidth	(Hz)
$\vec{B}$	Magnetic field	(T)
$e$	Elementary charge	$1.602\,176\,634 \cdot 10^{-19}$ (C)
$c$	Speed of light	$299\,792\,458$ (m/s)
$\mu_0$	Magnetic constant	$4\pi \cdot 10^{-7}$ Vs/(Am)
$\epsilon_0$	Permittivity of free space	$1/(c^2\mu_0) \approx 8.854\,187\,817$ (pF/m)
$k_B$	Boltzmann constant	$1.380\,649 \cdot 10^{-23}$ (J/K)
$\mu_B$	Bohr magneton	$9.274\,009\,994(57) \cdot 10^{-24}$ (J/T)

### 2. Mechanical sensor properties

Note: Cantilever and force sensor are used as synonyms here.

Symbol	Meaning	Unit
$k$	Stiffness of the cantilever	(N/m)
$f_0$	Eigenfrequency of the cantilever	(Hz)
$f$	Oscillation frequency of the cantilever	(Hz)
$\omega$	Angular frequency of the cantilever	(1/s)
$A$	Oscillation amplitude of the cantilever	(m)
$L$	Length of the cantilever	(m)
$th$	Thickness of the cantilever	(m)
$w$	Width of the cantilever	(m)
$Q$	Quality factor of the cantilever	(1)
$E_Y$	Young's modulus	(N/m <sup>2</sup> )
$J$	Area moment of inertia	(m <sup>4</sup> )
$\epsilon$	Mechanical strain	(1)
$\sigma$	Mechanical stress	(N/m <sup>2</sup> )
$\rho$	Mass density	(kg/m <sup>3</sup> )

### 3. Electrical sensor properties

Symbol	Meaning	Unit
$S_q$	Sensitivity charge per deflection	(C/m)
$S_F$	Sensitivity charge per force	(C/N)
$n_q$	Deflection noise density	(m/ $\sqrt{\text{Hz}}$ )
$d_{21}$	Transverse piezoelectric coupling constant	(C/N)
$\rho_{el}$	Specific resistivity	( $\Omega\text{m}$ )

### 4. Tip-sample interaction

Symbol	Meaning	Unit
$V_{ts}$	Tip-sample potential	(J)
$F_{ts}$	Tip-sample force $-\partial V_{ts}/\partial z$	(N)
$k_{ts}$	Tip-sample force gradient $\partial^2 V_{ts}/\partial z^2$	(N/m)
$\kappa$	Decay constant of interaction	(1/m)
$\lambda$	Decay length of interaction	(m)

## APPENDIX B: PERSONAL NOTE ON THE INVENTION OF THE qPlus SENSOR

The force sensor and tip have always been crucial to the atomic force microscope. During my Ph.D. thesis with Gerd Binnig at the IBM Physics Group Munich, we used the tunneling effect to measure cantilever deflection as outlined in Ref. 25. However, we upgraded from homebuilt cantilevers from Au foil and diamond splinters as in the original AFM<sup>25</sup> to micromachined amorphous SiO<sub>2</sub> and Si<sub>3</sub>N<sub>4</sub> cantilevers from Park Scientific Instruments, Inc., in Sunnyvale, California (PSI) that had been designed in the Quate laboratory. PSI had been cofounded by Stanford graduate Sang-il Park. Sang-il Park had done his PhD with Calvin Quate, designing one of the first STMs that reproduced imaging of the famous silicon (111)-(7 × 7) surface pioneered by Binnig, Rohrer, Gerber, and Weibel.<sup>22</sup> After having completed my PhD with Gerd Binnig in Munich, I joined Park Scientific Instruments on July 1992 to design a vacuum compatible AFM together with Brian Trafts.<sup>70</sup> This microscope had many innovations: it migrated from the Hewlett Packard work station to the IBM personal computer using Windows 3.11, it utilized a piezoelectric motor for coarse approach and lateral sample motion, and most importantly, it included a frequency modulation AFM based on a self-sensing, piezoresistive cantilever.<sup>241</sup> Park Scientific Instruments obtained a patent license for the piezoresistive silicon cantilever from Stanford University, and Marco Tortonese, who had worked on the piezolever as a graduate student with Calvin Quate, joined PSI to build levers. Thomas Albrecht, the lead author of the first paper on FM-AFM,<sup>2</sup> consulted PSI at that time to evaluate FM-AFM in PSI's ambient AFMs and designed a box that included a positive feedback for self-excitation of cantilevers and an analog T-circuit that measured the frequency shift. While FM-AFM was not pursued



further in ambient AFM at that time, we adapted the FM box to our vacuum AFM. The design of the vacuum AFM proceeded quickly—one of the blessings of working in silicon valley was the quick machine shops who would pick up a drawing in the evening and return the machined parts in the next morning. The piezoresistive cantilevers worked well in FM-AFM, and in November 1993, we submitted our first paper on its applications showing atomic steps and a lateral resolution below 3 nm<sup>70</sup> and atomic rows on Si.<sup>69</sup> In the spring and summer of 1994, a long standing challenge in atomic force microscopy was finally solved: obtaining atomic resolution on the silicon (111)-(7 × 7) surface.<sup>71</sup> At that point, I thought that my career in science is over—big goal achieved, nothing else on the horizon. As I had been hired by PSI to design a commercial UHV microscope, and the product achieved an outstanding goal, I found it hard to understand why the microscope did not sell by itself. To find that out, I joined the Munich office of McKinsey&Company, Inc., to explore a different realm of hard work.<sup>189</sup> However, there was one more thing about successfully obtaining atomic resolution on Si(111)-(7 × 7) that bothered me deeply: the oscillation amplitude of the cantilever had to be very large. Incredulously about its implications, I even showed a scale representation of that in Fig. 4 of Ref. 71. In my little spare time between those long consulting hours (and paid as well as unpaid vacation—thanks again to McKinsey), I finally found a reason why large amplitudes were required: stability. A much stiffer cantilever was required. I had learned through my diploma work with Gerhard Abstreiter at the Technical University of Munich that a single covalent Si-Si bond has a stiffness of 170 N/m. The cantilever I had used at PSI had only 10% of that stiffness. So, if one would manage to create levers with 1700 N/m, one would still achieve a frequency shift of 5% and be able to oscillate at small amplitudes.

Furthermore, the new vocation at McKinsey encompassed several functional benchmarking studies. The idea of benchmarking is to identify a weak spot in a business operation and model whoever is best in that particular operation to get to an excellent performance level.<sup>189</sup> It dawned on me that, when musing about improvements of frequency modulation atomic force microscopy, we never studied the techniques elaborated by the champions of frequency measurements. Atomic clocks, of course. But quartz watches come next and are really simple. Most quartz watches use a quartz tuning fork that oscillates at  $f_0 = 2^{15}$  Hz = 32 768 Hz. The tines of the tuning forks are typically 2–3 mm long and have a stiffness of about 2–10 kN/m. The two tines form two coupled oscillators that oscillate in an antiparallel mode where they reach Q-values of 100 000 when placed in an evacuated metal can. While piezoelectric sensors had been used in scanning probe microscopy with normal forces<sup>13</sup> and shear forces before,<sup>45,136,137</sup> the systematic use of them based on a mathematical analysis of the required sensor properties was new.

When I learned about quartz tuning forks, two questions came to mind: (a) can one make them to oscillate with amplitudes of an atomic diameter instead of their typical amplitudes of  $A \approx 5 \mu\text{m}$  and (b) can one still obtain reasonably high Q-values when one of the tines is tied down and the other one

carries a tip as needed when turning it into a quartz cantilever. Management consultants typically do not have ready access to a well stocked laboratory, so I purchased an oscilloscope, a frequency counter, and an oscillator and borrowed an ambient STM from Theodor Hänsch at Ludwig Maximilians University Munich who had hosted our IBM Research Group Munich in his premises at the University before. Early experiments in the home laboratory confirmed that high Q values can be obtained with one fixed prong, and oscillation amplitudes can be reduced to at least nanometers. The combination of past experience, theoretical background, and promising new trials<sup>130</sup> gave me confidence for another change in career. I dubbed the new device “qPlus sensor,” filed for and later obtained patents<sup>72–76</sup> and a registered trademark qPlus<sup>®</sup>,<sup>77</sup> and searched for a way to turn its high promise into reality. Many people helped me in this effort; hopefully most are listed in the acknowledgments, but I am sure I forgot some. So thank you as well!

## REFERENCES

- <sup>1</sup>M. Abramowitz and I. A. Stegun, *Handbook of Mathematical Functions* (Dover Publications, New York, 1970).
- <sup>2</sup>T. R. Albrecht, P. Grutter, H. K. Horne, and D. Rugar, “Frequency modulation detection using high-Q cantilevers for enhanced force microscope sensitivity,” *J. Appl. Phys.* **69**, 668 (1991).
- <sup>3</sup>F. Albrecht, N. Pavlicek, C. Herranz-Lancho, M. Ruben, and J. Repp, “Characterization of a surface reaction by means of atomic force microscopy,” *J. Am. Chem. Soc.* **137**, 7424 (2015).
- <sup>4</sup>F. Albrecht, F. Bischoff, W. Auwärter, J. V. Barth, and J. Repp, “Direct identification and determination of conformational response in adsorbed individual nonplanar molecular species using noncontact atomic force microscopy,” *Nano Lett.* **16**, 7703 (2016).
- <sup>5</sup>See <http://www.americanmagnetics.com/charactr.php> for American Magnetics, 112 Flint Rd, Oak Ridge, TN 37830-7068.
- <sup>6</sup>T. An, T. Eguchi, K. Akiyama, and Y. Hasegawa, “Atomically-resolved imaging by frequency-modulation atomic force microscopy using a quartz length-extension resonator,” *Appl. Phys. Lett.* **87**, 133114 (2005).
- <sup>7</sup>T. An, T. Nishio, T. Eguchi, M. Ono, A. Nomura, K. Akiyama, and Y. Hasegawa, “Atomically resolved imaging by low-temperature frequency-modulation atomic force microscopy using a quartz length-extension resonator,” *Rev. Sci. Instrum.* **79**, 033703 (2008).
- <sup>8</sup>S. An, B. Sung, H. Noh, S. Corey, S. Kwon, K. Lee, B. Kim, Q. Kim, and W. Jhe, “Position-resolved surface characterization and nanofabrication using an optical microscope combined with a nanopipette/quartz tuning fork atomic force microscope,” *Nano-Micro Lett.* **6**, 70 (2014).
- <sup>9</sup>See [www.analog.com](http://www.analog.com) for Analog Devices, One Technology Way, P.O. BOX 9106 Norwood, MA 02062, USA.
- <sup>10</sup>B. Anczykowski, D. Kruger, and H. Fuchs, “Cantilever dynamics in quasi-noncontact force microscopy: Spectroscopic aspects,” *Phys. Rev. B* **53**, 15485 (1996).
- <sup>11</sup>See [www.atceramics.com](http://www.atceramics.com) for American Technical Ceramics, One Norden Lane, Huntington Station, NY 11746, USA.
- <sup>12</sup>L. Bartels, G. Meyer, and K. H. Rieder, “Controlled vertical manipulation of single CO molecules with the scanning tunneling microscope: A route to chemical contrast,” *Appl. Phys. Lett.* **71**, 213 (1997).
- <sup>13</sup>K. Bartzke, T. Antrack, K.-H. Schmidt, E. Dammann, and C. H. Schatterny, “The needle sensor—a micromechanical detector for atomic force microscopy,” *Int. J. Optoelectron.* **8**, 669 (1993).
- <sup>14</sup>K. Bartzke, T. Antrack, K. Besocke, and E. Dammann, “Arrangement for determining the topography of a surface,” German Patent and Trademark Office, Patent DE 19513529A1 (1995).

- <sup>15</sup>S. Baumann, I. G. Rau, S. Loth, C. P. Lutz, and A. J. Heinrich, "Measuring the three-dimensional structure of ultrathin insulating films at the atomic scale," *ACS Nano* **8**, 1739 (2014).
- <sup>16</sup>M. Z. Baykara, H. Todorovic, H. Mönig, T. C. Schwendemann, O. Uenverdi, L. Rodrigo, E. I. Altman, R. Perez, and U. Schwarz, "Atom-specific forces and defect identification on surface-oxidized Cu(100) with combined 3D-AFM and STM measurements," *Phys. Rev. B* **87**, 155414 (2013).
- <sup>17</sup>M. Z. Baykara, H. Mönig, T. C. Schwendemann, Ö. Ünverdi, E. I. Altman, and U. D. Schwarz, *Appl. Phys. Lett.* **108**, 071601 (2016).
- <sup>18</sup>J. Berwanger, F. Huber, F. Stip, and F. J. Giessibl, "Lateral manipulation with combined atomic force and scanning tunneling microscopy using CO-terminated tips," *Phys. Rev. B* **98**, 195409 (2018).
- <sup>19</sup>A. Bettac, J. Koeble, K. Winkler, B. Uder, M. Maier, and A. Feltz, "QPlus: Atomic force microscopy on single-crystal insulators with small oscillation amplitudes at 5 K," *Nanotechnology* **20**, 264009 (2009).
- <sup>20</sup>H. Bielefeldt and F. J. Giessibl, "A simplified but intuitive analytical model for intermittent-contact-mode force microscopy based on Hertzian mechanics," *Surf. Sci.* **440**, L863 (1999).
- <sup>21</sup>G. Binnig, H. Rohrer, Ch. Gerber, and E. Weibel, "Tunneling through a controllable vacuum gap," *Appl. Phys. Lett.* **40**, 178 (1982).
- <sup>22</sup>G. Binnig, H. Rohrer, Ch. Gerber, and E. Weibel, "7 × 7 reconstruction on Si(111) resolved in real space," *Phys. Rev. Lett.* **50**, 120 (1983).
- <sup>23</sup>G. Binnig and H. Rohrer, "Nobel lecture: Scanning tunneling microscopy—From birth to adolescence," *Rev. Mod. Phys.* **59**, 615 (1987).
- <sup>24</sup>G. Binnig, "Atomic force microscope and method for imaging surfaces with atomic resolution," U.S. Patent No 4,724,318 (26 November 1985).
- <sup>25</sup>G. Binnig, C. F. Quate, and Ch. Gerber, "Atomic force microscope," *Phys. Rev. Lett.* **56**, 930 (1986).
- <sup>26</sup>G. Binnig and D. P. E. Smith, "Single-tube three-dimensional scanner for scanning tunneling microscopy," *Rev. Sci. Instrum.* **57**, 1688 (1986).
- <sup>27</sup>F. Bischoff, Y. He, A. Riss, K. Seufert, W. Auwärter, and J. V. Barth, "Exploration of interfacial porphine coupling schemes and hybrid systems by bond-resolved scanning probe microscopy," *Angew. Chem.* **57**, 16030 (2018).
- <sup>28</sup>M. P. Boneschanscher, J. van der Lit, Z. Sun, I. Swart, P. Liljeroth, and D. Vanmaekelbergh, "Quantitative atomic resolution force imaging on epitaxial graphene with reactive and nonreactive AFM probes," *ACS Nano* **6**, 10216 (2012).
- <sup>29</sup>C. Büchner, L. Lichtenstein, X. Yu, A. Boscoboinik, B. Yang, W. E. Kaden, M. Heyde, S. K. Shaikhutdinov, R. Włodarczyk, M. Sierka, J. Sauer, and H.-J. Freund, "Ultrathin silica films: The atomic structure of two-dimensional crystals and glasses," *Chem. - Eur. J.* **20**, 9176 (2014).
- <sup>30</sup>N. Burnham and R. J. Colton, "Measuring the nanomechanical and surface forces of materials using the atomic force microscope," *J. Vac. Sci. Technol., A* **7**, 2906 (1989).
- <sup>31</sup>L. Canale, A. Laborieux, A. Aroul Mogane, L. Jubin, J. Comtet, A. Laine, L. Bocquet, A. Siria, and A. Nigues, "MicroMegascopes," *Nanotechnology* **29**, 355501 (2018).
- <sup>32</sup>See [www.ceramtec.de](http://www.ceramtec.de) for CeramTec GmbH, CeramTec-Weg 1, D-95615 Marktredwitz, Germany.
- <sup>33</sup>C. J. Chen, *Introduction to Scanning Tunneling Microscopy* (Oxford University Press, New York, Oxford, 1993).
- <sup>34</sup>C. Chiutu, A. M. Sweetman, A. J. Lakin, A. Stannard, S. Jarvis, L. Kantorovich, J. L. Dunn, and P. Moriarty, "Precise orientation of a single C-60 molecule on the tip of a scanning probe microscope," *Phys. Rev. Lett.* **108**, 268302 (2012).
- <sup>35</sup>J. P. Cleveland, B. Anczykowski, A. E. Schmid, and V. B. Elings, "Energy dissipation in tapping-mode atomic force microscopy," *Appl. Phys. Lett.* **72**, 2613 (1998).
- <sup>36</sup>See <http://creativecommons.org/licenses/by/4.0> for information on terms of creative common licenses.
- <sup>37</sup>O. E. Dagdeviren and U. D. Schwarz, "Optimizing qPlus sensor assemblies for simultaneous scanning tunneling and noncontact atomic force microscopy operation based on finite element method analysis," *Beilstein J. Nanotechnol.* **8**, 657 (2017).
- <sup>38</sup>F. de Faria Elsner, "Untersuchung der rauchgrenzen bei der messung kleiner mechanischer auslenkungen," Diploma thesis, University of Regensburg, Germany, 2010.
- <sup>39</sup>B. de la Torre, M. Švec, G. Foti, O. Krejčí, P. Hapala, A. Garcia-Lekue, T. Frederiksen, R. Zbořil, A. Arnau, H. Vázquez, and P. Jelínek, "Submolecular resolution by variation of the inelastic electron tunneling spectroscopy amplitude and its relation to the AFM/STM signal," *Phys. Rev. Lett.* **119**, 166001 (2017).
- <sup>40</sup>B. de la Torre, M. Švec, P. Hapala, J. Redondo, O. Krejci, R. Lo, D. Manna, A. Sarmah, D. Nachtigallova, J. Tucek, P. Blonski, M. Otyepka, R. Zboril, P. Hobza, and P. Jelinek, "Non-covalent control of spin-state in metal-organic complex by positioning on N-doped graphene," *Nat. Commun.* **9**, 2831 (2018).
- <sup>41</sup>W. Denk and D. W. Pohl, "Local electrical dissipation imaged by scanning force microscopy," *Appl. Phys. Lett.* **59**, 2171 (1991).
- <sup>42</sup>D. G. de Oteyza, P. Gorman, Y.-C. Chen, S. Wickenburg, A. Riss, D. J. Mowbray, G. Etkin, Z. Pedramrazi, H.-Z. Tsai, A. Rubio, M. F. Crommie, and F. R. Fischer, "Direct imaging of covalent bond structure in single-molecule chemical reactions," *Science* **340**, 1434 (2013).
- <sup>43</sup>Detector noise—Note. In previous works [Eq. (2.43) in Ref. 167, Eq. (51) in Ref. 86], a factor 2 was erroneously missing - we have to consider that the actual deflection rms error is up to  $\pm n_q B^{1/2}$ .
- <sup>44</sup>U. Diebold, "The surface science of titanium dioxide," *Surf. Sci. Rep.* **48**, 53 (2003).
- <sup>45</sup>K. Dransfeld, P. Guethner, and K. Heitmann, "Acoustic screen scan microscope for the examination of an object in the short-range field of a resonant acoustic oscillator," United States Patent and Trademark Office, U.S. Patent 5,212,987 (16 June 1988).
- <sup>46</sup>U. Dürig, J. K. Gimzewski, and D. W. Pohl, "Experimental observation of forces acting during scanning tunneling microscopy," *Phys. Rev. Lett.* **57**, 2403 (1986).
- <sup>47</sup>U. Dürig, O. Züger, and A. Stalder, "Interaction force detection in scanning probe microscopy: Methods and applications," *J. Appl. Phys.* **72**, 1778 (1992).
- <sup>48</sup>U. Dürig, H. R. Steinauer, and N. Blanc, "Dynamic force microscopy by means of the phase-controlled oscillator method," *J. Appl. Phys.* **82**, 3641 (1997).
- <sup>49</sup>U. Dürig, "Interaction sensing in dynamic force microscopy," *New J. Phys.* **2**, 5 (2000).
- <sup>50</sup>T. Eguchi and Y. Hasegawa, "High resolution atomic force microscopic imaging of the Si(111)-(7 × 7) surface: Contribution of short-range force to the images," *Phys. Rev. Lett.* **89**, 266105 (2002).
- <sup>51</sup>D. M. Eigler and E. K. Schweizer, "Positioning single atoms with a scanning tunnelling microscope," *Nature* **344**, 524 (1990).
- <sup>52</sup>M. Emmrich, M. Schneiderbauer, F. Huber, A. J. Weymouth, N. Okabayashi, and F. J. Giessibl, "Force field analysis suggests a lowering of diffusion barriers in atomic manipulation due to presence of STM tip," *Phys. Rev. Lett.* **114**, 146101 (2015).
- <sup>53</sup>M. Emmrich, F. Huber, F. Pielmeier, J. Welker, T. Hofmann, M. Schneiderbauer, D. Meuer, S. Polesya, S. Mankovsky, D. Ködderitzsch, H. Ebert, and F. J. Giessibl, "Subatomic resolution force microscopy reveals internal structure and adsorption sites of small iron clusters," *Science* **348**, 308 (2015).
- <sup>54</sup>Epoxy Technology, Inc., 14 Fortune Drive, Billerica, MA 01821-3972, USA.
- <sup>55</sup>T. Esat, N. Friedrich, F. S. Tautz, and R. Temirov, "A standing molecule as a single-electron field emitter," *Nature* **558**, 573 (2018).
- <sup>56</sup>A. Extance, "The atomic-force revolution," *Nature* **555**, 545 (2018).
- <sup>57</sup>A. Extance, "New AFM tip reopens hydrogen bond imaging debate," in *Chemistry World* (April 11, 2018), <https://www.chemistryworld.com/news/new-afm-tip-reopens-hydrogen-bond-imaging-debate/3008878.article>.
- <sup>58</sup>S. Fatayer, N. B. Poddar, S. Quiroga, F. Schulz, B. Schuler, S. V. Kalpathy, G. Meyer, D. Perez, E. Guitian, D. Pena, M. J. Wornat, and L. Gross, "Atomic force microscopy identifying fuel pyrolysis products and directing the synthesis of analytical standards," *J. Am. Chem. Soc.* **140**, 8156 (2018).

- <sup>59</sup>S. Fatayer, A. I. Coppola, F. Schulz, B. D. Walker, T. A. Broek, G. Meyer, R. Ellen, M. Druffel, M. McCarthy, and L. Gross, "Direct visualization of individual aromatic compound structures in low molecular weight marine dissolved organic carbon," *Geophys. Res. Lett.* **45**, 5590, <https://doi.org/10.1029/2018gl077457> (2018).
- <sup>60</sup>Femto HQA-15M-10T, Femto GmbH, Berlin, Germany.
- <sup>61</sup>R. P. Feynman, "There's plenty of room at the bottom," in *An Invitation to Enter a New Field of Physics was a Lecture Given at the Annual American Physical Society Meeting at Caltech On December 29, 1959*, Reprinted [*J. Microelectromech. Syst.* **1**, 60 (1992)].
- <sup>62</sup>R. P. Feynman, R. B. Leighton, and M. Sands, *The Feynman Lectures on Physics* (Addison Wesley Publishing Company, Reading, MD, USA, 1964).
- <sup>63</sup>N. Fournier, C. Wagner, C. Weiss, R. Temirov, and F. S. Tautz, "Force-controlled lifting of molecular wires," *Phys. Rev. B* **84**, 035435 (2011).
- <sup>64</sup>R. Garcia and R. Perez, "Dynamic atomic force microscopy methods," *Surf. Sci. Rep.* **47**, 197 (2002).
- <sup>65</sup>R. Garcia and E. T. Herruzo, "The emergence of multifrequency force microscopy," *Nat. Nanotechnol.* **7**, 217 (2012).
- <sup>66</sup>M. F. B. Green, T. Esat, C. Wagner, P. Leinen, A. Grötsch, F. Stefan Tautz, and R. Temirov, "Patterning a hydrogen-bonded molecular monolayer with a hand-controlled scanning probe microscope," *Beilstein J. Nanotechnol.* **5**, 1926 (2014).
- <sup>67</sup>M. F. B. Green, C. Wagner, P. Leinen, T. Deilmann, P. Krüger, M. Rohlfing, F. Stefan Tautz, and R. Temirov, "Scanning quantum dot microscopy: A quantitative method to measure local electrostatic potential near surfaces," *Jpn. J. Appl. Phys., Part 1* **55**, 08NA04 (2016).
- <sup>68</sup>F. J. Giessibl and G. Binnig, "Investigation of the (001) cleavage plane of potassium bromide with an atomic force microscope at 4.2 K in ultra-high vacuum," *Ultramicroscopy* **42-44**, 281 (1992).
- <sup>69</sup>F. J. Giessibl, "Atomic force microscopy in ultrahigh vacuum," *Jpn. J. Appl. Phys., Part 1* **33**, 3726 (1994).
- <sup>70</sup>F. J. Giessibl and B. Trafts, "Piezoresistive cantilevers utilized for scanning tunneling and scanning force microscope in ultrahigh vacuum," *Rev. Sci. Instrum.* **65**, 1923 (1994).
- <sup>71</sup>F. J. Giessibl, "Atomic resolution of the silicon (111)-7 × 7 surface by atomic force microscopy," *Science* **267**, 68 (1995).
- <sup>72</sup>F. J. Giessibl, "Vorrichtung zum berührungslosen abtasten von oberflächen und verfahren dafür," German Patent and Trademark Office, Patent DE 19633546 (20 April 2000).
- <sup>73</sup>F. J. Giessibl, "Device for noncontact/intermittent contact scanning of a surface and process therefore," US Patent and Trademark Office, U.S. Patent US 6240771 (6 June 2001).
- <sup>74</sup>F. J. Giessibl, "Sensor zum berührungslosen abtasten einer oberfläche," German Patent and Trademark Office, Patent DE 10 2010052037 (18 April 2013).
- <sup>75</sup>F. J. Giessibl, "Sensor for noncontact profiling of a surface," US Patent and Trademark Office, US patent 8393009 (5 March 2013).
- <sup>76</sup>F. J. Giessibl, "Sensor for noncontact profiling of a surface," Chinese Patent and Trademark Office, Chinese Patent Registration No. CN102662085A, Granted October 28 2015 under Patent No. ZL201110373640.3 (28 October 2015).
- <sup>77</sup>F. J. Giessibl, "Registered trademark 'QPLUS' (wordmark)," US Patent and Trademark Office, US Serial No. 77788740, Registration No. 3918525, Registration Date 15 February 2011.
- <sup>78</sup>F. J. Giessibl, "Forces and frequency shifts in atomic-resolution dynamic-force microscopy," *Phys. Rev. B* **56**, 16010 (1997).
- <sup>79</sup>F. J. Giessibl, "High-speed force sensor for force microscopy and profilometry utilizing a quartz tuning fork," *Appl. Phys. Lett.* **73**, 3956 (1998).
- <sup>80</sup>F. J. Giessibl, H. Bielefeldt, S. Hembacher, and J. Mannhart, "Calculation of the optimal imaging parameters for frequency modulation atomic force microscopy," *Appl. Surf. Sci.* **140**, 352 (1999).
- <sup>81</sup>F. J. Giessibl, "Atomic resolution on Si (111)-(7 × 7) by noncontact atomic force microscopy with a force sensor based on a quartz tuning fork," *Appl. Phys. Lett.* **76**, 1470 (2000).
- <sup>82</sup>F. J. Giessibl, S. Hembacher, H. Bielefeldt, and J. Mannhart, "Subatomic features on the silicon (111)-(7 × 7) surface observed by atomic force microscopy," *Science* **289**, 422 (2000).
- <sup>83</sup>F. J. Giessibl and H. Bielefeldt, "Physical interpretation of frequency-modulation atomic force microscopy," *Phys. Rev. B* **61**, 9968 (2000).
- <sup>84</sup>F. J. Giessibl, "A direct method to calculate tip-sample forces from frequency shifts in frequency-modulation atomic force microscopy," *Appl. Phys. Lett.* **78**, 123 (2001).
- <sup>85</sup>F. J. Giessibl, M. Herz, and J. Mannhart, "Friction traced to the single atom," *Proc. Natl. Acad. Sci. U. S. A.* **99**, 12006 (2002).
- <sup>86</sup>F. J. Giessibl, "Advances in atomic force microscopy," *Rev. Mod. Phys.* **75**, 949 (2003).
- <sup>87</sup>F. J. Giessibl, S. Hembacher, M. Herz, Ch. Schiller, and J. Mannhart, "Stability considerations and implementation of cantilevers allowing dynamic force microscopy with optimal resolution: The qPlus sensor," *Nanotechnology* **15**, S79 (2004).
- <sup>88</sup>F. J. Giessibl, "AFM's path to atomic resolution," *Mater. Today* **8**, 32 (2005).
- <sup>89</sup>F. J. Giessibl and M. Reichling, "Investigating atomic details of the CaF<sub>2</sub>(111) surface with a qPlus sensor," *Nanotechnology* **16**, S118 (2005).
- <sup>90</sup>F. J. Giessibl, C. P. Lutz, and A. Heinrich, unpublished data using the traditional Eigler walker STM that was transformed to AFM by adding a qPlus sensor, recorded on June 22 2007.
- <sup>91</sup>F. J. Giessibl, "Higher-harmonic atomic force microscopy," *Surf. Interface Anal.* **38**, 1696 (2006).
- <sup>92</sup>F. J. Giessibl, F. Pielmeier, T. Eguchi, T. An, and Y. Hasegawa, "Comparison of force sensors for atomic force microscopy based on quartz tuning forks and length-extensional resonators," *Phys. Rev. B* **84**, 125409 (2011).
- <sup>93</sup>M. Granovskij, A. Schrön, and F. Bechstedt, "Magnetic exchange force microscopy from first principles: Application to the antiferromagnetic NiO(001) surface," *New J. Phys.* **16**, 023020 (2014).
- <sup>94</sup>L. Gross, F. Mohn, P. Liljeroth, J. Repp, F. J. Giessibl, and G. Meyer, "Measuring the charge state of an adatom with noncontact atomic force microscopy," *Science* **324**, 1428 (2009).
- <sup>95</sup>L. Gross, F. Mohn, N. Moll, P. Liljeroth, and G. Meyer, "The chemical structure of a molecule resolved by atomic force microscopy," *Science* **325**, 1110 (2009).
- <sup>96</sup>L. Gross, F. Mohn, N. Moll, G. Meyer, R. Ebel, W. M. Abdel-Mageed, and M. Jaspars, "Organic structure determination using atomic-resolution scanning probe microscopy," *Nat. Chem.* **2**, 821 (2010).
- <sup>97</sup>L. Gross, F. Mohn, N. Moll, B. Schuler, A. Criado, E. Guitian, D. Pena, A. Gourdon, and G. Meyer, "Bond-order discrimination by atomic force microscopy," *Science* **337**, 1326 (2012).
- <sup>98</sup>L. Gross, B. Schuler, N. Pavlicek, S. Fatayer, Z. Majzik, N. Moll, D. Pena, and G. Meyer, "Atomic force microscopy for molecular structure elucidation," *Angew. Chem., Int. Ed.* **57**, 3888 (2018).
- <sup>99</sup>P. Güthner, U. Fischer, and K. Dransfeld, "Scanning near-field acoustic microscopy," *Appl. Phys. B: Photophys. Laser Chem.* **48**, 89 (1989).
- <sup>100</sup>U. Gysin, S. Rast, P. Ruff, E. Meyer, D. W. Lee, P. Vettiger, and C. Gerber, "Temperature dependence of the force sensitivity of silicon cantilevers," *Phys. Rev. B* **69**, 045403 (2004).
- <sup>101</sup>S. K. Hämäläinen, N. van der Heijden, J. van der Lit, S. den Hartog, P. Liljeroth, and I. Swart, "Intermolecular contrast in atomic force microscopy images without intermolecular bonds," *Phys. Rev. Lett.* **113**, 186102 (2014).
- <sup>102</sup>K. O. Hanssen, B. Schuler, A. Williams, T. B. Demissie, E. Hansen, J. H. Andersen, J. Svenson, K. Blinov, M. Repisky, F. Mohn, G. Meyer, J.-S. Svendsen, R. Ruud, M. Elyashberg, L. Gross, M. Jaspars, and J. Isaksson, "A combined atomic force microscopy and computational approach for structural elucidation of breifussin A and B, highly modified halogenated dipeptides from the arctic hydrozoan Thuiaria breifussi," *Angew. Chem., Int. Ed.* **51**, 12238 (2012).
- <sup>103</sup>P. Hapala, G. Kichin, C. Wagner, F. Stefan Tautz, R. Temirov, and P. Jelinek, "Mechanism of high-resolution STM/AFM imaging with functionalized tips," *Phys. Rev. B* **90**, 085421 (2014).
- <sup>104</sup>M. Z. Hasan and C. L. Kane, "Colloquium: Topological insulators," *Rev. Mod. Phys.* **82**, 3045 (2010).



- <sup>105</sup>Y. Hasegawa, T. Eguchi, T. An, M. Ono, K. Akiyama, and T. Sakurai, "Calculation of noise intensity in the frequency demodulation for atomic force microscopy," *Jpn. J. Appl. Phys., Part 2* **43**, L303 (2004).
- <sup>106</sup>N. Hauptmann, M. Dupe, T. C. Hung, A. K. Lemmens, D. Wegner, B. Dupe, and A. A. Khajetoorians, "Revealing the correlation between real-space structure and chiral magnetic order at the atomic scale," *Phys. Rev. B* **97**, 100401 (2018).
- <sup>107</sup>Y. He, M. Garnica, F. Bischoff, J. Dücke, M.-L. Bocquet, M. Batzill, W. Auwärter, and J. V. Barth, "Fusing tetrapyrroles to graphene edges by surface-assisted covalent coupling," *Nat. Chem.* **9**, 33 (2016).
- <sup>108</sup>J. Augustin Hedberg, "Low temperature force microscopy on a deeply embedded two dimensional electron gas," Ph.D. thesis, McGill University, Montréal, Québec, Canada, 2011, <https://drive.google.com/file/d/0B-2ISu5F0W9UN2I4ZEIOZGM4SIVnNDJMqZBLREJLSdNYT0hj/view>.
- <sup>109</sup>J. Hellerstedt, A. Cahlik, Š. Martin, B. de la Torre, M. Moro-Lagares, T. Chutora, B. Papoušková, G. Zoppellaro, P. Mutombo, M. Ruben, R. Zbořil, and P. Jelinek, "On-surface structural and electronic properties of spontaneously formed Tb<sub>2</sub>Pc<sub>3</sub> single molecule magnets," *Nanoscale* **10**, 15553 (2018).
- <sup>110</sup>S. Hembacher, F. J. Giessibl, and J. Mannhart, "Evaluation of a force sensor based on a quartz tuning fork for operation at low temperatures and ultrahigh vacuum," *Appl. Surf. Sci.* **188**, 445 (2002).
- <sup>111</sup>S. Hembacher, F. J. Giessibl, J. Mannhart, and C. F. Quate, "Revealing the hidden atom in graphite by low-temperature atomic force microscopy," *Proc. Natl. Acad. Sci. U. S. A.* **100**, 12539 (2003).
- <sup>112</sup>S. Hembacher, F. J. Giessibl, and J. Mannhart, "Force microscopy with light-atom probes," *Science* **305**, 380 (2004).
- <sup>113</sup>S. Hembacher, F. J. Giessibl, J. Mannhart, and C. F. Quate, "Local spectroscopy and atomic imaging of tunneling current, forces and dissipation on graphite," *Phys. Rev. Lett.* **94**, 056101 (2005).
- <sup>114</sup>M. Herz, F. J. Giessibl, and J. Mannhart, "Probing the shape of atoms in real space," *Phys. Rev. B* **68**, 045301 (2003).
- <sup>115</sup>M. Herz, Ch. Schiller, F. J. Giessibl, and J. Mannhart, "Simultaneous current-, force-, and work function measurement with atomic resolution," *Appl. Phys. Lett.* **86**, 153101 (2005).
- <sup>116</sup>J. E. Hirsch, "Proposed experimental test of an alternative electrodynamic theory of superconductors," *Physica C* **508**, 21 (2015).
- <sup>117</sup>H. Hölscher, S. M. Langkat, A. Schwarz, and R. Wiesendanger, "Measurement of three-dimensional force fields with atomic resolution using dynamic force spectroscopy," *Appl. Phys. Lett.* **81**, 4428 (2002).
- <sup>118</sup>W. A. Hofer, A. S. Foster, and A. L. Shluger, "Theories of scanning probe microscopes at the atomic scale," *Rev. Mod. Phys.* **75**, 1287 (2003).
- <sup>119</sup>T. Hofmann, J. Welker, and F. J. Giessibl, "Preparation of light-atom tips for scanning probe microscopy by explosive delamination," *J. Vac. Sci. Technol., B: Nanotechnol. Microelectron.: Mater., Process., Meas., Phenom.* **28**, C4E28 (2010).
- <sup>120</sup>T. Hofmann, "Hochauflösende Rasterkraftmikroskopie auf Graphen und Kohlenmonoxid," *Dissertationsreihe Physik, Universität Regensburg* (2014), available at <https://epubl-uni-regensburg.de/29735/1/hofmann.pdf>.
- <sup>121</sup>T. Hofmann, F. Pielmeier, and F. J. Giessibl, "Chemical and crystallographic characterization of the tip apex in scanning probe microscopy," *Phys. Rev. Lett.* **112**, 066101 (2014).
- <sup>122</sup>I. Horcas, R. Fernández, J. M. Gómez-Rodríguez, J. Colchero, J. Gómez-Herrero, and A. M. Baro, "WSXM: A software for scanning probe microscopy and a tool for nanotechnology," *Rev. Sci. Instrum.* **78**, 013705 (2007).
- <sup>123</sup>M. Huang, M. Čuma, and F. Liu, "Seeing the atomic orbital: First-principles study of the effect of tip termination on atomic force microscopy," *Phys. Rev. Lett.* **90**, 256101 (2003).
- <sup>124</sup>F. Huber, S. Matencio, A. J. Weymouth, C. Ocal, E. Barrera, and F. J. Giessibl, "Intramolecular force contrast and dynamic current-distance measurements at room temperature," *Phys. Rev. Lett.* **115**, 066101 (2015).
- <sup>125</sup>F. Huber and F. J. Giessibl, "Low noise current preamplifier for qPlus sensor deflection signal detection in atomic force microscopy at room and low temperatures," *Rev. Sci. Instrum.* **88**, 073702 (2017).
- <sup>126</sup>T. Huff, H. Labidi, M. Rashidi, L. Livadaru, T. Dienel, R. Achal, W. Vine, J. Pitters, and R. A. Wolkow, "Binary atomic silicon logic," *Nat. Electron.* **1**, 636 (2018).
- <sup>127</sup>H. J. Hug, M. A. Lantz, A. Abdurixit, P. J. A. van Schendel, R. Hoffmann, P. Kappenberger, A. Baratoft, reply by F. J. Giessibl, S. Hembacher, H. Bielefeldt, and J. Mannhart, "Subatomic features in atomic force microscopy images," *Science* **291**, 2509 (2001).
- <sup>128</sup>See <https://hypertextbook.com/facts/2004/JennelleBaptiste.shtml> for Resistivity of Gold, in The Physics Factbook.
- <sup>129</sup>T. Ichii, M. Fujimura, M. Negami, K. Murase, and H. Sugimura, "Frequency modulation atomic force microscopy in ionic liquid using quartz tuning fork sensors," *Jpn. J. Appl. Phys., Part 1* **51**, 08KB08 (2012).
- <sup>130</sup>W. Isaacson, "Leonardo da Vinci" (Simon & Schuster, 2017).
- <sup>131</sup>J. Israelachvili, *Intermolecular and Surface Forces*, 3rd ed. (Elsevier, Oxford, 2011).
- <sup>132</sup>P. H. Jacobse, A. Komouche, T. Gebraad, M. M. Ervasti, J. M. Thijssen, P. Liljeroth, and I. Swart, "Electronic components embedded in a single graphene nanoribbon," *Nat. Commun.* **8**, 119 (2017).
- <sup>133</sup>C. L. Jahnke, O. Brandt, K. E. Fellows, and H. D. Hallen, "Choosing a preamplifier for tuning fork signal detection in scanning force microscopy," *Rev. Sci. Instrum.* **75**, 2759 (2004).
- <sup>134</sup>S. P. Jarvis, A. M. Sweetman, I. Lekkas, N. R. Champness, L. Kantorovich, and P. Moriarty, "Simulated structure and imaging of NTCDI on Si(111)-7 × 7: A combined STM, NC-AFM and DFT study," *J. Phys.: Condens. Matter* **27**, 054004 (2015).
- <sup>135</sup>U. Kaiser, A. Schwarz, and R. Wiesendanger, "Magnetic exchange force microscopy with atomic resolution," *Nature* **446**, 522 (2007).
- <sup>136</sup>K. Karrai and R. D. Grober, "Piezoelectric tip-sample distance control for near field optical microscopes," *Appl. Phys. Lett.* **66**, 1842 (1995).
- <sup>137</sup>K. Karrai and I. Tiemann, "Interfacial shear force microscopy," *Phys. Rev. B* **62**, 13174 (2000).
- <sup>138</sup>S. Kawai, S. Saito, S. Osumi, S. Yamaguchi, A. S. Foster, P. Spijker, and E. Meyer, "Atomically controlled substitutional boron-doping of graphene nanoribbons," *Nat. Commun.* **6**, 8098 (2015).
- <sup>139</sup>S. Kawai, A. S. Foster, T. Björkman, S. Nowakowska, J. Björk, F. Federici Canova, L. H. Gade, T. A. Jung, and E. Meyer, "Van der Waals interactions and the limits of isolated atom models at interfaces," *Nat. Commun.* **7**, 11559 (2016).
- <sup>140</sup>S. Kawai, A. Benassi, E. Gnecco, H. Söde, R. Pawlak, K. Mullen, D. Passerone, C. Pignedoli, P. Ruffieux, R. Fasel, and E. Meyer, "Superlubricity of graphene nanoribbons on gold surfaces," *Science* **351**, 957 (2016).
- <sup>141</sup>S. Kawai, T. Nishiuchi, T. Kodama, P. Spijker, R. Pawlak, T. Meier, J. Tracey, T. Kubo, E. Meyer, and A. S. Foster, "Direct quantitative measurement of the C=O...H-C bond by atomic force microscopy," *Sci. Adv.* **3**, e1603258 (2017).
- <sup>142</sup>S. Kawai, S. Nakatsuka, T. Hatakeyama, R. Pawlak, T. Meier, J. Tracey, E. Meyer, and A. S. Foster, "Multiple heteroatom substitution to graphene nanoribbon," *Sci. Adv.* **4**, eaar7181 (2018).
- <sup>143</sup>B. Kim, S. Kwon, M. Lee, Q. H. Kim, S. An, and W. Jhe, "Probing nonlinear rheology layer-by-layer in interfacial hydration water," *Proc. Natl. Acad. Sci. U. S. A.* **112**, 15619 (2015).
- <sup>144</sup>E. Kleinbaum and G. A. Csathy, *Rev. Sci. Instrum.* **83**, 126101 (2012).
- <sup>145</sup>N. Klimov, S. Jung, S. Zhu, T. Li, C. Wright, S. Solares, D. Newell, N. Zhitenev, and J. Strosio, "Electromechanical properties of graphene drumheads," *Science* **336**, 1557 (2012).
- <sup>146</sup>K. Kobayashi, H. Yamada, and K. Matsushige, "Frequency noise in frequency modulation atomic force microscopy," *Rev. Sci. Instrum.* **80**, 043708 (2009).
- <sup>147</sup>M. Koch, Z. Li, C. Nacci, T. Kumagai, I. Franco, and L. Grill, "How structural defects affect the mechanical and electrical properties of single molecular wires," *Phys. Rev. Lett.* **121**, 047701 (2018).
- <sup>148</sup>Kolibri-Preampl, SPECS GmbH, Berlin, Germany.
- <sup>149</sup>J. Lambe and R. C. Jaklevic, "Molecular vibration spectra by inelastic electron tunneling," *Phys. Rev.* **165**, 821 (1968).
- <sup>150</sup>M. A. Lantz, H. J. Hug, P. J. A. van Schendel, R. Hoffmann, S. Martin, A. Baratoft, A. Abdurixit, H.-J. Güntherodt, and Ch. Gerber, "Low

temperature scanning force microscopy of the Si(111)-(7 × 7) surface," *Phys. Rev. Lett.* **84**, 2642 (2000).

<sup>151</sup>M. A. Lantz, H. J. Hug, R. Hoffmann, P. J. A. van Schendel, P. Kappenberger, S. Martin, A. Baratoff, and H.-J. Güthner, "Quantitative measurement of short-range chemical bonding forces," *Science* **291**, 2580 (2001).

<sup>152</sup>K. Lee, Q. Kim, S. An, J. An, J. Kim, B. Kim, and W. Jhe, "Superwetting of TiO<sub>2</sub> by light-induced water-layer growth via delocalized surface electrons," *Proc. Natl. Acad. Sci. U. S. A.* **111**, 5784 (2014).

<sup>153</sup>M. Lee, B. Kim, J. Kim, and W. Jhe, "Noncontact friction via capillary shear interaction at nanoscale," *Nat. Commun.* **6**, 7359 (2015).

<sup>154</sup>P. Leinen, M. F. B. Green, T. Esat, C. Wagner, F. Stefan Tautz, and R. Temirov, "Virtual reality visual feedback for hand-controlled scanning probe microscopy manipulation of single molecules," *Beilstein J. Nanotechnol.* **6**, 2148 (2015).

<sup>155</sup>P. Leinen, M. F. B. Green, T. Esat, C. Wagner, F. Stefan Tautz, and R. Temirov, "Hand controlled manipulation of single molecules via a scanning probe microscope with a 3D virtual reality interface," *J. Visualized Exp.* **116**, e54506 (2016).

<sup>156</sup>N. Li, X. Chen, and Qi-K. Xue, "Contribution of chemical bonding to the force in atomic force microscopy," *Acta Phys.-Chim. Sin.* **30**, 205 (2014).

<sup>157</sup>A. Liebig, A. Peronio, D. Meuer, A. J. Weymouth, and F. J. Giessibl, "Atomic force microscopy with atomically-engineered tips provides up to 99.8% agreement between experiment and elementary electrostatics" (unpublished).

<sup>158</sup>H.-Q. Mao, X. Chen, and Qi-K. Xue, "Modulation of step heights of thin Pb films by the quantum size effect observed by non-contact atomic force microscopy," *Chin. Phys. Lett.* **29**, 066802 (2012).

<sup>159</sup>G. Meyer and N. M. Amer, "Novel optical approach to atomic force microscopy," *Appl. Phys. Lett.* **53**, 1045 (1988).

<sup>160</sup>G. Meyer and N. M. Amer, "Optical-beam-deflection atomic force microscopy: The NaCl (001) surface," *Appl. Phys. Lett.* **56**, 2100 (1990).

<sup>161</sup>G. Meyer and N. M. Amer, "Simultaneous measurement of lateral and normal forces with an optical-beam-deflection atomic force microscope," *Appl. Phys. Lett.* **57**, 2089 (1990).

<sup>162</sup>J. Melcher, J. Stirling, and G. A. Shaw, "A simple method for the determination of qPlus sensor spring constants," *Beilstein J. Nanotechnol.* **6**, 1733 (2015).

<sup>163</sup>Microcrystal product brochure on quartz resonators, Micro Crystal AG, Mühlestrasse 14, CH-2540 Grenchen, Switzerland.

<sup>164</sup>H. Mönig, M. Todorovic, M. Z. Baykara, T. C. Schwendemann, L. Rodrigo, E. I. Altman, R. Perez, and U. Schwarz, "Understanding scanning tunneling microscopy contrast mechanisms on metal oxides: A case study," *ACS Nano* **7**, 10233 (2013).

<sup>165</sup>H. Mönig, S. Amirjalayer, A. Timmer, Z. Hu, L. Liu, O. Diaz Arado, M. Cnudde, C. Alejandro Strassert, W. Ji, M. Rohlfing, and H. Fuchs, "Quantitative assessment of intermolecular interactions by atomic force microscopy imaging using copper oxide tips," *Nat. Nanotechnol.* **13**, 371 (2018).

<sup>166</sup>F. Mohn, B. Schuler, L. Gross, and G. Meyer, "Different tips for high-resolution atomic force microscopy and scanning tunneling microscopy of single molecules," *Appl. Phys. Lett.* **102**, 073109 (2013).

<sup>167</sup>*Noncontact Atomic Force Microscopy*, edited by S. Morita, R. Wiesendanger, and E. Meyer (Springer, New York, 2002).

<sup>168</sup>*Noncontact Atomic Force Microscopy: Volume 2*, edited by S. Morita, F. J. Giessibl, and R. Wiesendanger (Springer, New York, 2009).

<sup>169</sup>*Noncontact Atomic Force Microscopy: Volume 3*, edited by S. Morita, F. J. Giessibl, E. Meyer, and R. Wiesendanger (Springer, New York, 2015).

<sup>170</sup>E. Momoaki and Sh. Kogure, in *Piezoelectricity*, edited by G. W. Taylor, J. J. Gagnepain, T. R. Meeker, T. Nakamura, and L. A. Shuvalov (Gordon and Breach, New York, 1985), pp. 47–60.

<sup>171</sup>G. Münnich, A. Donarini, M. Wenderoth, and J. Repp, "Fixing the energy scale in scanning tunneling microscopy on semiconductor surfaces," *Phys. Rev. Lett.* **111**, 216802 (2013).

<sup>172</sup>K. Mukasa, H. Hasegawa, Y. Tazuke, K. Sueoka, M. Sasaki, and K. Hayakawa, "Exchange interaction between magnetic moments of ferromagnetic sample and tip: Possibility of atomic-resolution images of

exchange interactions using exchange force microscopy," *Jpn. J. Appl. Phys., Part 1* **33**, 2692 (1994).

<sup>173</sup>Nanonis—SPECS Zurich GmbH, 8005 Zurich, Switzerland.

<sup>174</sup>M. Neu, N. Moll, L. Gross, G. Meyer, F. J. Giessibl, and J. Repp, "Image correction for atomic force microscopy images with functionalized tips," *Phys. Rev. B* **89**, 205407 (2014).

<sup>175</sup>New England Wire Technologies, 130 North Main Street, Lisbon, NH 03585, USA.

<sup>176</sup>K. Hvidtfelt Nielsen, "Nanotech, blur and tragedy in recent artworks by Gerhard Richter," *Leonardo* **41**, 484 (2008).

<sup>177</sup>See [https://en.wikipedia.org/wiki/Not\\_invented\\_here](https://en.wikipedia.org/wiki/Not_invented_here) for Not-invented-here syndrome.

<sup>178</sup>H. Ooe, D. Kirpal, D. S. Wastl, A. J. Weymouth, T. Arai, and F. J. Giessibl, "Amplitude dependence of image quality in atomically-resolved bimodal atomic force microscopy," *Appl. Phys. Lett.* **109**, 141603 (2016).

<sup>179</sup>F. Ohnesorge and G. Binnig, "True atomic resolution by atomic force microscopy through repulsive and attractive forces," *Science* **260**, 1451 (1993).

<sup>180</sup>N. Okabayashi, A. Gustafsson, A. Peronio, M. Paulsson, T. Arai, and F. J. Giessibl, "Influence of atomic tip structure on the intensity of inelastic tunneling spectroscopy data analyzed by combined scanning tunneling spectroscopy, force microscopy, and density functional theory," *Phys. Rev. B* **93**, 165415 (2016).

<sup>181</sup>N. Okabayashi, A. Peronio, M. Paulsson, T. Arai, and F. J. Giessibl, "Vibrations of a molecule in an external force field," *Proc. Natl. Acad. Sci. U. S. A.* **115**, 4571 (2018).

<sup>182</sup>L. Patera, X. Liu, N. Mosso, S. Decurtins, S. X. Liu, and J. Repp, "Crystallization of a two-dimensional hydrogen-bonded molecular assembly: Evolution of the local structure resolved by atomic force microscopy," *Angew. Chem., Int. Ed.* **56**, 10786 (2017).

<sup>183</sup>N. Pavlíček, B. Fleury, M. Neu, J. Niedenführ, C. Herranz-Lancho, M. Ruben, and J. Repp, "Atomic force microscopy reveals bistable configurations of dibenzo[a,h]thianthrene and their interconversion pathway," *Phys. Rev. Lett.* **108**, 086101 (2012).

<sup>184</sup>N. Pavlíček and L. Gross, "Generation, manipulation and characterization of molecules by atomic force microscopy," *Nat. Rev. Chem.* **1**, 0005 (2017).

<sup>185</sup>J. Peng, J. Guo, P. Hapala, D. Cao, R. Ma, B. Cheng, L. Xu, O. Martin, P. Jelinek, E. Wang, and Y. Jiang, "Weakly perturbative imaging of interfacial water with submolecular resolution by atomic force microscopy," *Nat. Commun.* **9**, 122 (2018).

<sup>186</sup>J. Peng, D. Cao, Z. He, J. Guo, P. Hapala, R. Ma, B. Cheng, J. Chen, W. J. Xie, X.-Z. Li, P. Jelinek, L.-M. Xu, Y. Q. Gao, E.-G. Wang, and Y. Jiang, "The effect of hydration number on the interfacial transport of sodium ions," *Nature* **557**, 701 (2018).

<sup>187</sup>R. Perez, I. Stich, M. C. Payne, and K. Terakura, "Surface-tip interactions in noncontact atomic-force microscopy on reactive surfaces: Si(111)," *Phys. Rev. B* **58**, 10835 (1998).

<sup>188</sup>A. Peronio and F. J. Giessibl, "Attempts to test an alternative electrodynamic theory of superconductors by low-temperature scanning tunneling and atomic force microscopy," *Phys. Rev. B* **94**, 094503 (2016).

<sup>189</sup>T. Peters and R. H. Waterman, *Search of Excellence* (Oxford University Press, New York, Oxford, 1982).

<sup>190</sup>F. Pielmeier and F. J. Giessibl, "Spin resolution and evidence for superexchange on NiO(001) observed by force microscopy," *Phys. Rev. Lett.* **110**, 266101 (2013).

<sup>191</sup>F. Pielmeier, D. Meuer, D. Schmid, C. Strunk, and F. J. Giessibl, "Impact of thermal frequency drift on highest precision force microscopy using quartz-based force sensors at low temperatures," *Beilstein J. Nanotechnol.* **5**, 407–412 (2014).

<sup>192</sup>F. Pielmeier, G. Landolt, B. Slomski, S. Muff, J. Berwanger, A. Eich, A. A. Khajetoorians, J. Wiebe, Z. S. Aliev, M. B. Babanly, R. Wiesendanger, J. Osterwalder, E. V. Chulkov, F. J. Giessibl, and J. H. Dil, "Response of the topological surface state to surface disorder in TlBiSe<sub>2</sub>," *New J. Phys.* **17**, 023067 (2015).

<sup>193</sup>F. Pielmeier and F. J. Giessibl, "Dissipation on TlBiSe<sub>2</sub>" (unpublished).

- <sup>194</sup>L. Prandtl, "Ein gedankenmodell zur kinetischen theorie der festen körper," *J. Appl. Math. Mech.* **8**, 85 (1928).
- <sup>195</sup>K. Pürckhauer, A. J. Weymouth, K. Pfeffer, L. Kullmann, E. Mulvihill, M. P. Krahn, D. J. Müller, and F. J. Giessibl, "Imaging in biologically-relevant environments with AFM using stiff qPlus sensors," *Sci. Rep.* **8**, 9330 (2018).
- <sup>196</sup>M. Rashidi, W. Vine, T. Dienel, L. Livadaru, J. Retallick, T. Huff, K. Walus, and R. A. Wolkow, "Initiating and monitoring the evolution of single electrons within atom-defined structures," *Phys. Rev. Lett.* **121**, 166801 (2018).
- <sup>197</sup>J. Repp, G. Meyer, F. Olsson, and M. Persson, "Controlling the charge state of individual gold atoms," *Science* **305**, 493 (2004).
- <sup>198</sup>M. Reticcioli, M. Setvin, X. Hao, P. Flauger, G. Kresse, M. Schmid *et al.*, "Polaron-driven surface reconstructions," *Phys. Rev. X* **7**, 031053 (2017).
- <sup>199</sup>E. Blick, Website of Gerhard Richter <https://www.gerhard-richter.com/en/art/editions/first-view-12800>, 2000.
- <sup>200</sup>See <https://www.gerhard-richter.com/en/art/editions/graphite-14153> for Graphit at website of Gerhard Richter, 2005.
- <sup>201</sup>A. Riss, S. Wickenburg, P. Gorman, L. Z. Tan, H.-Z. Tsai, D. G. de Oteyza, Y.-C. Chen, A. J. Bradley, M. M. Ugeda, G. Etkin, S. G. Louie, F. R. Fischer, and M. F. Crommie, "Local electronic and chemical structure of oligo-acetylene derivatives formed through radical cyclizations at a surface," *Nano Lett.* **14**, 2251 (2014).
- <sup>202</sup>P. Ruffieux, S. Wang, B. Yang, C. Sánchez-Sánchez, J. Liu, T. Dienel, L. Talirz, P. Shinde, C. A. Pignedoli, D. Passerone, T. Dumsclaff, X. Feng, K. Müllen, and R. Fasel, "On-surface synthesis of graphene nanoribbons with zigzag edge topology," *Nature* **531**, 489 (2016).
- <sup>203</sup>D. Rugar and P. Hansma, "Atomic force microscopy," *Phys. Today* **43**(10), 23 (1990).
- <sup>204</sup>J. Rycken, *Combined Low-Temperature Scanning Probe Microscopy and Magneto-Transport Experiments for the Local Investigation of Mesoscopic Systems*, Diss. ETH No. 14229 (Swiss Federal Institute of Technology, Zurich, CH, 2001).
- <sup>205</sup>J. E. Sader, J. W. M. Chon, and P. Muvaney, "Calibration of rectangular atomic force microscope cantilevers," *Rev. Sci. Instrum.* **70**, 3967 (1999).
- <sup>206</sup>J. E. Sader and S. Jarvis, "Accurate formulas for interaction force and energy in frequency modulation force spectroscopy," *Appl. Phys. Lett.* **84**, 1801 (2004).
- <sup>207</sup>J. E. Sader, B. D. Hughes, F. Huber, and F. J. Giessibl, "Interatomic force laws that corrupt their own measurement," e-print [arXiv:1709.07571](https://arxiv.org/abs/1709.07571) [cond-mat.mes-hall].
- <sup>208</sup>J. E. Sader, B. D. Hughes, F. Huber, and F. J. Giessibl, "Interatomic force laws that evade dynamic measurement," *Nat. Nanotechnol.* **13**, 1088 (2018).
- <sup>209</sup>A. Schirmeisen, G. Cross, A. Stalder, P. Grütter, and U. Dürig, "Metallic adhesion and tunnelling at the atomic scale," *New J. Phys.* **2**, 29 (2000).
- <sup>210</sup>M. Schneiderbauer, D. Wastl, and F. J. Giessibl, "qPlus magnetic force microscopy in frequency-modulation mode with millihertz resolution," *Beilstein J. Nanotechnol.* **3**, 174 (2012).
- <sup>211</sup>M. Schneiderbauer, M. Emmrich, A. J. Weymouth, and F. J. Giessibl, "CO tip functionalization inverts atomic force microscopy contrast via short-range electrostatic forces," *Phys. Rev. Lett.* **112**, 166102 (2014).
- <sup>212</sup>M. Schmid, J. Mannhart, and F. J. Giessibl, "Searching atomic spin contrast on nickel oxide (001) by force microscopy," *Phys. Rev. B* **77**, 045402 (2008).
- <sup>213</sup>B. Schuler, W. Liu, A. Tkatchenko, N. Moll, G. Meyer, A. Mistry, D. Fox, and L. Gross, "Adsorption geometry determination of single molecules by atomic force microscopy," *Phys. Rev. Lett.* **111**, 106103 (2013).
- <sup>214</sup>B. Schuler, S. Fatayer, F. Mohn, N. Moll, N. Pavliček, G. Meyer, D. Pena, and L. Gross, "Reversible Bergman cyclization by atomic manipulation," *Nat. Chem.* **8**, 220 (2016).
- <sup>215</sup>B. Schuler, S. Fatayer, G. Meyer, E. Rogel, M. Moir, Y. Zhang, M. R. Harper, A. E. Pomerantz, K. D. Bake, M. Witt, D. Pera, J. Douglas Kushnerick, O. C. Mullins, C. Ovalles, F. G. A. van den Berg, and L. Gross, "Heavy oil based mixtures of different origins and treatments studied by AFM," *Energy Fuels* **31**, 6856 (2017).
- <sup>216</sup>M. Schwarz, A. Riss, M. Garnica, J. Dücke, P. S. Deimel, D. A. Duncan, P. K. Thakur, T. L. Lee, A. P. Seitsonen, J. V. Barth, F. Allegretti, and W. Auwärter, "Corrugation in the weakly interacting hexagonal-BN/Cu(111) system: Structure determination by combining noncontact atomic force microscopy and x-ray standing waves," *ACS Nano* **11**, 9151 (2017).
- <sup>217</sup>J. Schwenk, S. Kim, J. Berwanger, S. Blankenship, W. Cullen, Y. Kuk, F. Giessibl, and J. Strosio, "A combined atomic force- and tunneling microscopy system at 10 mK temperature," in presentation E01.00009 at APS March Meeting, Los Angeles, 2018.
- <sup>218</sup>M. Setvin, C. Franchini, X. Hao, M. Schmid, A. Janotti, M. Kaltak *et al.*, "Direct view at excess electrons in TiO<sub>2</sub> rutile and anatase," *Phys. Rev. Lett.* **113**, 086402 (2014).
- <sup>219</sup>M. Setvin, M. Wagner, M. Schmid, G. S. Parkinson, and U. Diebold, "Surface point defects on bulk oxides: Atomically-resolved scanning probe microscopy," *Chem. Soc. Rev.* **46**, 1772 (2017).
- <sup>220</sup>M. Setvin, J. Hulva, G. S. Parkinson, M. Schmid, and U. Diebold, "Electron transfer between anatase TiO<sub>2</sub> and an O<sub>2</sub> molecule directly observed by atomic force microscopy," *Proc. Natl. Acad. Sci. U. S. A.* **107**(3), E2556 (2017).
- <sup>221</sup>M. Setvin, M. Reticcioli, F. Pölzleitner, J. Hulva, M. Schmid, L. A. Boatner, C. Franchini, and U. Diebold, "Polarity compensation mechanisms on the perovskite surface KTaO<sub>3</sub>(001)," *Science* **359**, 572 (2018).
- <sup>222</sup>M. Shekhirev, P. Zahl, and A. Sinitskii, "Phenyl functionalization of atomically precise graphene nanoribbons for engineering inter-ribbon interactions and graphene nanopores," *ACS Nano* **12**, 8662 (2018).
- <sup>223</sup>A. Shiotari and Y. Sugimoto, "Ultrahigh-resolution imaging of water networks by atomic force microscopy," *Nat. Commun.* **8**, 14313 (2017).
- <sup>224</sup>D. Sobel, *Longitude: The True Story of a Lone Genius Who Solved the Greatest Scientific Problem of His Time* (Walker & Company, 1995).
- <sup>225</sup>Y. J. Song, A. F. Otte, V. Shvarts, Z. Zhao, Y. Kuk, S. R. Blankenship, A. Band, F. M. Hess, and J. A. Strosio, "Invited review article: A 10 mK scanning probe microscopy facility," *Rev. Sci. Instrum.* **81**, 121101 (2010).
- <sup>226</sup>Y. J. Song, A. F. Otte, Y. Kuk, Y. Hu, D. B. Torrance, P. N. First, W. A. de Heer, H. Min, S. Adam, M. D. Stiles, A. H. MacDonald, and J. A. Strosio, "High-resolution tunnelling spectroscopy of a graphene quartet," *Nature* **467**, 185 (2010).
- <sup>227</sup>B. C. Stipe, M. A. Rezaei, and W. Ho, "Single molecule vibrational spectroscopy and microscopy," *Science* **280**, 1732 (1998).
- <sup>228</sup>Y. Sugimoto, P. Pou, S. Hirayama, N. Oyabu, O. Custance, and S. Morita, "Atom inlays performed at room temperature using atomic force microscopy," *Nat. Mater.* **4**, 156 (2005).
- <sup>229</sup>Y. Sugimoto, P. Pou, M. Abe, P. Jelinek, R. Perez, S. Morita, and O. Custance, "Chemical identification of individual surface atoms by atomic force microscopy," *Nature* **446**, 64 (2007).
- <sup>230</sup>Z. Sun, M. P. Boneschanscher, I. Swart, D. Vanmaekelbergh, and P. Liljeroth, "Quantitative atomic force microscopy with carbon monoxide terminated tips," *Phys. Rev. Lett.* **106**, 046104 (2011).
- <sup>231</sup>I. Swart, personal communication (2014).
- <sup>232</sup>A. Sweetman, S. Jarvis, R. Danza, J. Bamidele, S. Gangopadhyay, G. A. Shaw, L. Kantorovich, and P. Moriarty, "Toggling bistable atoms via mechanical switching of bond angle," *Phys. Rev. Lett.* **106**, 136101 (2011).
- <sup>233</sup>A. Sweetman, S. Jarvis, R. Danza, and P. Moriarty, "Effect of the tip state during qPlus noncontact atomic force microscopy of Si(100) at 5 K: Probing the probe," *Beilstein J. Nanotechnol.* **3**, 25 (2012).
- <sup>234</sup>A. Sweetman, M. A. Rashid, S. P. Jarvis, J. Dunn, P. Rahe, and P. Moriarty, "Visualizing the orientational dependence of an intermolecular potential," *Nat. Commun.* **7**, 1 (2016).
- <sup>235</sup>R. Temirov, S. Soubatch, O. Neucheva, A. Lassise, and F. S. Tautz, "A novel method achieving ultra-high geometrical resolution in scanning tunnelling microscopy," *New J. Phys.* **10**, 053012 (2008).
- <sup>236</sup>R. Temirov, A. Lassise, F. B. Anders, and F. S. Tautz, "Kondo effect by controlled cleavage of a single-molecule contact," *Nanotechnology* **19**, 065401 (2008).
- <sup>237</sup>R. Temirov, M. F. B. Green, N. Friedrich, P. Leinen, T. Esat, P. Chmielniak, S. Sarwar, J. Rawson, P. Kögerler, C. Wagner, M. Rohlfing, and F. Stefan Tautz, "Molecular model of a quantum dot beyond the constant interaction approximation," *Phys. Rev. Lett.* **120**, 206801 (2018).



- <sup>238</sup>M. Ternes, C. Gonzalez, C. P. Lutz, P. Hapala, F. J. Giessibl, P. Jelinek, and A. Heinrich, "Interplay of conductance, force, and structural change in metallic point contacts," *Phys. Rev. Lett.* **106**, 016802 (2011).
- <sup>239</sup>M. Ternes, C. Lutz, C. F. Hirjibehedin, F. J. Giessibl, and A. Heinrich, "The force needed to move an atom on a surface," *Science* **319**, 1066 (2008).
- <sup>240</sup>G. A. Tomlinson, "A molecular theory of friction," *Philos. Mag.* **7**, 905 (1929).
- <sup>241</sup>M. Tortonese, R. C. Barrett, and C. F. Quate, "Atomic resolution with an atomic force microscope using piezoresistive detection," *Appl. Phys. Lett.* **62**, 834 (1993).
- <sup>242</sup>S. Torbrügge, O. Schaff, and J. Rychen, "Application of the KolibriSensor to combined atomic-resolution scanning tunneling microscopy and non-contact atomic-force microscopy imaging," *J. Vac. Sci. Technol., B: Nanotechnol. Microelectron.: Mater., Process., Meas., Phenom.* **28**, C4E12 (2010).
- <sup>243</sup>R. C. Tung, T. Wutscher, D. Martinez-Martin, and R. G. Reifenberger, F. Giessibl, and A. Raman, "Higher-order eigenmodes of qPlus sensors for high resolution dynamic atomic force microscopy," *J. Appl. Phys.* **107**, 104508 (2010).
- <sup>244</sup>J. van der Lit, M. P. Boneschanscher, D. Vanmaekelbergh, M. Ijas, A. Uppstu, M. Ervasti, A. Harju, P. Liljeroth, and I. Swart, "Suppression of electron-vibron coupling in graphene nanoribbons contacted via a single atom," *Nat. Commun.* **4**, 2023 (2013).
- <sup>245</sup>C. M. Van Vliet, "Random walk and  $1/f$  noise," *Physica A* **303**, 421 (2001).
- <sup>246</sup>R. W. Ward, "Constants of alpha quartz," in *Piezoelectricity*, edited by C. Zwick Rosen, B. V. Hiremath, and R. Newnham (American Institute of Physics, New York, 1992), pp. 211–220.
- <sup>247</sup>C. Wagner, N. Fournier, F. S. Tautz, and R. Temirov, "Measurement of the binding energies of the organic-metal perylene-teracarboxylic-dianhydride/Au(111) bonds by molecular manipulation using an atomic force microscope," *Phys. Rev. Lett.* **109**, 076102 (2012).
- <sup>248</sup>C. Wagner, N. Fournier, F. S. Tautz, and R. Temirov, "The role of surface corrugation and tip oscillation in single-molecule manipulation with a non-contact atomic force microscope," *Beilstein J. Nanotechnol.* **5**, 202 (2014).
- <sup>249</sup>C. Wagner, N. Fournier, V. G. Ruiz, C. Li, K. Müllen, M. Rohlfing, A. Tkatchenko, R. Temirov, and F. Stefan Tautz, "Non-additivity of molecule-surface van der Waals potentials from force measurements," *Nat. Commun.* **5**, 5568 (2014).
- <sup>250</sup>C. Wagner, M. F. B. Green, P. Leinen, T. Deilmann, P. Krüger, M. Rohlfing, R. Temirov, and F. Stefan Tautz, "Scanning quantum dot microscopy," *Phys. Rev. Lett.* **115**, 026101 (2015).
- <sup>251</sup>X.-Y. Wang, M. Richter, Y. He, J. Björk, A. Riss, R. Rajesh, M. Garnica, F. Hennersdorf, J. J. Weigand, A. Narita, R. Berger, X. Feng, W. Auwärter, J. V. Barth, C.-A. Palma, and K. Müllen, "Exploration of pyrazine-embedded antiaromatic polycyclic hydrocarbons generated by solution and on-surface azomethine ylide homocoupling," *Nat. Commun.* **8**, 1948 (2017).
- <sup>252</sup>D. Wastl, A. Weymouth, and F. J. Giessibl, "Optimizing atomic resolution of force microscopy in ambient conditions," *Phys. Rev. B* **87**, 245415 (2013).
- <sup>253</sup>D. Wastl, A. Weymouth, and F. J. Giessibl, "Atomically resolved graphitic surfaces in air by atomic force microscopy," *ACS Nano* **8**, 5233 (2014).
- <sup>254</sup>D. Wastl, M. Judmann, A. Weymouth, and F. J. Giessibl, "Atomic resolution of calcium and oxygen sublattices of calcite in ambient conditions by atomic force microscopy using qPlus sensors with sapphire tips," *ACS Nano* **9**, 3858 (2015).
- <sup>255</sup>J. Welker, F. de Faria Elsner, and F. J. Giessibl, "Application of the equipartition theorem to the thermal excitation of quartz tuning forks," *Appl. Phys. Lett.* **99**, 084102 (2011).
- <sup>256</sup>J. Welker, E. Illek, and F. J. Giessibl, "Analysis of force-deconvolution methods in frequency-modulation atomic force microscopy," *Beilstein J. Nanotechnol.* **3**, 238 (2012).
- <sup>257</sup>J. Welker and F. J. Giessibl, "Revealing the angular symmetry of chemical bonds by atomic force microscopy," *Science* **336**, 444 (2012).
- <sup>258</sup>J. Welker, A. John Weymouth, and F. J. Giessibl, "The influence of chemical bonding configuration on atomic identification by force spectroscopy," *ACS Nano* **7**, 7377 (2013).
- <sup>259</sup>A. J. Weymouth, T. Wutscher, J. Welker, T. Hofmann, and F. J. Giessibl, "Phantom force induced by tunneling current: A characterization on Si(111)," *Phys. Rev. Lett.* **106**, 226801 (2011).
- <sup>260</sup>A. J. Weymouth, D. Meuer, P. Mutombo, T. Wutscher, M. Ondracek, P. Jelinek, and F. J. Giessibl, "Atomic structure affects the directional dependence of friction," *Phys. Rev. Lett.* **111**, 126103 (2013).
- <sup>261</sup>A. J. Weymouth, T. Hofmann, and F. J. Giessibl, "Quantifying molecular stiffness and interaction with lateral force microscopy," *Science* **343**, 1120 (2013).
- <sup>262</sup>A. J. Weymouth, "Non contact lateral force microscopy," *J. Phys.: Condens. Matter* **29**, 323001 (2017).
- <sup>263</sup>A. J. Weymouth, personal communication (2018).
- <sup>264</sup>S. Wickenburg, J. Lu, J. Lischner, H.-Z. Tsai, A. A. Omrani, A. Riss, C. Karrasch, A. Bradley, H. S. Jung, R. Khajeh, D. Wong, K. Watanabe, T. Taniguchi, A. Zettl, A. H. Castro Neto, S. G. Louie, and M. F. Crommie, "Tuning charge and correlation effects for a single molecule on a graphene device," *Nat. Commun.* **7**, 13553 (2016).
- <sup>265</sup>See [https://en.wikipedia.org/wiki/Redefinition\\_of\\_SI\\_base\\_units](https://en.wikipedia.org/wiki/Redefinition_of_SI_base_units) for Wikipedia article on the redefinition of SI base units.
- <sup>266</sup>C. Alan Wright and S. D. Solares, "On mapping subangstrom electron clouds with force microscopy," *Nano Lett.* **11**, 5026 (2011).
- <sup>267</sup>E. Wutscher and F. J. Giessibl, "Atomic force microscopy at ambient and liquid conditions with stiff sensors and small amplitudes," *Rev. Sci. Instrum.* **82**, 093703 (2011).
- <sup>268</sup>T. Wutscher and F. J. Giessibl, "Note: In situ cleavage of crystallographic oriented tips for scanning probe microscopy," *Rev. Sci. Instrum.* **82**, 026106 (2011).
- <sup>269</sup>J. Zhang, P. Chen, B. Yuan, W. Ji, Z. Cheng, and X. Qiu, "Real-space identification of intermolecular bonding with atomic force microscopy," *Science* **342**, 611 (2013).
- <sup>270</sup>L. A. Zotti, W. A. Hofer, and F. J. Giessibl, "Electron scattering in scanning probe microscopy experiments," *Chem. Phys. Lett.* **420**, 177 (2006).
- <sup>271</sup>S. Polesya, S. Mankovsky, and H. Ebert, "DFT calculations of AFM images of metallic adatoms" (unpublished).
- <sup>272</sup>S. Yamazaki, K. Maeda, Y. Sugimoto, M. Abe, V. Zobač, P. Pou, L. Rodrigo, P. Mutombo, R. Pérez, P. Jelinek, and S. Morita, "Interplay between switching driven by the tunneling current and atomic force of a bistable four-atom Si quantum dot," *Nano Lett.* **15**(7), 4356 (2015).
- <sup>273</sup>A. Shiotari, T. Odani, and Y. Sugimoto, "Torque-induced change in configuration of a single NO molecule on Cu(110)," *Phys. Rev. Lett.* **121**, 116101 (2018).